Mechanical and Physical Properties of Additive Friction Stir Deposited Aluminum

Merris Corinne Wells

Thesis submitted to the faculty of the Virginia Polytechnic Institute and State University
in partial fulfillment of the requirements for the degree of

Master of Science
In
Materials Science and Engineering

Alan P. Druschitz, Chair
Hang Yu
Thomas Dorin

June 13th, 2022
Blacksburg, VA

Keywords: Additive Manufacturing, Additive Friction Stir Deposition, Aluminum, Tensile Testing, Fractography, Microstructure

Mechanical and Physical Properties of Additive Friction Stir Deposited Aluminum

Merris Corinne Wells

ABSTRACT

The goal of this research is to aid the development of large-scale additive manufacturing of jointless underbody hulls for the Army Ground Vehicle Systems by 1) generating an improved mechanical and metallurgical database and 2) understanding the Additive Friction Stir Deposition (AFSD) process. AFSD is a solid-state additive manufacturing process that is a high strain rate and a hot working process that deforms material onto a substrate and builds a component layer by layer. This unique, solid-state additive manufacturing process has the potential for scalability into ground vehicle applications on the extra large-scale due to its solid-state nature. Two different aluminum alloys were investigated: Al-Mg-Si (6061) and Al-Zn-Mg-Cu (7075). AFSD builds were evaluated in the transverse or through layer direction (Z) and the 6061 material was also evaluated in the longitudinal direction (X). Uniaxial tensile testing was performed to generate mechanical property data while fractography, and metallography were used to better understand the metallurgical implications of this process. This research determined that the refinement of the grain size caused by the AFSD process had little or no strengthening effect on the mechanical properties of either alloy. Instead, the as-deposited condition in both alloys were soft with good ductility due to the dissolution of the strengthening particles. After heat treatment, the elongation and fracture mode of the 6061 alloy was dependent on the layer direction. Failure often initiated at interfaces and affected the materials' elastic-plastic behavior. For the 7075 alloy, the strength and failure mechanism of the material were affected by the presence of the graphite lubricant used during processing. The use of graphite increased the variability of the mechanical properties results and caused premature failure in numerous samples. In both alloys, the heat treatment caused grain coarsening to varying degrees which can affect the mechanical behavior. From these results, it was found that a precipitation strengthening heat treatment is required for material deposited with AFSD to achieve the minimum mechanical property standards for a forging. Recommendations and future work include 1) investigating the effect of residual stresses on AFSD components, 2) determining the fatigue properties of AFSD materials, 3) continuing to increase the database of mechanical properties for AFSD materials, and 4) developing additional lubricants for the AFSD process.

Mechanical and Physical Properties of Additive Friction Stir Deposited Aluminum

Merris Corinne Wells

GENERAL AUDIENCE ABSTRACT

The results of this research will be used to help generate design requirements for large-scale additively manufactured parts such as underbody tank hulls. This research generated and expanded on the mechanical and metallurgical understanding of solid-state additively manufactured aluminum. The solid-state additive process used was Additive Friction Stir Deposition. Like its name, this process uses a rotating tool head to apply friction to a solid bar of aluminum that then generates heat which makes the metal soft enough to stir and deposit into a layer. Another layer is then deposited on top and repeated layer by layer until the final part is completed. Other metal additive manufacturing processes that involve melting and then rapidly cooling the material degrade the quality of the metal material.

The first part of this research investigated the mechanical properties in different layer directions either pulling along the build direction or against the layers. The results showed that a heat treatment was required to improve the strength of the aluminum to meet current standards of quality. However, the ability of the aluminum to elongate depended on the orientation of the layers.

The second part of this research investigated the effect that a graphite lubricant used on the aluminum feedstock to help prevent the material from sticking in the tool head affected the mechanical properties. The results show that the graphite lubricant did not dissolve or disappear into the metal and caused a reduction in the elongation of the aluminum. Recommendations for extra large-scale metal additive manufacturing are to design parts to apply the highest stress along the layer direction and to eliminate the use of the graphite lubricant.

Mechanical and Physical Properties of Additive Friction Stir Deposited Aluminum

Merris Corinne Wells

Acknowledgements

I would first like to thank my committee for their guidance and support in completing this project. My committee chair, Dr. Alan Druschitz has given me his unwavering support, expertise on all things metallurgy, and has inspired my graduate career. I would like to thank Dr. Hang Yu and his research group for their knowledge and characterization of the AFSD process. Dr. Thomas Dorin from Deakin University for his support and knowledge of metallurgy.

This project would not have been possible without the financial support of ASTRO America and the Jointless Underbody Hull project. I am also grateful to MELD manufacturing for providing the material necessary to complete my thesis. These organizations' desire to improve and further that state of the art in metal AM is admirable.

Thank you to the MSE department at Virginia Tech for giving me the tools necessary to further my education. I would like to acknowledge the MSE graduate program and the great support they offer to their students.

Finally, I would like to thank my colleagues, friends, and family as they have motivated me to further my education and at times assisted my work. Without everyone’s support, I would not have completed this thesis.

Table of Contents

List of Figures vii
List of Tables xiv
List of Equations xv

Chapter 1 Introduction
1.1 Motivation 1
1.2 Jointless Underbody Hull Project 1
1.3 Large-Scale Additive Manufacturing 3

Chapter 2 Literature Review
2.1 Additive Friction Stir Deposition Process 7
2.2 AFSD Microstructure 8
2.3 AFSD Mechanical Properties 9
2.4 Hot Working of Aluminum 12
2.5 Precipitation Strengthening Heat Treatment 13

Chapter 3 Methods
3.1 AFSD Builds 16
3.1.1 6061 Builds 16
3.1.2 7075 Builds 18
3.2 Heat Treatment and Chemistry 18
3.2.1 Heat Treatment of 6061 19
3.2.2 Heat Treatment of 7075 20
3.3 Tensile Testing 20
3.4 Mechanical Properties 22
3.5 Quality Index 23
3.6 T-test 24
3.7 Fractography 25
3.8 Particle Analysis 25
3.9 Metallography 26
3.10 Raman Spectroscopy 26

Chapter 4 Results 6061
4.1 Mechanical AFSD 6061 27
4.1.1 As-Deposited 28
4.1.2 Heat Treated 29
4.1.3 Elastic Modulus 31
4.2 Fractography 32
4.2.1 Wrought 6061-T6 32
4.2.2 AFSD Z 6061-AD 35
4.2.3 AFSD X 6061-AD 37
4.2.4 AFSD Z 6061-T6 39
4.2.5 AFSD 6061-T6 43
4.2.6 Particle Analysis of 6061 45

4.3 6061 Outliers....49
4.3.1 AFSD Z 6061-AD #13....49
4.3.2 AFSD Z 6061-T6 #5....51

Chapter 5 Results 7075
5.1 Mechanical AFSD 7075....55
5.1.1 As-Deposited....56
5.1.2 Heat Treated....57
5.1.3 Elastic Modulus....59
5.2 Fractography....60
5.2.1 Wrought 7075-T6....60
5.2.2 AFSD Z 7075-AD....62
5.2.3 AFSD Z 7075-T6....64
5.2.4 Particle Analysis of 7075....66
5.3 7075 Outliers....68
5.3.1 AFSD Z 7075-AD #13....69
5.3.2 AFSD Z 7075-T6 #14....71
5.3.3 AFSD Z 7075-T6 #15....74
5.4 Raman Spectroscopy....76

Chapter 6 Discussion
6.1 Mechanical Properties....80
6.2 Fracture Mechanisms....81
6.2.1 AFSD 6061....82
6.2.2 AFSD 7075....84
6.3 Microstructure....85

Chapter 7 Conclusions
7.1 Overall....87
7.2 6061....87
7.3 7075....88
7.4 Future Work....89

Bibliography....90
Appendix A....95
Appendix B....97

List of Figures

Figure 1.1 M113 knocked out of service from underbody mines during Tet fighting, 1968 (Photo courtesy of the National and Calvary Museum)……..…2

Figure 1.2 The largest forged underbody hull was created jointly with ALCOA and the GVSC...3

Figure 1.3 A fuel tank made from EBAM (left) and securing brackets made from WAAM (right)……...4

Figure 1.4 A 3D rendering of the AFSD system that will be the largest AM metal system ever built to-date……..6

Figure 2.1 The deposition of 6061 aluminum with a temperature controlled aperture that changes the spindle tool head speed (Ω) and the travel velocity (V) to adjust the working temperature. {Image recreated from MELD Manufacturing white papers}…….7

Figure 2.2 The formation of subgrains in a hot worked material with increasing strain…….8

Figure 2.3 EBSD images of the undeformed 2024 material (a) and then the dynamically recrystallized equiaxed grain structure after processing with AFSD (b)…….9

Figure 2.4 Modified fatigue specimen used for testing the tensile strength of AFSD material used in most published literature……10

Figure 2.5 Ultimate tensile strength of the AFSD 6061 material in various orientations and conditions……...11

Figure 2.6 Ultimate tensile strength of the AFSD 7075 material in various orientations and conditions……...12

Figure 2.7 The forged aircraft grain structure (left) and the AFSD 6061 with noted layer direction (right)…….13

Figure 3.1 The single wall build for the Z direction samples (above) and the X direction samples (below) showing the orientation of the tensile bars……...17

Figure 3.2 The Z direction single track build made of 7075 showing the orientation of the tensile bars…….18

Figure 3.3 A diagram of the tensile specimen showing the important sample dimensions……...21

Figure 3.4 The methods used to calculate the E, 0.2% offset Yield strength, Ultimate tensile strength, and Elongation at fracture……...23

Figure 4.1 The optical image (left) at 5x magnification shows a dull fibrous appearance with the 3D rendering (right) shows the side profile of the shear lip (red arrow) and ductile fibrous center (blue) which indicates a ductile overload failure……...33

Figure 4.2 The diagram of the process by which microvoids form and their appearance under an SEM……...33

Figure 4.3 The center of the wrought 6061-T6 at 1000x showing microvoid coalescence indicative of ductile overload failure…….34

Figure 4.4 The cross section of the fracture surface at 10x with a Keller's etch reveals the grain flow of the material that follows the direction of deformation……..34

Figure 4.5 The fracture surface of the Z 6061-AD #15 sample had a shear lip (red arrow) and significant reduction in cross section…….35

Figure 4.6 The center of the fracture surface of AFSD Z 6061-AD #15 in the secondary electron detection mode at and 1000x showing microvoid coalescence indicative of ductile failure…….36

Figure 4.7 The cross section of the fracture surface of AFSD Z 6061-AD #15 at 10x showed the grain flow of the AFSD material that distorted around the reduced cross section where the sample was etched using Keller's reagent…….36

Figure 4.8 The fracture surface of the X 6061-AD #2-1 has a large ridge (red arrow) and ridges throughout the surface (blue arrow). The 3D the topography of the fracture surface as viewed from the top (a) and bottom (b) side……..38

Figure 4.9 The grain flow in sample X 6061-AD #2-1 etched with Keller's revealed that the grain flow distorted in the direction of the load…….38

Figure 4.10 There were numerous secondary cracks at the base of the ridges (b and c). On the sides inside of one of these cracks (d), there were microvoids……..39

Figure 4.11 The fracture surface of the X 6061-T6 #9 (left) and the 3D rendering of the surface (right) showing ledges on the surface……40

Figure 4.12 The difference in microvoid appearance of the step at the tread (b) the riser (c) and at the interface between the tread and riser (d)……..41

Figure 4.13 At the flat section of the ledge (a) the appearance is smooth with shallow microvoids (b). The crack that runs parallel to the fracture surface (c and d) is deep with shallow microvoids……..42

Figure 4.14 The Z 6061-T6 #9 sample after Keller's etch shows that after heat treatment the grains had grown in the direction of the layers……..43

Figure 4.15 The figure shows that the dark lines are all parallel to etch other and run across the fracture surface……...44

Figure 4.16 The appearance of the fracture surface changed from smooth to fibrous (right) near the secondary crack circled in red……..44

Figure 4.17 The cracks with a smooth appearance had shallow microvoids……...44

Figure 4.18 The grains grew after heat treatment in the direction of the layers and a crack initiated around a grain, circled in red…….45

Figure 4.19 The heat treated fracture surface of wrought 6061-T6 #2 had Si and Mg rich particles in the bottom of the microvoids with Fe evenly dispersed……46

Figure 4.20 The as-deposited fracture surface had Si and Mg rich particles in the bottom of the microvoids sample AFSD Z 6061-AD #15……...46

Figure 4.21 The heat treated fracture surface had Si and Mg rich particles in the bottom of the microvoids sample AFSD Z 6061-T6 #7……...47

Figure 4.22 The heat treated fracture surface also had Si and Mg rich particles that were evenly dispersed on the smooth section of the fracture surface in sample AFSD Z 6061-T6 #7…….47

Figure 4.23 The heat treated fracture surface with microvoids had Si and Mg rich particles that were evenly dispersed on the facture surface in sample AFSD X 6061-T6 #1-2…….…….48

Figure 4.24 The heat treated fracture surface with the smooth and shallow microvoids had Si and Mg rich particles that were dispersed on the facture surface in sample AFSD X 6061-T6 #1-2……..48

Figure 4.25 The fracture surface had two distinct zones the ductile 'twist' (left) and the granular appearance (right)……..50

Figure 4.26 The fracture surface in the red circle was ductile in appearance (a) while the section in the blue circle was smooth in appearance (b)……50

Figure 4.27 The EDS analysis of the ductile section of the 'twist' showed Mg and Si rich particles in the microvoids…….51

Figure 4.28 EDS analysis of the smooth and granular section showed Mg and Si rich particles that were not as evenly dispersed as the ductile 'twist' section…….51

Figure 4.29 The fracture surface (left) and the topography (right) showed some ledges with a sharp corner outlined in red……...52

Figure 4.30 The fracture surface showed that most of the fracture surface was smooth in appearance with very shallow microvoids…….53

Figure 4.31 Although most microvoids were shallow, the particles in the deeper microvoids were Mg and Si rich……53

Figure 4.32 The grains grew after heat treatment in the direction of the layers with a crack initiating at a grain boundary…….54

Figure 5.1 The optical image (left) at 5x magnification showed a dull fibrous appearance with the 3D rendering (right) showed the side profile of the shear lip (red arrow) and ductile fibrous center (blue), which indicated a ductile overload failure……...60

Figure 5.2 The center of the wrought 7075-T6 at 1000x showed microvoid coalescence indicative of ductile overload failure with a small secondary crack circled in red……61

Figure 5.3 A cross section included the fracture surface of wrought 7075-T6 at 2.5X etched with Keller's showed that the grains were aligned in the extrusion direction……...62

Figure 5.4 An overview image of Z 7075-AD #12 and the 3d rendering showing the spike of the topography…….63

Figure 5.5 The fracture surface of the as-deposited 7075 material taken at 1000X, showing the flat tread and the sheared riser of the fracture surface……...63

Figure 5.6 The microstructure of the as-deposited AFSD Z 7075-AD #12 material etched with Weck's reagent showed a very fine-grained size at 150X……64

Figure 5.7 The overview image of Z 7075-T6 #4 was flat in appearance (left) with a shear lip all the way around the perimeter (right)……65

Figure 5.8 The fracture surface at 1000X was smooth and slightly faceted in appearance, which indicates brittle failure……...65

Figure 5.9 The microstructure of the heat treated sample of Z 7075-T6 #4 at 150X etched with Weck's revealed fracture occurring at the grain boundaries……66

Figure 5.10 An EDS map showing of the wrought 7075-T6 sample #4 had particles that were rich in Mg and Si and there were smaller Mg, Zn, and Cu rich particles dispersed throughout the fracture surface……...67

Figure 5.11 An EDS map showing that the particles were rich in Mg and Si and there were smaller Mg, Zn, and Cu rich particles were dispersed throughout the fracture surface of sample AFSD Z 7075-AD #9……67

Figure 5.12 An EDS map of the heat treated material showing Mg and Si rich large particles with smaller Mg, Zn, and Cu rich particles dispersed throughout the fracture surface in sample AFSD Z 7075-T6 #4……68

Figure 5.13 The fracture surface was flat with dark lines running across the surface that pointed towards the outer edge (red arrow)……69

Figure 5.14 Sem image of the fracture surface at the fracture initiation site (a) 50X and its appearance at higher magnifications (b) 500x……...70

Figure 5.15 An EDS map showing a carbon rich area along with the expected Mg, Si, Zn and Cu elements……70

Figure 5.16 The cross section of the fracture surface at 150x with a Keller's etch revealed a fine grain structure……71

Figure 5.17 An overview of the fracture surface (left) and the 3d rendering of the red circled 'waved' section (right)……...72

Figure 5.18 The fracture surface at 50X (left) and the fracture surface at higher magnification showing a smooth appearance 1000x (right)……73

Figure 5.19 EDS map of the dark section of the wave outlined in red did not show a difference in chemistry or carbon in high amounts……73

Figure 5.20 Sample AFSD Z 7075-T6 #14 near the fracture surface etched with Weck's and at 150X showed failure occurs at the grain boundaries……74

Figure 5.21 The fracture surface of the AFSD Z 6061-T6 #15 material and the topographical 3D rendering of the initiation site……75

Figure 5.22 The initiation of the fracture was smooth in appearance (top) 55x and at higher magnification is appears to have a smooth granular appearance (below) 2000X……..75

Figure 5.23 The EDS map showed expected elements with very little carbon or oxygen……76

Figure 5.24 The cross section of the fracture surface at 150x after etching with Weck's reagent revealed that fracture was along the grain boundaries……...76

Figure 5.25 The unetched AFSD Z 7075-T6 #4 did not have noticeable banding of carbon particles at 20X……..77

Figure 5.26 The outlier sample had lines where carbon was deposited in the microstructure of the unetched samples #14 at 2.5X (above) and 10X (below)……..78

Figure 5.27 The Raman shift for the graphite spray as sprayed (a) after heat treatment (b), and the dark particles suspected to be carbon (c) in the unetched microstructures……..79

Figure 6.1 The dotted line is located at the working temperature for 6061 and the solid line was the the working temperature for 7075……80

Figure 6.2 The proposed mechanism of failure shows that at the fracture surface it has a stepped appearance due to the delamination of the layers……..83

Figure 6.3 The proposed mechanism of failure shows that at the fracture surface elastic spring bake causes the secondary cracks in the fracture surface……..84

Figure 6.4 AFSD X (left) #2-1 annealed, (right) #2-2 fully heat treated showing the change in grain size……85

Figure 6.5 AFSD Z 6061 (left) #11 annealed (right) #9 fully heat treated at 2.5X showing the change in grain size……86

Figure 6.6 AFSD Z 7075-AD #12 (left) after annealing and AFSD Z 7075-T6 #14 fully heat treated (right) etched with Weck's reagent imaged at 150X showing the change in grain size……86

List of Tables

Table 3.1 AFSD, wrought and standard 6061 chemistries as wt.% as determined through OES……19

Table 3.2 AFSD, wrought and standard 7075 chemistries as wt.% as determined through OES……19

Table 3.3 Dimensions for the standard specimen and the small size specimen……21

Table 3.4 The condition, name, and build location of the samples tested for 6061 alloy…….21

Table 3.5 The condition, name, and build location of the samples tested for 7075 alloy…….21

Table 4.1 Selected mechanical properties of 6061 aluminum……...27

Table 4.2 The average mechanical results of the material and the calculated quality index values…….28

Table 4.3 T-test results of the Z and X directions in the as-deposited conditions…….29

Table 4.4 T-test results of the Z and X directions in the heat treated condition……31

Table 4.5 The Youngs Moduli of the samples with percent error off the literature value…….32

Table 5.1 Selected mechanical properties of 7075 aluminum……...55

Table 5.2 The Average mechanical properties and calculated quality index values for the 7075 AFSD and wrought material……..56

Table 5.3 As-deposited AFSD material compared to wrought material in annealed condition…57

Table 5.4 T-test results for the AFSD and wrought material after heat treatment……58

Table 5.5 T-test results for the AFSD and wrought material after heat treatment with the outliers removed……..59

Table 5.6 The difference between measured AFSD material compared to the literature value…59

Table 5.7 The t-test results that compared the elastic modulus of the AFSD material to the wrought material before and after heat treatment……..60

Table A.1 Published literature values of AFSD 6061 material…….95

Table A.2 Published literature values of AFSD 6061 material…….96

Table B.1 AFSD X 6061-AD Tensile Results……...97

Table B.2 AFSD Z 6061-AD Tensile Results……...97

Table B.3 AFSD X 6061-T6 Tensile Results……97

Table B.4 AFSD Z 6061-T6 Tensile Results……97

Table B.5 Wrought 6061-T6 Tensile Results……98

Table B.6 Wrought 6061-O Tensile Results…….....98

Table B.7 AFSD Z 7075-AD Tensile Results……...98

Table B.8 AFSD Z 7075-T6 Tensile Results…….99

Table B.9 Wrought 7075-T6 Tensile Results……99

Table B.10 Wrought 7075-O Tensile Results……99

Table B.11 General steps used to polish the as-deposited and heat treated material……...100

Table B.12 The etchant name and chemical composition used for the 6061 and 7075 etching of the AFSD material……...100

List of Equations

Eq 3.1 Initial quality index calculation, Q_O……...24

Eq 3.2 Calculation for the dimensional factor, K_D……24

Eq 3.3 Final quality index calculation, Q_D……24

Chapter 1 Introduction

1.1 Motivation

The goal of this research is to aid in the development of the large-scale additive manufacturing of jointless underbody hulls for the Army Ground Vehicle Systems by generating an improved mechanical and metallurgical understanding of the Additive Friction Stir Deposition (AFSD) process. This project was supported by the Applied Science and Technology Research Organization of America (ASTRO America), the American Lightweight Materials Manufacturing Innovation Institute (ALMII), and the US Army CCDC-GVSC (GVSC). These groups have in turn partnered with Ingersoll Machine Tool (Ingersoll), Meld Manufacturing (MELD), and Siemens Digital Industries (Siemens) to evaluate the feasibility of large-scale additive manufacturing. As part of the Jointless Hull program, Meld Manufacturing's AFSD process was selected as the additive technology most likely to meet combat vehicle scale manufacturing capabilities. The results of this project will be used to aid in determining material design choices for large-scale additive manufacturing using the AFSD process.

1.2 Jointless Underbody Hull Project

Aluminum underbody hulls for ground vehicles first saw combat in Vietnam where they were used on the M113 [1]. The use of aluminum as opposed to steel was to reduce weight to allow for the M113 to be airlifted into combat [1]. Although the weight reduction increased the speed and maneuverability, the use of aluminum left the underbody vulnerable to blasts. In fact, 73% of all vehicle losses in the Vietnam war were from anti-tank mines, Figure 1.1 [2].

The Jointless Underbody Hull project was started to push the limits of the more mature manufacturing methods, such as welding, forming, and forging. Redesigns included increasing the thickness of the underbody, adding steel reinforcing plates, and reducing or eliminating welds [3]. The largest forged underbody hull, Figure 1.2, is an example of this project [4].

However, even with full effort, this most recent project took 6 months from design to completion to produce a testable product [3]. Due to the speed by which new designs are needed and the sheer volume required, current manufacturing methods cannot meet the demands promptly manner. For these reasons, the program added additive manufacturing methods.

Figure 1.1 M113 knocked out of service from underbody mines during Tet fighting, 1968 (Photo courtesy of the National and Calvary Museum) [2].

Figure 1.2 The largest forged underbody hull was created jointly with ALCOA and the GVSC [3], [4].

1.3 Large-Scale Additive Manufacturing

The selection of an additive manufacturing process was based on its scalability for large additive manufacturing of metal. There is currently a lot of interest in metal additive manufacturing to take advantage of potential weight savings, complex part re-designs, and rapid prototyping. There are few metal additive manufacturing processes that have the capacity for scalability to the large-scale. Of these, Wire Arc Additive Manufacturing (WAAM), Ultrasonic Additive Manufacturing (UAM), Electron Beam Additive Manufacturing (EBEAM), and Additive Friction Stir Deposition (AFSD) have seen applications and demonstrations for the large-scale, Figure 1.3 [5]–[10].

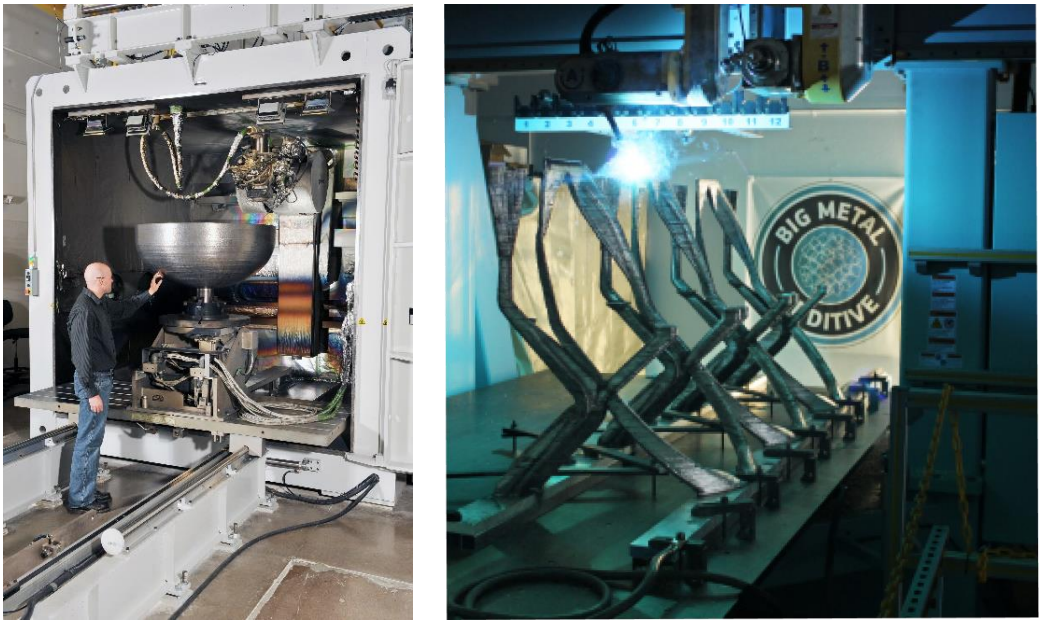

Figure 1.3 A fuel tank made from EBAM (left) and securing brackets made from WAAM (right) [11], [12].

There are certain parameters that the Jointless Underbody Hull project indicated that would allow a metal additive process to scale to the sizes needed to produce underbody hulls. The main parameters are to minimize residual stresses, porosity, and defects, while also lowering the cost of processing and postprocessing times and expenses. For AM processes that require a melt pool of the solid feedstock material, such as WAAM and EBEAM, rapid liquefication and solidification of the feedstock material introduces high internal stresses, directional solidification, and porosity that detrimentally affects the final properties of the part [6], [13], [14]. These parts often require special post-processing, such as Hot Isostatic Pressing, to heal internal porosity and relieve stresses [15]. For processes that require a closed environment, such as EBEAM, the part design is limited by the building envelope and a new build space needs to be built to scale up, which increases costs [16]. Another issue is the fact that these beam-based processes require constant monitoring as defects are difficult to remove once made however, there current research on advanced monitoring systems for these processes is still in its infancy [6], [7], [17]. Feedstock handling is also very important due to the sheer volume required for

large builds. AM processes that require special materials make procurement difficult which hinders the production of large parts in a timely manner.

Additive Friction Stir Deposition (AFSD) was selected as it allows for scalability. AFSD is a solid-state process that has the potential for lower residual stresses and lower porosity than the beam-based processes [18], [19]. AFSD also does not require a controlled atmosphere for aluminum depositions and can deposit at speeds of >1000 cm^3/hr. (61 in^3/hr.) [20]. Additionally, the AFSD process can deposit commercially available materials, which require only minimal preparation, such as a general acetone cleaning, and can deposit both solid and powder feedstock [21], [22]. For all these reasons, the Jointless Underbody Hull program selected the AFSD process and commissioned two machines that will produce underbody hulls. Both machines will be outfitted with an AFSD deposition head and a CNC machine to allow for both additive and subtractive manufacturing. The first and smaller machine is for general prototyping and to allow production engineers to dial in the process parameters and a larger one will be for general production. A smaller research system that will have a build volume envelope of 2'x3'x3' will be located in the new Advanced Manufacturing Commercialization Center [23]. Figure 1.4 shows a 3D rendering of the larger production machine that will have a volume of 20'x30x10' and will be located at the Rock Island Arsenal [23], [24].

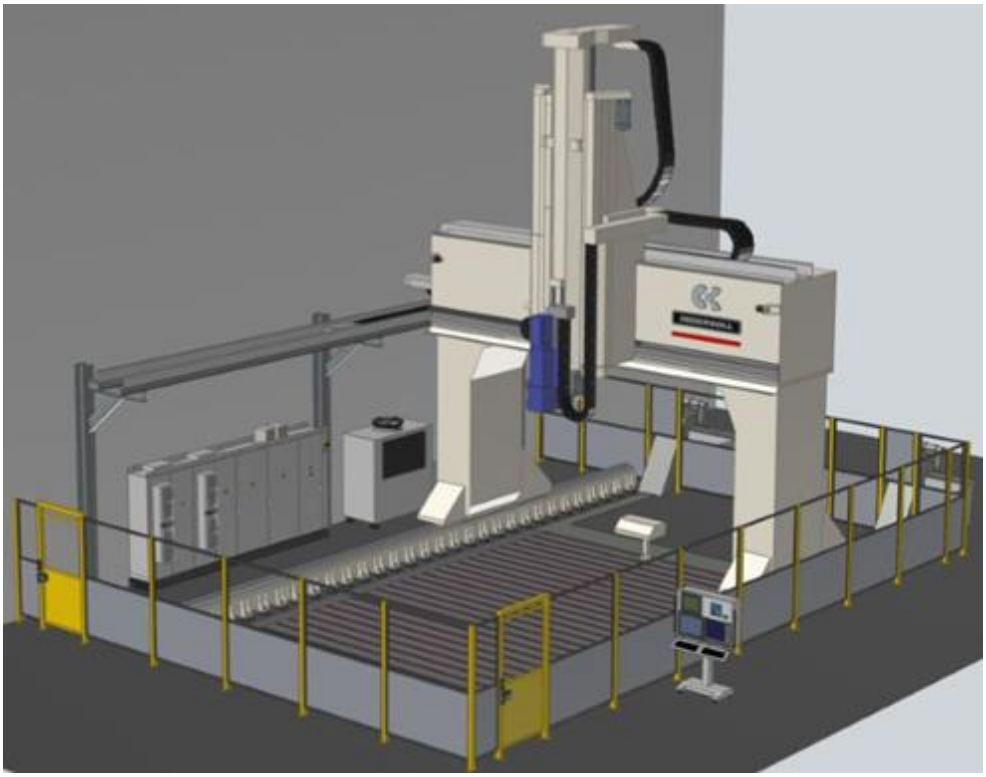

Figure 1.4 A 3D rendering of the AFSD system that will be the largest AM metal system ever built to-date [25].

Chapter 2 Literature Review

2.1 Additive Friction Stir Deposition Process

Additive Friction Stir Deposition (AFSD) is an additive process that is considered a hot working process like forging due to its high processing temperature and severe material plastic deformation. The process works by pushing a square feedstock rod through a rotating hollow shoulder. The material is heated through interfacial friction between the feedstock, baseplate, and the tool head to produce volumetric heating of the material [26]. Once heated, the material begins to yield at which point it is then deposited onto a preheated baseplate. This process of heating, yielding, and depositing occurs layer by layer until the final part is completely formed. The temperature of the deposit is controlled by the spindle tool head speed (Ω) and the travel velocity (*V*). Another current focus of research is using AFSD for on-site repairs like Friction Stir Welding (FSW) [27].

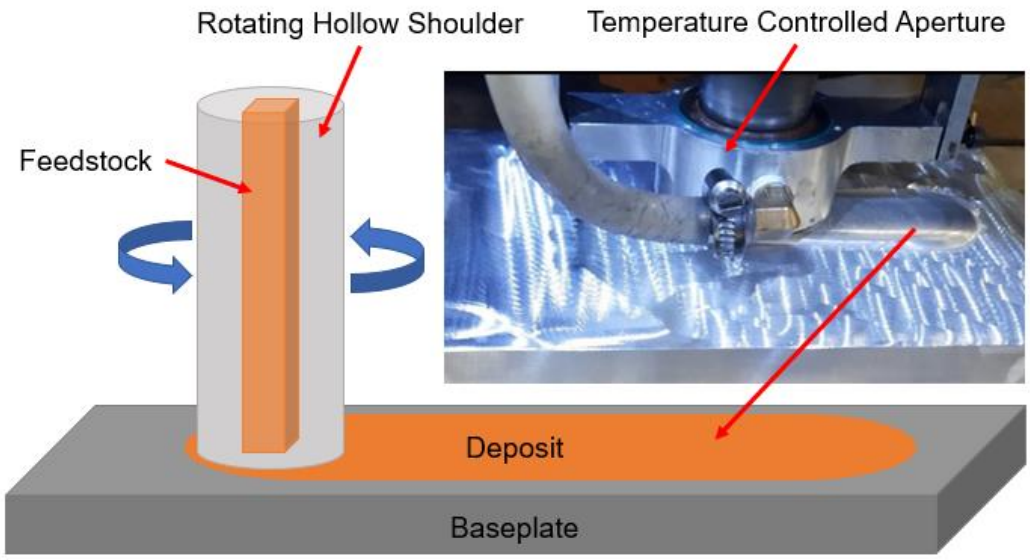

Figure 2.1 The deposition of 6061 aluminum with a temperature controlled aperture that changes the spindle tool head speed (Ω) and the travel velocity (V) to adjust the working temperature. {Image recreated from MELD Manufacturing white papers}

2.2 AFSD Microstructural

One area of interest is the characterization of the microstructure after severe deformation and heat are applied to the material. The AFSD process produces a fine equiaxed grain structure and is credited with reducing the grain size of the feedstock material of various materials from 100-200 μm to 1-5 μm [18], [28]–[31]. The refined microstructure is due to dynamic recrystallization (DXR) which is the process by which the cell walls of the larger grains are deformed and form a smaller subgrain structure [19], [32]. Materials with high stacking fault energies (SFE), such as Aluminum and α-Fe, tend to cross-slip dislocations more readily and allow for the refinement of the grain structure when strain is applied. Figure 2.2 shows the formation of these subgrains with increasing strain in hot-worked high-SFE materials which is the expected method by which hot-working refines the grains [32]. Figure 2.3 shows the EBSD images of AA2024 feedstock and deposited material after AFSD processing [28].

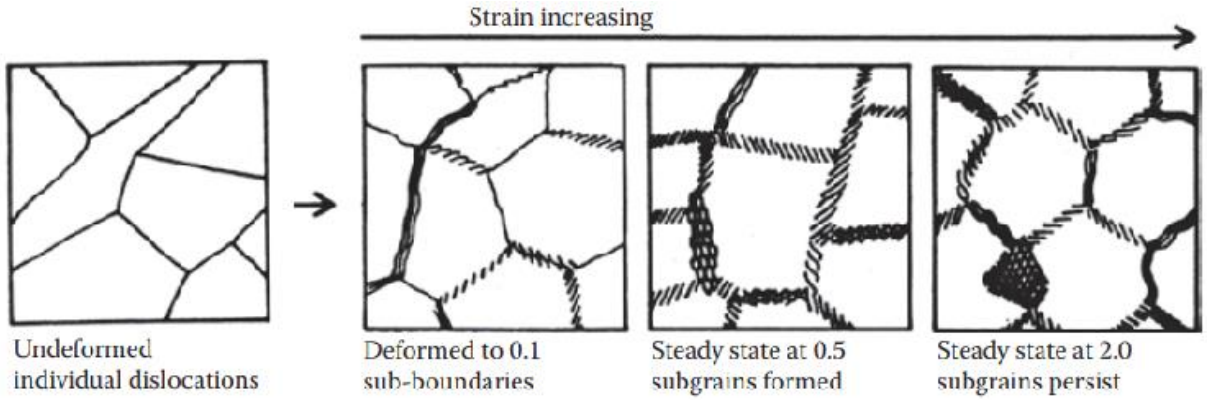

Figure 2.2 The formation of subgrains in a hot worked material with increasing strain [32].

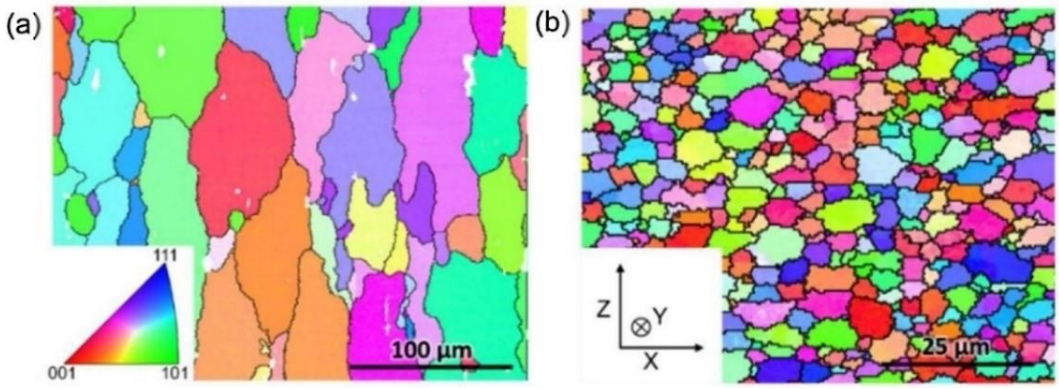

Figure 2.3 EBSD images of the undeformed 2024 material (a) and then the dynamically recrystallized equiaxed grain structure after processing with AFSD (b) [28].

2.3 AFSD Mechanical Properties

There is very little mechanical data on the AFSD process in the as-deposited condition and even less in the heat treated condition. Most of the mechanical property data published has been generated from non-standard small tensile bars or modified fatigue specimens to save on material and time, Figure 2.4. In addition, very little data has been published for 6061 and 7075 aluminum that shows the mechanical properties of the bulk material deposit. The current research focus is often on interface interactions between the initial layers and the baseplate, investigation of its application for onsite weld repair or direct recycling, or general microstructural characterization of the AFSD process [26], [28]–[31], [33]–[39]. Table A.1 and A.2 in Appendix A list the mechanical properties, the tool head speed (Ω), the travel velocity (*V*), and any standards used to heat treat or test the tensile properties of the 6061 and 7075 AFSD materials from published literature [21], [31], [34], [40]–[43]. It should be noted that for the use in this thesis, any mechanical data from investigations of crack or hole repair were excluded.

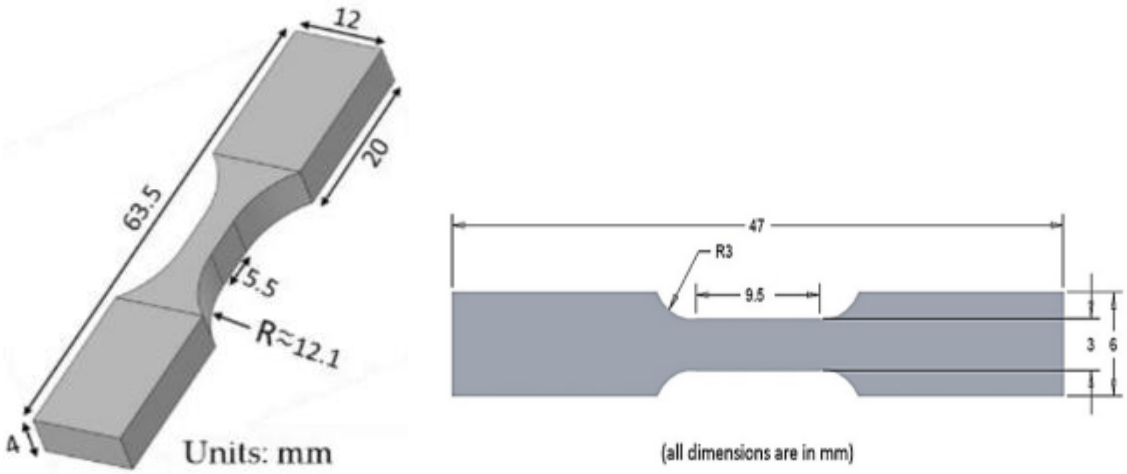

Figure 2.4 Modified fatigue specimen used for testing the tensile strength of AFSD material used in most published literature [21], [31], [34], [40]–[42].

A major issue with the current mechanical properties generated in the literature is that the tensile specimens used do not meet the ASTM standards for tensile testing. The values calculated from the stress-strain curves generated are elastic modulus, 0.2% offset yield strength, ultimate tensile strength, and elongation at failure. Of these, yield and elastic modulus can only be determined if a strain gauge or extensometer was used. In addition, even though all of the published data in Tables 2.1 and 2.2 used strain gauges or extensometers, the small size of the samples and the fact that they are not proportional to standard tensile bars, they often produce inaccurate and highly variable values [44]–[46]. Higher variability is due to microstructural discontinuities, surface roughness, and improper machining that have a greater effect on the mechanical properties in smaller cross-sections. In addition, most samples were prepared with electric discharge machining (EDM) to cut out the flat thin specimens. If there is a heat affected zone, even a small amount, from the EDM this can affect the as-deposited and heat treated condition of the sample to a significant effect on small cross-sections [47]–[49]. Elongations values are also extremely sensitive to geometric changes [45], [46], [50]. For these reasons, only

the ultimate strength values in the literature can be reasonably compared between papers and to the standard published values.

Figure 2.5 and Figure 2.6 are the ultimate tensile strengths of the published literature and the values presented in this thesis for comparison. The name under the data lists the author's last name, the sampling direction, and the condition either as-deposited (AD) or heat treated (T6). Error bars were added to these Figures if it was listed in the published document. Of these, we see that the as-deposited condition of the 6061 and 7075 material is generally low strength. The as-deposited 6061 material also shows a slight increase in the strength values with the samples in the longitudinal (X) direction compared to the transverse direction (Z). After heat treatment, the 6061 material in Beck et al and the data generated in this thesis were lower compared to the wrought material [42]. The 7075-T6 in Yoder et al and the work from this thesis achieved strength values more similar to a wrought 7075 material of similar heat treatment [43].

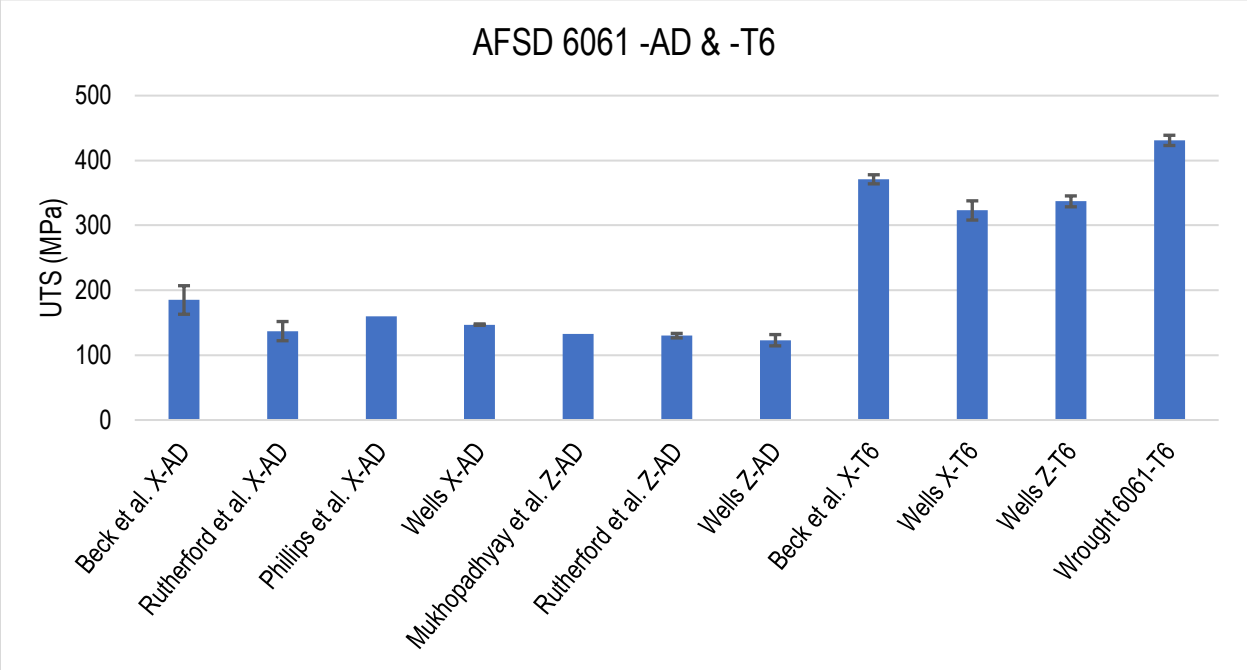

Figure 2.5 Ultimate tensile strength of the AFSD 6061 material in various orientations and conditions.

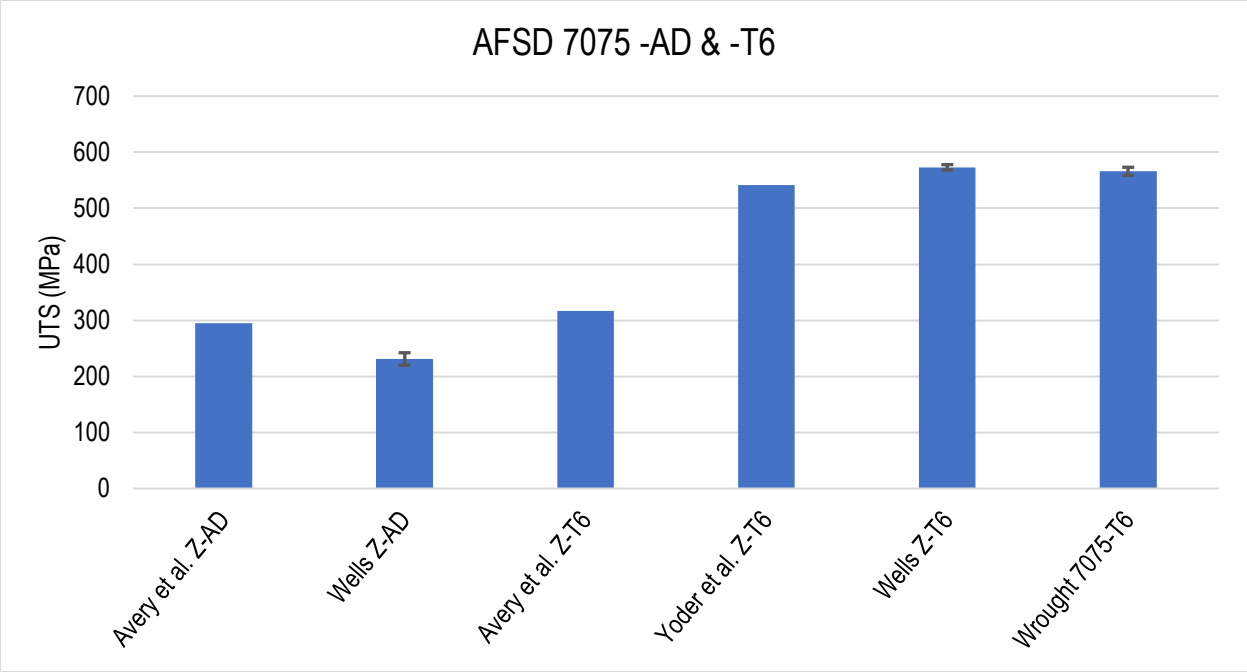

Figure 2.6 Ultimate tensile strength of the AFSD 7075 material in various orientations and conditions.

2.4 Hot Working of Aluminum

The process of hot working is defined as deforming a material at temperatures greater than $0.6T_M$. According to works published by Garcia et al., the heat generation from the interfacial heating by changing the tool head speed (Ω) and travel velocity (V) of the AFSD process produces temperatures in the range of 50-70% of the melting point of 6061 aluminum [26]. In addition, recent adjustments to the MELD tool head allow for control of these parameters in situ to control the temperature of the deposition at the tool head. For this study, the working temperature for the 6061 material was kept at 470 ^{o}C (842 ^{o}F) which is roughly 55% of the melting temperature and for the 7075 material was kept at a lower working temperature of 425 ^{o}C (797 ^{o}F) which was roughly 90% of the melting temperature. Research has also shown that the strain rate of this process is extremely high and there are few material flow constraints on the deposit except at the interface between the baseplate and the deposit [26].

For these reasons, AFSD is like a hot working process, such as open die forging. In terms of microstructure, the as-deposited AFSD material is similar in appearance to a forged product. Figure 2.7 shows the 6061 material in the as-deposited condition and a forged aircraft part both sectioned and etch to reveal the grain structure [51]. This appearance is attributed to grain flow which is characterized by the fiber-like grain structure that is aligned in the principle direction of the material flow [52], [53]. This directionality can produce some strengthening due to grain refinement in the direction longitudinal (X) to the direction of the grain flow. However, in hot-working the strength and hardness of the material are primarily controlled by the alloy chemistry and heat treatment [52]. This is due to the fact that the high levels of dynamic recovery (DRV) during hot working reduce the hardening effect in high SFE materials [32], [52].

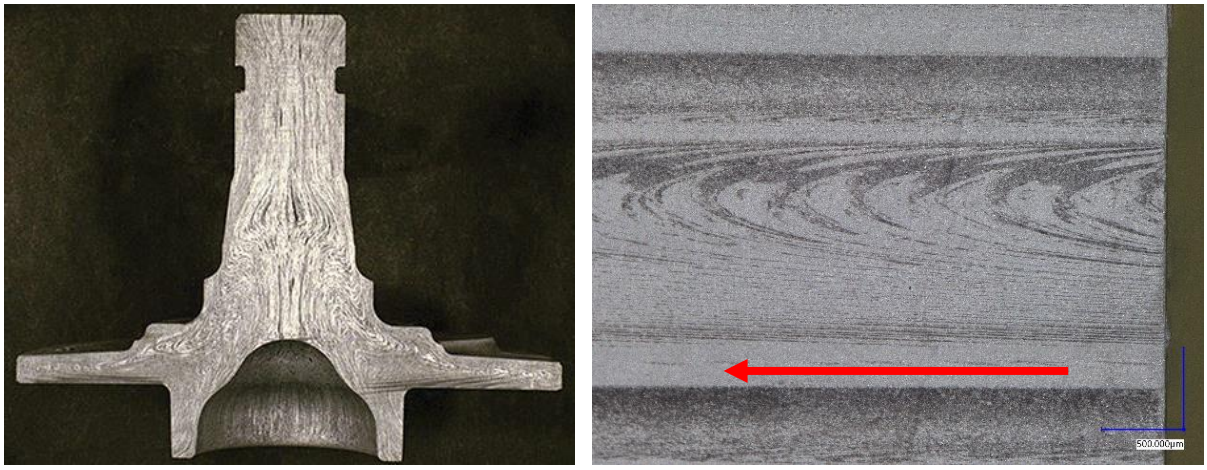

Figure 2.7 The forged aircraft grain structure (left) and the AFSD 6061 with noted layer direction (right) [51].

2.5 Precipitation Strengthening Heat Treatment

This thesis also investigates the effect of heat treatment on the mechanical properties of AFSD builds. The alloys in this thesis are both precipitation hardening heat treatable alloys, 6061 and 7075. The heat treatments of these alloys involve a solutionizing step just below the eutectic melting point that places the alloying elements into the solution [54], [55]. A rapid quench in

water or a polymer quenchant from the solutionizing temperature creates a super saturated solution (α_{ss}). Subsequent room temperature (natural) or elevated temperature (artificial) aging, forms GP zones that are coherent with the aluminum matrix. From these GP zones, the strengthening precipitates form which increases the strength of the material as they help to pin and mitigate the movement of dislocations. The quench rate is very important as a fast quench rate forms vacancies in the matrix that allows for nucleation sites and allows for fast diffusion of the elements during the ageing process [52], [55].

The Al-Mg-Si alloy 6061 has more Mg and Si and additions of Cu than the other 6xxx series wrought alloys. The increase in alloying elements and minor additions of Cu allows 6061 to achieve higher strengths. The precipitation reactions for 6061, show the process by which the main strengthening particle β" forms first.

$$\alpha_{ss} \rightarrow (Mg) + (Si) + (Si, Mg) \rightarrow GP\ zones \rightarrow\ \beta'' \rightarrow \beta' \rightarrow \beta(Mg_2Si)$$

The 7075 alloy is an Al-Zn-Mg-Cu alloy that produces the highest strengths out of all the wrought aluminum alloys [52]. Upon quenching and aging, the Zn forms GP zones and Mg migrates to these zones. The equilibrium and incoherent phase $Mg(Zn,Cu,Al)_2$ phase η forms during aging. The typical process for the precipitation reaction of the main strengthening phase η' in 7075 is as follows;

$$\alpha_{ss} \rightarrow GP \rightarrow \eta' \rightarrow \eta$$

Something important to note for the 7075 alloy is that after hot working there is often a hard intermetallic phase called Al_2CuMg which is slow to dissolve. This phase forms platelets that are found on grain boundaries and can act as stress risers [55]–[57]. Slow heating rates to the

solutionizing temperature are important as they allow this intermetallic phase to completely dissolve [56]. For this reason, the samples were placed in the furnace while the soak temperature was reached with a calculated ramp rate of 15 ^{o}C/min.

Chapter 3 Methods

3.1 AFSD Builds

Additive Friction Stir Depositions (AFSD) were performed by MELD Manufacturing Corporations (Christiansburg, VA, USA) on a MELD SB2 discontinuous system. Two different rotating hollow shoulder tool head designs were used. The (1.5 inches) 38 mm tool head with 4 protrusions that were 0.09" high was used for the 6061 builds and the 7075 builds used 0.025" high nubs. The temperature for the build was controlled with a thermocouple in the tool head that adjusted the travel velocity and spindle speed of the tool head. The feedstock material was 0.5" (12.7 mm) solid square bars in the T6 temper for both 6061 and 7075 alloys.

3.1.1 6061 Builds

No graphite was used to lubricate the feedstock material for the 6061 builds. The process parameters were adjusted to maintain the tool head temperature. For the first layer that penetrates the base plate, the tool head was kept at 450 ^{o}C (842 ^{o}F). The second layer was kept at 460 ^{o}C (860 ^{o}F). The tool head was then raised to 470 ^{o}C (878 ^{o}F) for all the remaining layers. The layer height for all the builds was 2 mm (0.08 in).

The samples used to test the mechanical strength in the direction along the tool head path (X) were made in November of 2021 which were 5 single track walls 8" long and over 1" tall (20.32 x 2.54 cm). From each build, two 0.5" diameter round tensile bars were machined along the direction of the tool path from the top and bottom sections. The first and last inch of material on the builds was not included in the sampling. Figure 3.1 shows the location of the tensile bars in the builds. It is important to note that the samples were marked with two numbers where the first number was which build it came from and the second number was either 1 from the lower section or 2 from the upper section.

The Z direction builds were from two single track walls 10” long and over 6” tall made in October of 2022. From each build, 0.5” diameter round tensile bars were machined transverse to the layer direction which is noted as the Z direction. Figure 3.1 shows one of the builds and the orientation of the tensile bars. From the remaining material, samples 1-10 were cut from the 1st build, and samples 11-16 were cut from the second build. The remaining section was set aside for ballistic testing which will not be discussed in this thesis.

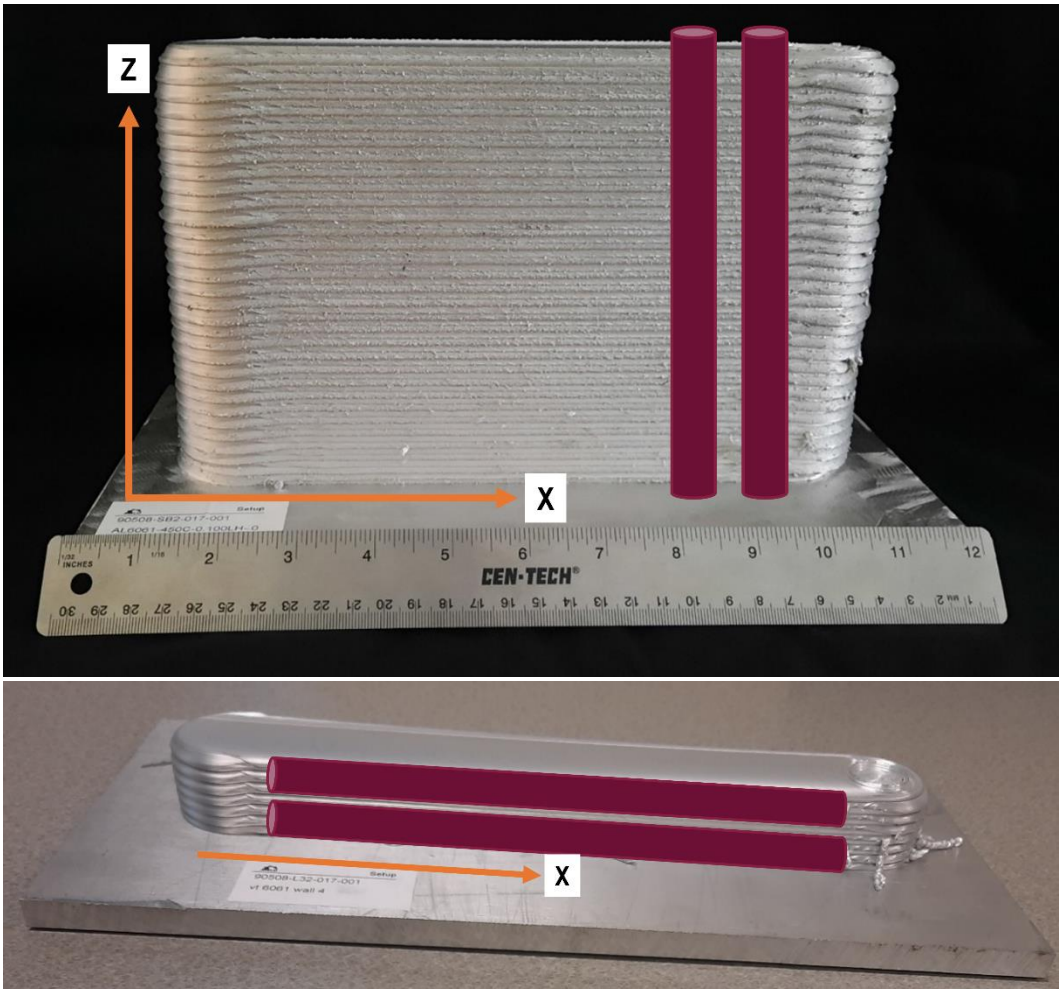

Figure 3.1 The single wall build for the Z direction samples (above) and the X direction samples (below) showing the orientation of the tensile bars.

3.1.2 7075 Builds

A “medium” graphite layer was used on the feedstock material for the 7075 builds. Additionally, only walls were built to test the Z direction to test the mechanical properties of the AFSD process, Figure 3.2. The tool head for the 7075 builds was maintained at 435 ºC (815 ºF) for each layer. Only 2 builds that were 12" long and 6.2" in height (30.48 x 15.75 cm) were made of 7075. From each build, 0.5” diameter round tensile bars were machined transverse to the layer direction. The substrate material was included in the profile of the grip section of the tensile bar. From the first, build, samples number 1-12 were taken. The second build had tensile specimens 13-17 and the remainder was used for ballistic testing that will not be discussed in this thesis.

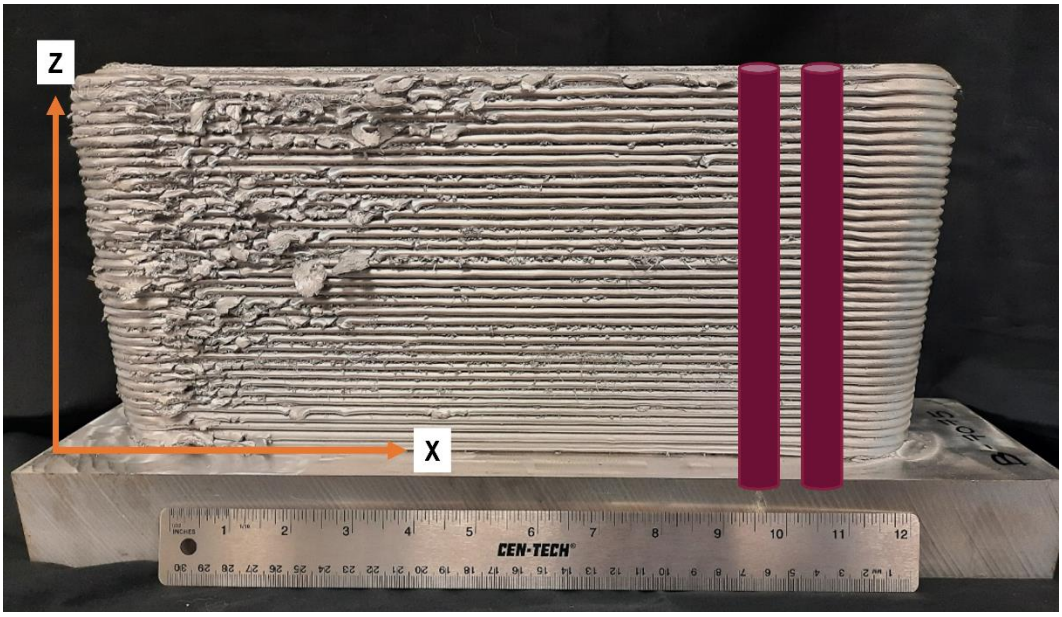

Figure 3.2 The Z direction single track build made of 7075 showing the orientation of the tensile bars.

3.2 Heat Treatment and Chemistry

All heat treatment was done in an air circulating furnace at the Kroehling Advanced Materials Research Foundry. Before heat treatment all the builds were sectioned into square bars over 0.5” thick. Wrought 0.5” diameter round bars of similar chemistries were also heat treated alongside the AFSD material to confirm if the heat treatment used was able to meet industry

standards. All samples were heat treated in accordance with forging heat treatment specifications to achieve standard mechanical values [58], [59]. This involved an annealing step to relieve any residual stress before the precipitation heat treatment. All samples were solutionized before quenching in room temperature water and were artificially aged. The chemistries of the AFSD builds and the wrought material were measured with an OES spectrometer. The results for the 6061 and 7075 alloys are reported in Table 3.1 and Table 3.2. The ASTM specification for the chemistry is listed and it should be noted that specifications values that are not presented as a range are a maximum value [60]–[62].

Table 3.1 AFSD, wrought and standard 6061 chemistries as wt.% as determined through OES.

	Si	**Mg**	**Fe**	**Cu**	**Cr**	**Zn**	**Ti**	**Mn**	**Al**
AFSD X 6061-AD	0.61	0.80	0.36	0.23	0.06	0.03	0.03	0.09	Bal
AFSD Z 6061-AD	0.75	0.81	0.36	0.25	0.06	0.03	0.03	0.07	Bal
Wrought 6061	0.73	0.84	0.22	0.27	0.09	0.04	0.02	0.10	Bal
Specification [60]–[62]	0.4-0.8	0.8-1.2	0.7 max	0.15-0.40	0.04-0.35	0.25 max	0.15 max	0.15 max	Bal

Table 3.2 AFSD, wrought and standard 7075 chemistries as wt.% as determined through OES.

	Si	**Fe**	**Cu**	**Mn**	**Mg**	**Cr**	**Zn**	**Ti**	**Al**
AFSD Z 7075-AD	0.10	0.21	1.26	0.03	2.40	0.20	6.01	0.04	Bal
Wrought 7075	0.07	0.13	1.28	0.02	2.36	0.20	5.87	0.03	Bal
Specification [60]–[62]	0.40 max	0.50 max	1.2-2.0	0.30 max	2.1-2.9	0.18-0.28	5.1-6.1	0.2 max	Bal

3.2.1 Heat Treatment of 6061

The annealing step was performed at 413 ^{o}C (775 ^{o}F) for 3 hours and allowed to air cool to room temperature. The material was then solutionized at 527 ^{o}C (980 ^{o}F) for 1 hour and then quenched in water. The samples were then immediately aged in a 178 ^{o}C (350 ^{o}F) furnace for 8

hours followed by air cooling to room temperature. The time required to reach soak temperature was determined with an embedded thermocouple in a sample puck of equal dimensions.

3.2.2 Heat Treatment of 7075

Two different batches of 7075 were heat treated. The first batch was aged immediately after solutionizing. This was a mistake on the author's part and may have affected the scatter in the tensile results. A second batch of AFSD and wrought material was annealed, solutionized, quenched, and then allowed to naturally age for 24 hours before artificially aging. The annealing step was done at 413 ^{o}C (775 ^{o}F) for 2 hours followed by air cooling to room temperature. The material was then solutionized at 471 ^{o}C (880 ^{o}F) for a minimum of 25 minutes. The samples were then artificially aged in a 124 ^{o}C (255 ^{o}F) furnace for a minimum of 22 hours before air cooling to room temperature.

3.3 Tensile Testing

The tensile bars were machined and tested in accordance with ASTM B557-15 standard test methods for tension testing wrought and cast aluminum and magnesium alloy products [50]. The tensile bars were a standard small-size specimen that was proportional to the standard round bar. Table 3.3 lists the dimensions of the standard specimen and the small size specimen used. Figure 3.3 shows a schematic of the round tensile bar. Table 3.4 and 3.5 lists the sample locations, testing conditions, and identification numbers of the 6061 and 7075 samples. In Table 3.5 numbers written in **bold** are from 7075 build 1.

Table 3.3 Dimensions for the standard specimen and the small size specimen [50].

	Standard Specimen	Small Size Specimen
Nominal Diameter	0.5	0.35
G – Gage length	2.000 ± 0.005	1.4 ± 0.005
D – Diameter	0.500 ± 0.010	0.350 ± 0.007
R – Radius of fillet, min	0.375	0.75
A – length of reduced section, min	2.25	1.75

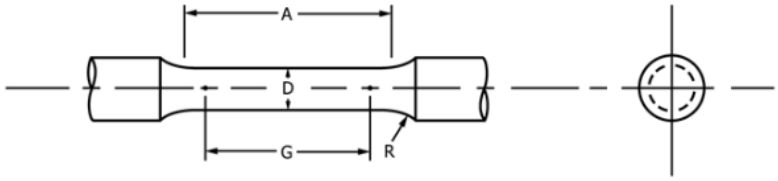

Figure 3.3 A diagram of the tensile specimen showing the important sample dimensions [50].

Table 3.4 The condition, name, and build location of the samples tested for 6061 alloy.

Name	Sample Number
AFSD X 6061-AD	1-1, 2-1, 3-1, 4-1, 4-2, 5-1
AFSD X 6061-T6	1-2, 2-2, 3-2
AFSD Z 6061-AD (Build 2)	11, 12, 13, 15
AFSD Z 6061-T6 (Build 1)	1, 2, 3, 4, 5, 6, 7, 8, 9, 10
Wrought 6061-T6	1, 2, 3, 4, 5, 6, 7, 8

Table 3.5 The condition, name, and build location of the samples tested for 7075 alloy.

Name	Sample Number
AFSD Z 7075-AD	**1, 2, 6, 9, 10, 12**, 13, 16, 17
AFSD Z 7075-T6	**3, 4, 5, 8, 11**, 14, 15
Wrought 7075-T6	1, 2, 3, 4, 5, 6, 7

Testing was conducted on an Instron series 4460 tabletop load frame system with a 50 kN load cell at the Busting Lab in Norris Hall at Virginia Tech. Strain measurements were done with an MTS axial clip-on extensometer with a 1” gauge length. For the 6061 materials, both the X and Z direction were tested in both the as-deposited and heat treated conditions. For the 7075 materials, only the Z direction was tested in both the as-deposited and heat treated conditions. Wrought bars of similar chemistries were tested in the annealed and heat treated conditions

alongside the AFSD material. The wrought material was used to confirm the heat treatment procedure and make a direct comparison to industry wrought material.

The current research focus on the AFSD process and its capabilities for repair and thus the interface between the baseplate and the deposited material is often the focus of mechanical testing. The purpose of this project was to gather data for the use of large-scale additive applications by providing industry standard mechanical property data to compare to other aluminum manufacturing methods. For these reasons, the location of the reduced section of the tensile bars was in the middle region of the build as that would provide a focus on the layer-to-layer properties. However, the author would like to acknowledge that due to the difference in thermal history between the initial and uppermost layers the mechanical properties may vary as a function of location.

3.4 Mechanical Properties

The complete lists of all the mechanical properties for each tensile specimen are listed in Appendix B. Figure 3.4 shows the graphical methods used to determine the mechanical properties from the stress-strain graph generated from the tensile testing. The Young's modulus, E, was graphically determined from the linear slope of the stress v. strain curves in the elastic region. The yield strength, R_Y, was calculated using the 0.2% offset method and the calculated Young's modulus. The ultimate tensile strength, R_{UTS}, was the maximum stress value recorded during testing. The elongation at fracture, A_{at}, was graphically determined as the point at which there was a sudden decrease in force on the stress-strain graph. Elongation after fracture, A_{after}, was calculated by placing the broken fracture surfaces together and measuring the change in length of the gauge marks. The strain energy density, W, was calculated from the area under the stress-strain curve until elongation at fracture. For elongation at fracture, it is required that an

extensometer remain attached to the specimen throughout testing, however, it does not measure the exact elongation at break unless the break occurs within the extensometer gauge length. Because of this, elongation at fracture is almost always lower than the actual elongation. For this reason, the elongation after fracture, $A_{after,}$ was used to compare the results to literature values while the A_{at}, was used to calculate the strain energy density.

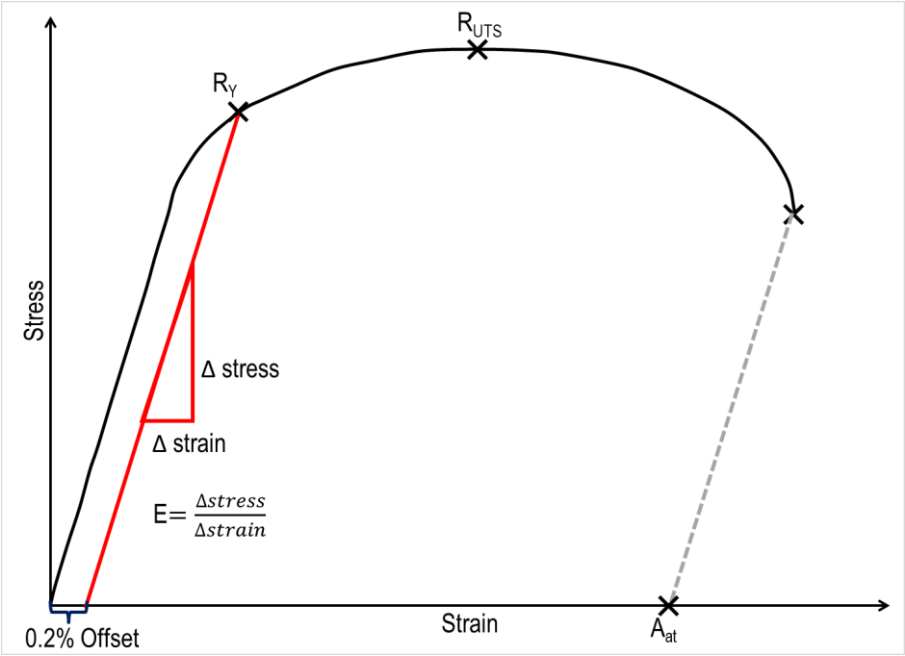

Figure 3.4 The methods used to calculate the E, 0.2% offset Yield strength, Ultimate tensile strength, and Elongation at fracture.

3.5 Quality Index

To better understand the AFSD material and compare it to the wrought product, a quality index was used to provide an understanding of the strength to ductility tradeoff as well as the scatter in the data. There were notable outliers in both the 6061 and 7075 AFSD material. The removal or inclusion of these outliers in the averages will be discussed in a later section. The quality index used for this thesis was derived from Alexopoulos and Pantelakis [63], [64].

The initial quality index calculated with equation 3.1, uses the yield strength and strain energy density to compare the strength to ductility tradeoff of a material [64].

$$Q_O = R_Y + 10 * W \quad \text{(Eq 3.1)}$$

The equation to calculate the initial quality index, Q_O, uses the yield strength, R_Y, and the strain energy density, W, to generate an index that ranks strength to ductility. The multiplier, 10, is used to represent the typical values of R_Y /W ratio for the optimized aluminum alloys [63], [64]. This multiplier was used for both cast and wrought quality index calculations [63], [64]. The strain energy value is used instead of the elongation at fracture or elongation after fracture as it includes the entire tensile behavior of the material and not just the elongation. The yield strength is used instead of the ultimate value as yield strength is typically the mechanical property that is used to design components.

In addition to the initial quality index, references proposed a quality index, Q_D, that includes the dimensional factor, K_D, which is used to empirically relate the strength to ductility tradeoff. This factor is calculated using equation 3.2 [63], [64].

$$K_D = \left(\frac{R_{Y\,i}}{R_{Y\,max}} + \frac{W_i}{W_{max}}\right) \quad \text{(Eq 3.2)}$$

In the references, K_D uses the maximum values for W and R_Y, so that samples with a K_D value of 2 have the highest strength with the best ductility. The final quality index, Q_D, was calculated with equation 3.3. This final index should rank the material with the best strength to ductility tradeoff and with the least amount of scatter as the highest.

$$Q_D = Q_O * K_D \quad \text{(Eq 3.3)}$$

3.6 T-Test

While the quality index is beneficial for understanding how the AFSD and wrought material compare, another method was needed to compare the statistical significance of the

difference. A T-test with a 95% confidence interval assuming unequal variance was used to compare the mechanical values between the X and Z directions in the as-deposited and heat treated conditions as well as compare the AFSD material to the wrought material in similar conditions (annealed or heat treated). For this, a p-value below 0.05 indicates that there is a statistically significant difference between the two data sets.

3.7 Fractography

Postmortem fracture analysis was done on the tensile specimens to determine fracture mode. One side of the fracture surface was preserved for imaging and particle analysis and the other side was mounted in epoxy for microstructural analysis.

Optical images were taken on the Keyence 3D surface profiler VK-X3000 in the Material Characterization Lab. This confocal microscope used focus variation to generate a Z-stacked image of the fracture surface and produced a 3D rendering of the topography of the fracture surface. ImageJ was used to stitch together some of the images of samples that could not be imaged in one frame [65].

3.8 Particle Analysis

High-resolution images and particle analysis of the fracture surfaces were taken on the JEOL IT-500HR scanning electron microscope (SEM) at the NCFL. Particle analysis using an energy dispersive spectrometer (EDS) was used to confirm if particles on the fracture surface had the expected chemical makeup. As EDS analysis does not provide a highly accurate analysis of the phases present nor does it give the exact chemical makeup of the particles, it was only used to provide a qualitative determination.

3.9 Metallography

Microstructural analysis of the fracture surface was done on the epoxy-mounted samples. All samples were polished according to the steps listed in Appendix B. The 6061 AFSD and wrought material were etched with Keller's reagent to reveal the grain structure and flow. For the 7075 materials, the Keller's etch was unable to reveal the grain structure clearly, so Weck's reagent was used to color the grain boundaries. The chemical compositions and methods used for each etchant are listed in Appendix B [66].

3.10 Raman Spectroscopy

Imaging of the unetched samples of 7075 revealed that there were dark particles that were potentially from the graphite lubricant used. Raman spectroscopy with a 532 nm laser was used to determine if the material was carbon and whether the phase was amorphous or graphitic. Raman spectroscopy utilizes inelastic scattering to determine the phase of the carbon in both polymers and metals [67], [68]. The unetched samples were imaged with the Keyence microscope before the dark particles were investigated with Raman spectroscopy. The Raman phase shift from these particles was compared to phase shifts generated from the graphite lubricant used in production. The Raman phase shift of the graphite lubricant was measured from the lubricant after it was first sprayed and then after it was heat treated at 435 ^{o}C (818 ^{o}F) for approximately 30 minutes. The heat treatment temperature was determined from the build temperature of the 7075 AFSD builds. This was done for a representative sample of the heat treated material that achieved moderate elongation and an outlier sample.

Chapter 4 Results 6061

4.1 Mechanical 6061

Table 4.1 lists the results from this thesis for both the as-deposited and heat treated conditions as well as the wrought material heat treated alongside the AFSD material. For comparison, the standard values for annealed and T1 and heat treated conditions for a wrought aluminum bar are listed in Table 4.1 [60]–[62]. According to the standard, unless noted, the values listed are the minimum values required to meet the standard. Table 4.2 quality lists the average, maximum, and standard deviation of the mechanical properties of the 6061 as-deposited (AD) and heat treated (T6) conditions.

Table 4.1 Selected mechanical properties of 6061 aluminum [60]–[62].

Name	R_Y (MPa)	R_{UTS} (MPa)	El (%)
Wrought 6061-O [60]	110 (max)	152 (max)	16
Wrought 6061-T1 Bar [62]	97	179	16
Forging (≤ 4") 6061-T6 [61]			
Trans (Z)	241	262	8
Long (X)	241	262	10
Bar (≥ 0.250") 6061-T6 [62]	241	262	10
AFSD 6061-AD			
Z	61 ± 2	128 ± 0.5	30 ± 3
X	66 ± 5	147 ± 1	35 ± 2
AFSD 6061-T6			
Z	313 ± 5	337 ± 8	5 ± 3
X	288 ± 15	323 ± 15	13 ± 1
Wrought 6061-T6	411 ± 5	431 ± 8	15 ± 2

Table 4.2 The average mechanical results of the material and the calculated quality index values.

	AFSD Z 6061-AD	AFSD X 6061-AD	Wrought 6061-O	AFSD Z 6061-T6	AFSD X 6061-T6	Wrought 6061-T6
#Samples	4	6	2	10	3	8
E(GPa)						
max	58	69	70	72	71	73
mean	53 ± 3	65 ± 3	70 ± 0	69 ± 1	68 ± 5	71 ± 1
R_Y(MPa)						
max	64	74	106	321	310	417
mean	61 ± 2	66 ± 5	106 ± 0	313 ± 4	288 ± 15	411 ± 5
R_{UTS}(MPa)						
max	129	149	180	350	341	441
mean	128 ± 0	147 ± 1	162 ± 18	337 ± 8	323 ± 15	431 ± 8
A_{at} (%)						
max	14	34	16	4	12	8
mean	13 ± 1	22 ± 6	14 ± 2	2 ± 1	8 ± 3	7 ± 1
A_{after} (%)						
max	33	38	18	11	14	18
mean	30 ± 3	35 ± 2	18 ± 0	5 ± 3	13 ± 1	15 ± 2
W(MJ/m^3)						
max	583	1168	1307	137	150	288
mean	527 ± 40	1098 ± 41	1307 ± 0	107 ± 25	144 ± 7	261 ± 20
K_D						
max	2.00	1.97	2.00	2.00	2.00	1.99
mean	1.86 ± 0.1	1.83 ± 0.1	2.00 ± 0.0	1.75 ± 0.2	1.89 ± 0.1	1.89 ± 0.1
Q_O						
max	5893	11756	13172	1695	1807	3292
mean	5328 ± 404	11045 ± 413	13171 ± 0	1382 ± 255	1729 ± 83	3023 ± 197
Q_D						
max	11785	23102	26343	3383	3615	6544
mean	9931 ± 1325	20240 ± 1339	26299 ± 45	2469 ± 687	3280 ± 307	5735 ± 586

4.1.1 As-Deposited

In both the X and Z directions, the general trend of the mechanical values for the as-deposited condition was that the material had low strength and high ductility. The as-deposited material met the standard criteria for annealed aluminum as it did not exceed the maximum values for ultimate tensile strength or yield strength. The calculated quality index, Q_D, showed

that the wrought material ranks the highest followed by the AFSD X direction and then AFSD Z direction. The AFSD X direction ranked over 50% higher than the AFSD Z direction samples. In terms of strength values, only the yield strength was not directionally dependent, but the ultimate strength value was dependent on sampling direction. For the elongation values, the elongations at fracture are dependent on testing direction but measured elongation after fracture were not. Table 4.3 lists the results of the t-test done with the mean, variance, and P-value listed.

Table 4.3 T-test results of the Z and X directions in the as-deposited conditions.

R_Y (MPa) AFSD As-Deposited			**R_{UTS} (MPa) AFSD As-Deposited**		
	Z	*X*		*Z*	*X*
Mean	61	66	Mean	128	147
Variance	7	28	Variance	0.3	1
t-Stat	-1.9		t-Stat	-33.0	
P-value	0.10		P-value	6.01E-9	
A_{at} (%) AFSD As-Deposited			**A_{after} (%) AFSD As-Deposited**		
	Z	*X*		*Z*	*X*
Mean	13	22	Mean	*30*	35
Variance	1	37	Variance	16	5
t-Stat	-3.3		t-Stat	-2.1	
P-value	0.02		P-value	0.13	

4.1.2 Heat Treated

After the heat treatment, the AFSD material had a significant increase in yield and ultimate strength with a significant decrease in elongation. The wrought bar met the standard strength and elongations values for wrought material of similar chemistry and dimensions. In both directions, the AFSD material exceeded the strength minimums required for a forging. Both directions had similar increases in yield strength (~ 80%) and ultimate tensile strength (~60%) after heat treatment. This percent change is like the change in strength when a sample of wrought material was annealed and then heat treated to the T6 condition.

The Z direction samples did maintain ductility like the wrought material and did meet the standard for a forging sampled in the longitudinal (X) direction. The Z direction specimens did not meet the elongation values for a forging sampled in the transverse (Z) direction. The wrought material experienced a small change in ductility (~20%) whereas the AFSD in the X direction had a decreased in elongation by 165%. The Z direction decreased in elongation that was 3 times greater than the X direction. Due to the severe reduction of the elongation in the AFSD material, the wrought material ranked higher than both AFSD directions with the X direction ranking higher than the Z direction. A t-test on the X and Z direction was used to determine if the material was directionally dependent after the heat treatment. Table 4.4 lists the mean, variance, t-Stat, and p-value for the strength and elongation values which shows that after heat treatment only the elongation after fracture is statistically significant directionally dependent. However, both the yield strength and the elongation at fracture both have p-values of 0.1 which is very close to the p-value needed for a 90% confidence interval. Further investigation needs to be made to increase the number of samples tested in both directions to confirm that these values are not statistically significant.

Table 4.4 T-test results of the Z and X directions in the heat treated condition.

R_Y (MPa) Heat Treated			**R_{UTS} (MPa) Heat Treated**		
	Z	*X*		*Z*	*X*
Mean	313	288	Mean	337	323
Variance	22	353	Variance	79	330
t-Stat	2.3		t-Stat	1.3	
P-value	0.1		P-value	0.3	
A_{at} (%) Heat Treated			**A_{after} (%) Heat Treated**		
	Z	*X*		*Z*	*X*
Mean	2	8	Mean	5	13
Variance	1	14	Variance	9	3
t-Stat	-2.7		t-Stat	-6.0	
P-value	0.1		P-value	9.5E-4	

4.1.3 Elastic Modulus

The elastic modulus was determined from the linear region of the stress versus strain graph. For the as-deposited material, there were fewer data in the linear elastic region due to the lower stress required to reach the yield point. This is a potential source of the % difference from the literature values. Further tests need to be completed to confirm this value and potential directionality to the Young's modulus using another method such as resonance analysis or strain gauges attached to the specimen. The average Young's moduli are listed in Table 4.5 as well as the % difference compared to that of the ASTM standard for 6061 [60]. Both the X and Z direction in the as-deposited condition had lower elastic moduli than the literature value.

Table 4.5 The Youngs Moduli of the samples with percent error off the literature value.

Sample Name	Youngs (GPa)	% Difference
AFSD Z 6061-AD	53.5 ± 3.3	-22.4
AFSD X 6061-AD	65.1 ± 2.8	-5.5
Wrought 6061-O	69.8 ± 0.2	+1.3
AFSD Z 6061-T6	69.5 ± 1.5	+0.9
AFSD X 6061-T6	67.6 ± 4.5	-1.9
Wrought 6061-T6	70.9 ± 1.1	+2.9
ASTM 6061 [69]	68.9	

4.2 Fractography

4.2.1 Wrought 6061-T6

For comparison to the AFSD material, the wrought 6061-T6 fracture surface was used as a baseline. Visually and with an optical microscope, necking or reduction of surface area and a fibrous fracture appearance with a shear lip around the outer rim of the fracture surface were expected [57]. From the optical images of the wrought 6061-T6 fracture surface, we can see a shear lip and spongy ductile core, Figure 4.1.

This fibrous appearance is due to the formation of microvoids, which are voids that form around small inclusions in the aluminum [57]. Figure 4.2, shows a diagram of how microvoids are formed on the left with an image of the microvoids in an SEM [57]. As the force is applied beyond the yield point, the voids grow and combine, which eventually leads to fracture. The elongation of these voids are in the direction of the applied load. For a uniaxial tension test, the voids should appear round in shape. In the SEM, the wrought material had microvoids (or dimples) with elongation in the direction of applied load i.e., out of the page, Figure 4.3. The image was taken near the middle core of the fracture surface and shows a representative image of the microvoids that were found throughout the fracture surface. Finally, the metallographic analysis should reveal grain flow in the direction of the load and transgranular fracture on the

fracture surface [57]. Figure 4.4 shows that after polishing and etching of the fracture surface, the samples show grain flow that follows the direction of deformation.

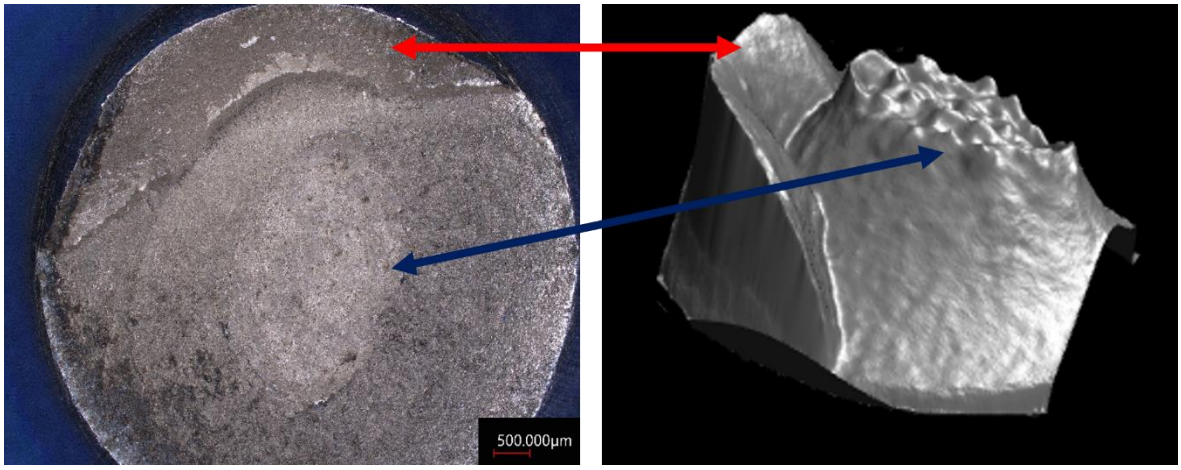

Figure 4.1 The optical image (left) at 5x magnification shows a dull fiberous appearance with the 3D rendering (right) shows the side profile of the shear lip (red arrow) and ductile fibrous center (blue) which indicates a ductile overlaod failure.

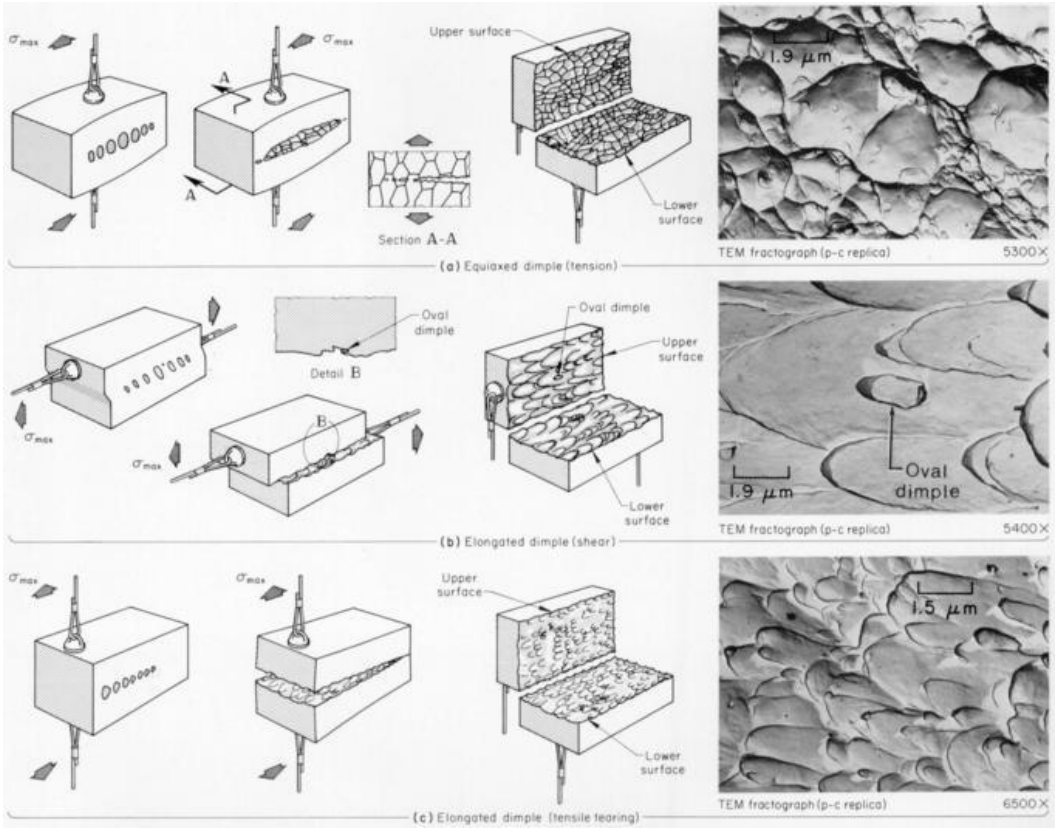

Figure 4.2 The diagram of the process by which microvoids form and their appearance under an SEM [57].

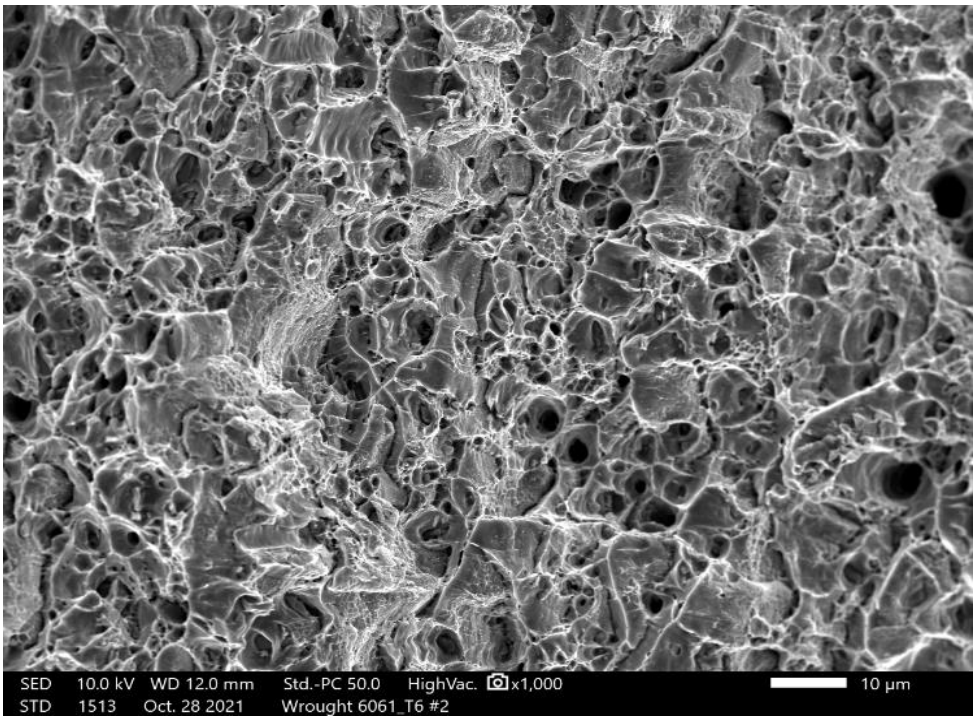

Figure 4.3 The center of the wrought 6061-T6 at 1000x showing microvoid coalsence indicative of ductile overload failure.

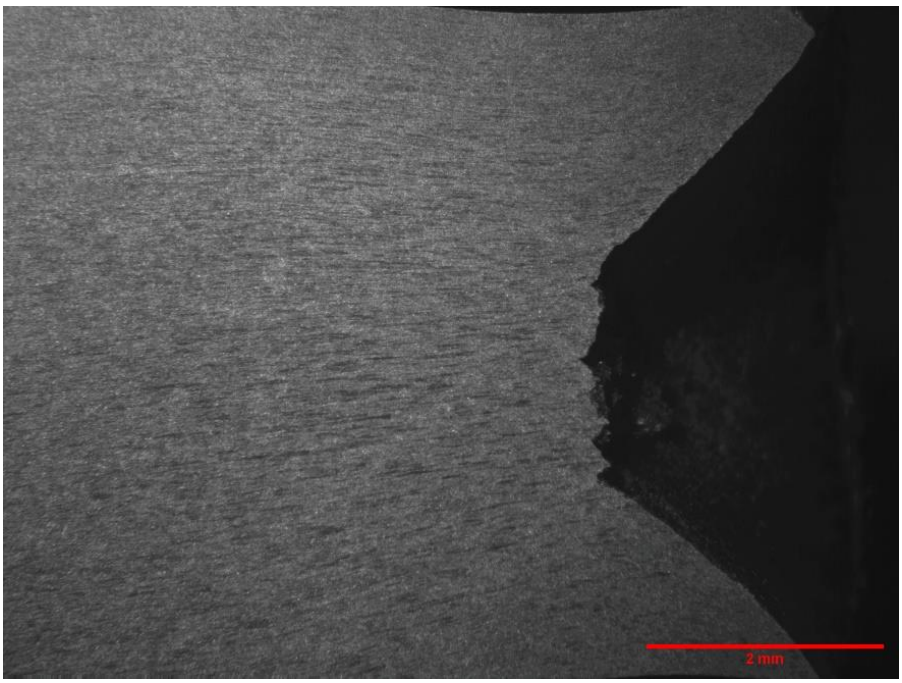

Figure 4.4 The cross section of the fracture surface at 10x with a Keller's etch reveals the grain flow of the material that follows the direction of deformation.

4.2.2 AFSD Z 6061-AD

As mentioned in the tensile results section, the as-deposited material in both the X and Z direction had low strength and high ductility. It was expected to exhibit indicators of ductile overload failure. Figure 4.5 shows the overview optical image of the fracture surface of a Z direction 6061-AD with the 3D rendering of the fracture surface on the right. This fracture surface visually had a large reduction in area and a shear lip around the edge. The SEM image of the fracture surface showed microvoid coalescence, Figure 4.6. The metallographic image in Figure 4.7, shows that there were flow lines along the build direction of the layers. Near the fracture surface, the grains distort in the direction of the deformation.

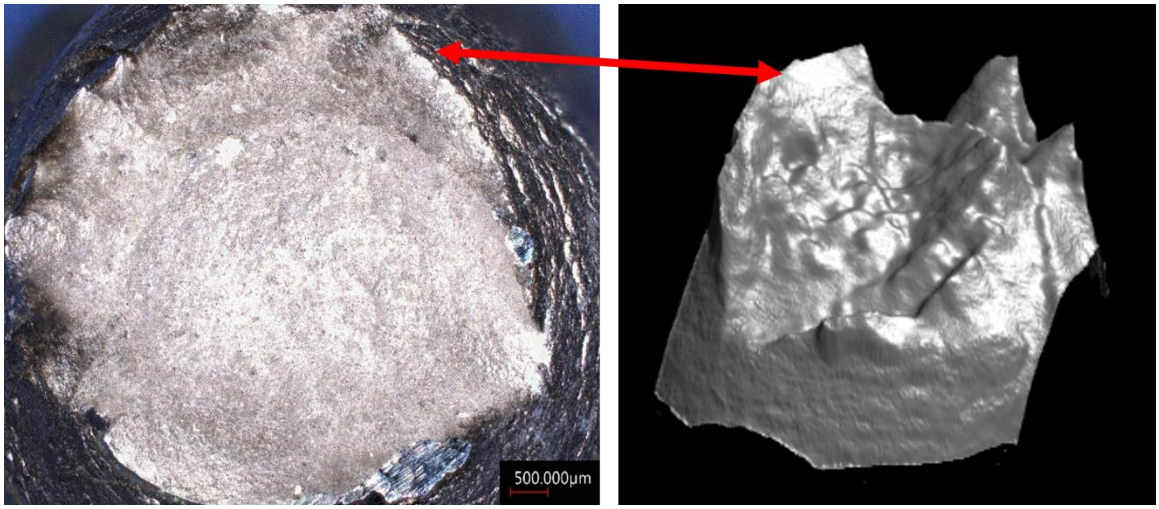

Figure 4.5 The fracture surface of the Z 6061-AD #15 sample had a shear lip (red arrow) and significant reduction in cross section.

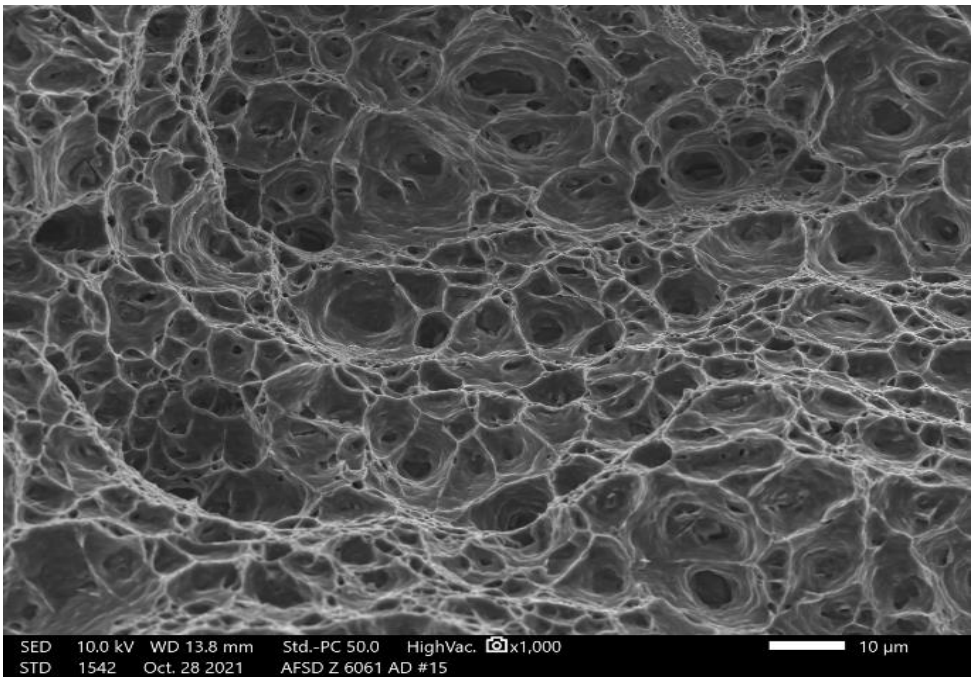

Figure 4.6 The center of the fracture surface of AFSD Z 6061-AD #15 in the secondary electron detection mode at and 1000x showing microvoid coalsence indicative of ductile failure.

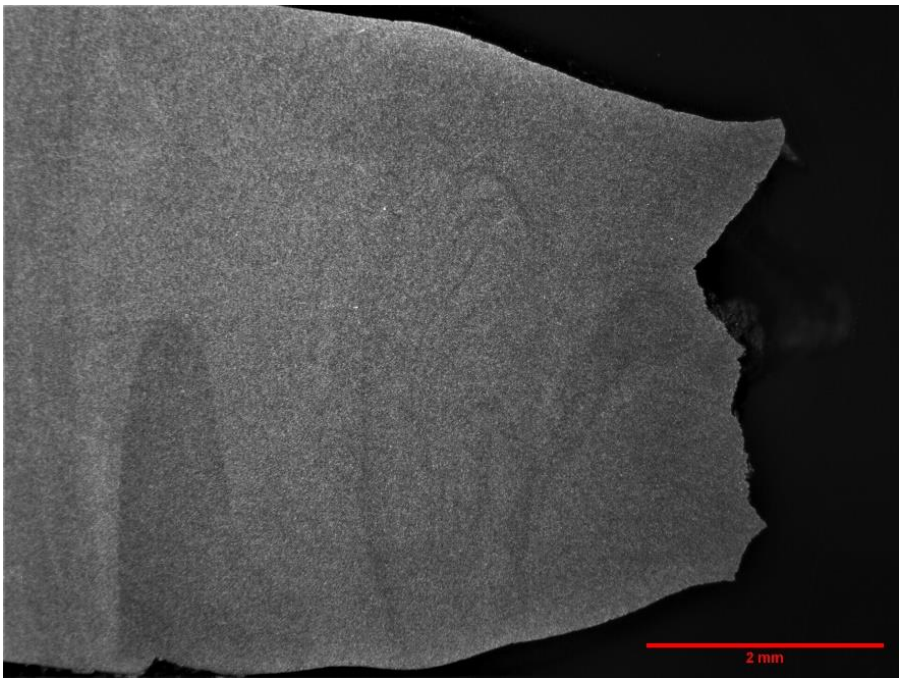

Figure 4.7 The cross section of the fracture surface of AFSD Z 6061-AD #15 at 10x showed the grain flow of the AFSD material that distorted around the reduced cross section where the sample was etched using Keller's reagent.

4.2.3 AFSD X 6061-AD

The X direction in the as-deposited condition had similar mechanical behavior as the Z direction however there were notable differences in the topography of the fracture surface and with the SEM analysis. The fracture surface of this material did not have an obvious shear lip instead the fracture surface formed spiked ridges on the edge of the fracture and across the surface. This was not the typical cup and cone fracture as seen in the wrought material and in the Z direction as-deposited material. Figure 4.8 shows the fracture surface with the 3D rendering of the topography of the fracture surface. The microstructure of the X direction samples, Figure 4.9, shows that the material has a layered structure with flow lines in the direction of the build. As the fracture surface reduced in area, the flow lines followed the distortion.

In the SEM, the fracture surface showed microvoid coalescence, however, it should be noted that at the base and along the sides of the ridges the material had small hairline cracks. At higher magnification, some microvoids were elongated in the direction transverse to the applied tensile load within the cracks. Figure 4.10a, shows an overview SEM image of the fracture surface. Figure 4.10b and c had hairline fractures located on the ridges and at the bottom of the ridges. Inside the hairline fractures, Figure 4.10d, shows what is the side profile of microvoids which means that the peaks of the voids transverse to the applied load.

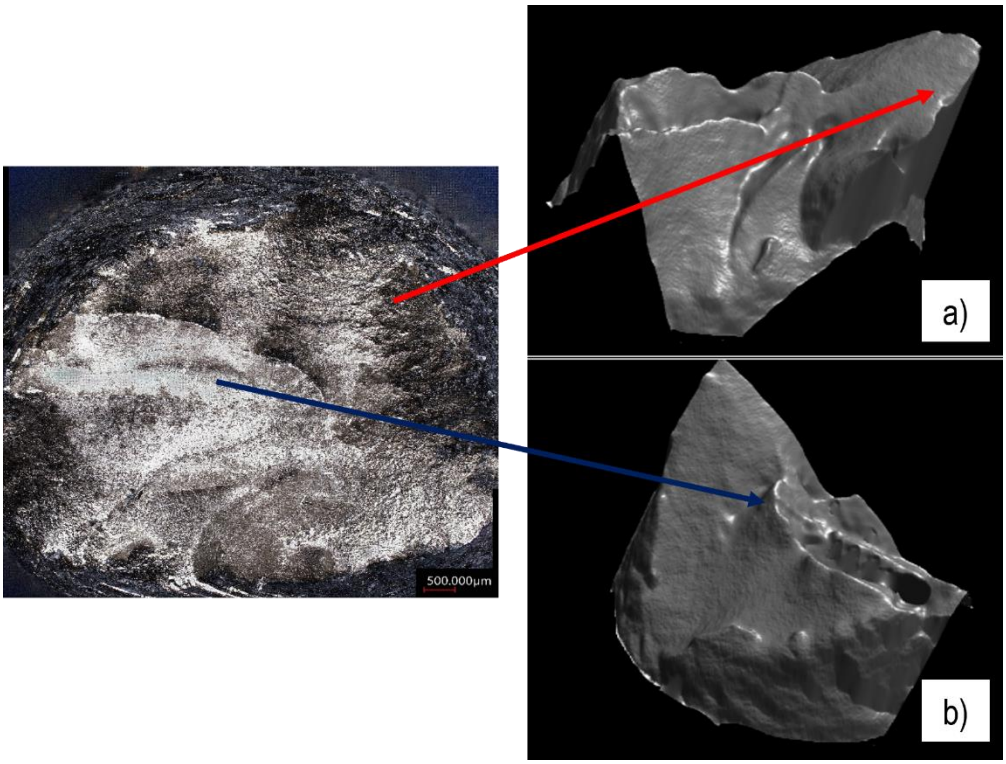

Figure 4.8 The fracture surface of the X 6061-AD #2-1 has a large ridge (red arrow) and ridges throughout the surface (blue arrow). The 3D the topography of the fracture surface as viewed from the top (a) and bottom (b) side

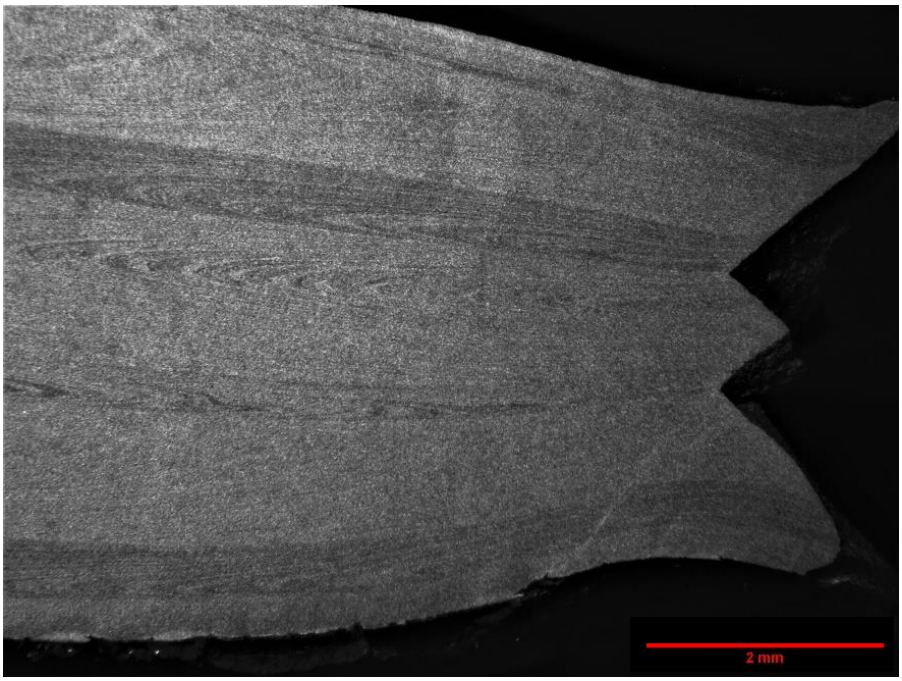

Figure 4.9 The grain flow in sample X 6061-AD #2-1 etched with Keller's revealed that the grain flow distorted in the direction of the load.

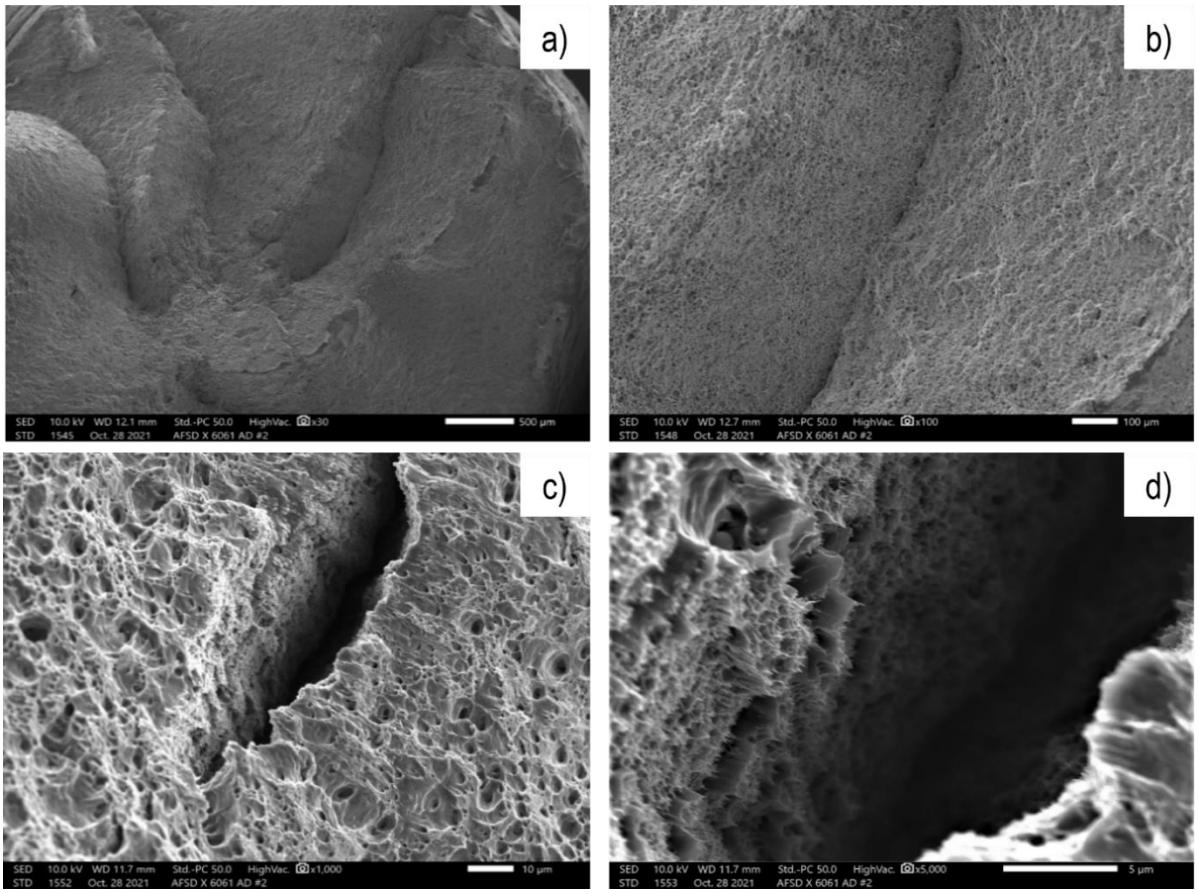

Figure 4.10 There were numerous secondary cracks at the base of the ridges (b and c). On the sides inside of one of these cracks (d), there were microvoids.

4.2.4 AFSD Z 6061-T6

Z direction material after heat treatment had a notable change in the fracture surface appearance. The fracture surface no longer had a cup and cone appearance but had an angular shear fracture that had ledges along the shear direction. Figure 4.11 shows an overview of the fracture surface and the topography of part of the fracture.

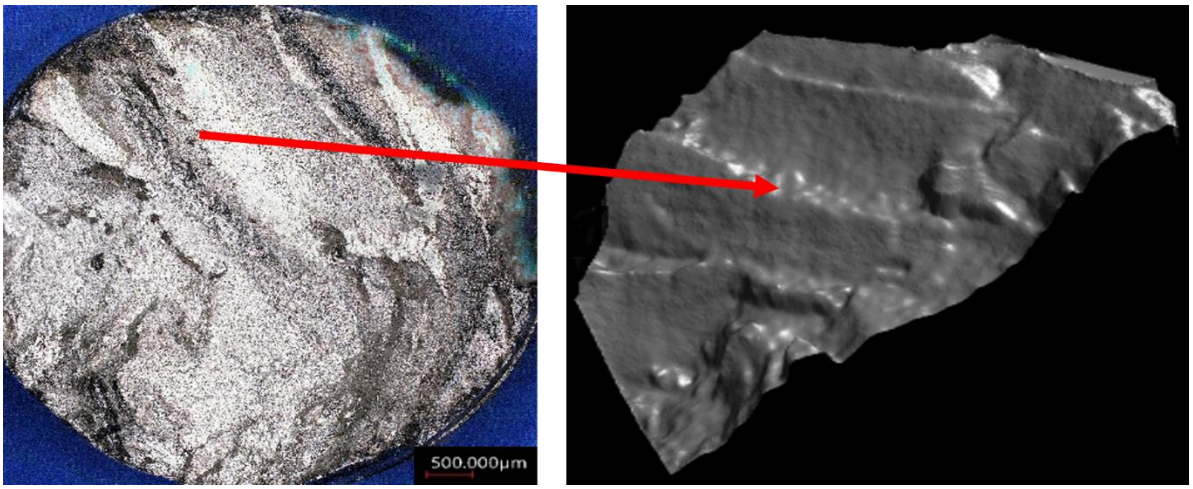

Figure 4.11 The fracture surface of the X 6061-T6 #9 (left) and the 3D rendering of the surface (right) showing steps on the surface.

In the SEM, the microvoid appearance was different depending upon the location on the ledges. Figure 4.12 uses the topography 3D rendering to show the appearance of the fracture surface at different locations. Figure 4.12 points out that the appearance of the microvoids changes with the location on the steps from deep microvoids to microvoids that were shallow and smooth in appearance, Figure 4.12a. On the angled plane or riser of the steps, the microvoids appear normal in appearance and are slightly elongated in the direction of the applied load, Figure 4.12b. The tread of the stepped fracture surface had a smoother appearance with very shallow microvoids, Figure 4.12c.

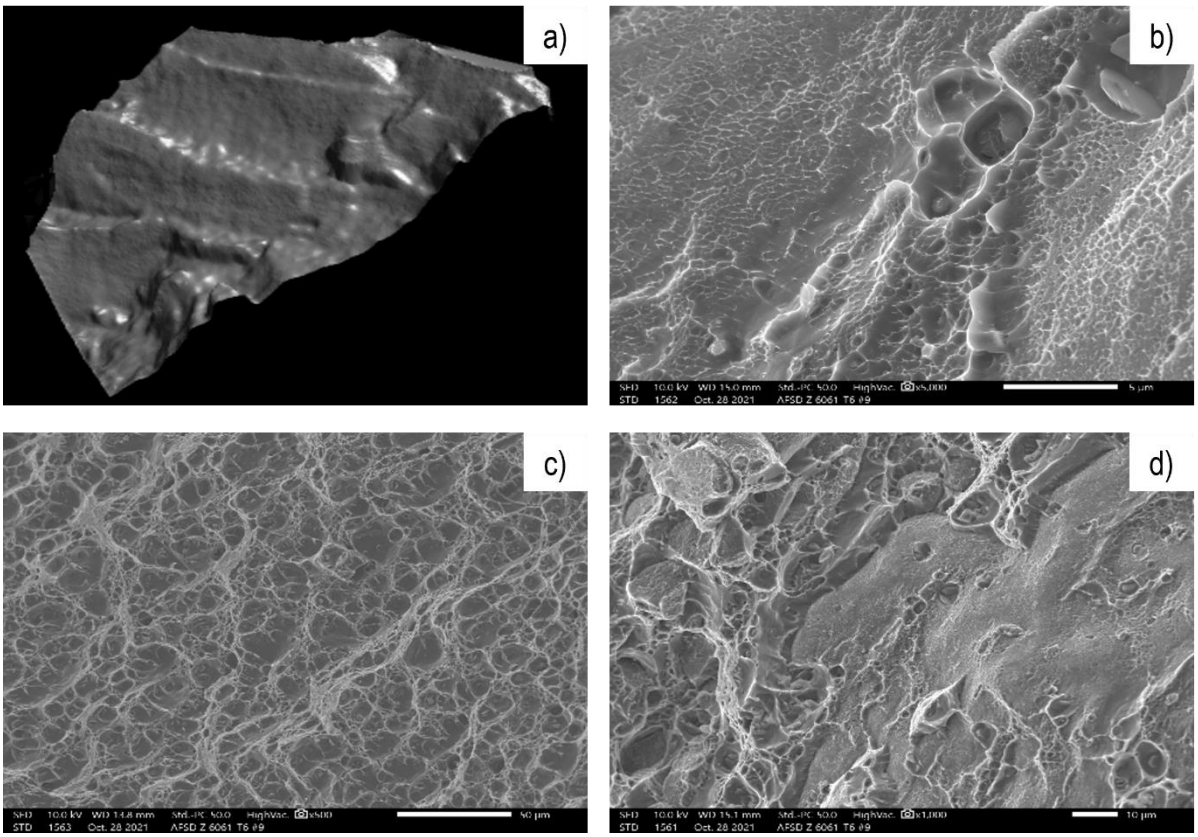

Figure 4.12 The difference in microvoid appearance of the step at the tread (b) the riser (c) and at the interface between the tread and riser (d).

In addition to this fracture surface, on other fracture surfaces, it was found that at the interface between the step and the angled ledge there were secondary cracks that followed the direction of the layers. Figure 4.13a, shows how the tread of the step had a secondary crack that runs transverse to the applied load and in the direction of the layers. On this ledge and in the internal hairline crack, Figure 4.13c, and 4.13d, the surface is smooth with very shallow microvoids that are elongated in the direction of the applied load. Figure 4.14 shows that after etching the grains had grown in the direction of the layers.

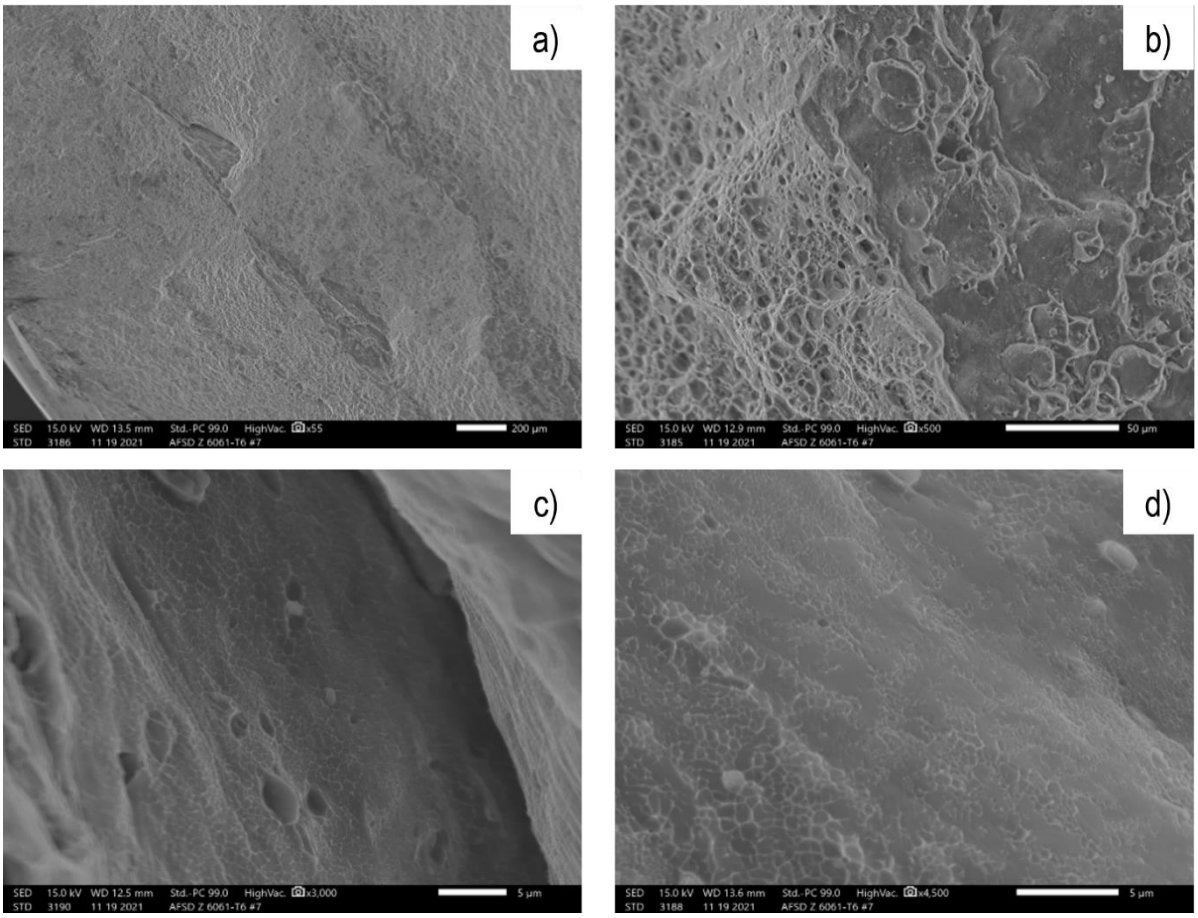

Figure 4.13 At the flat section of the ledge (a) the appearance is smooth with shallow microvoids (b). The crack that runs parallel to the fracture surface (c and d) is deep with shallow microvoids.

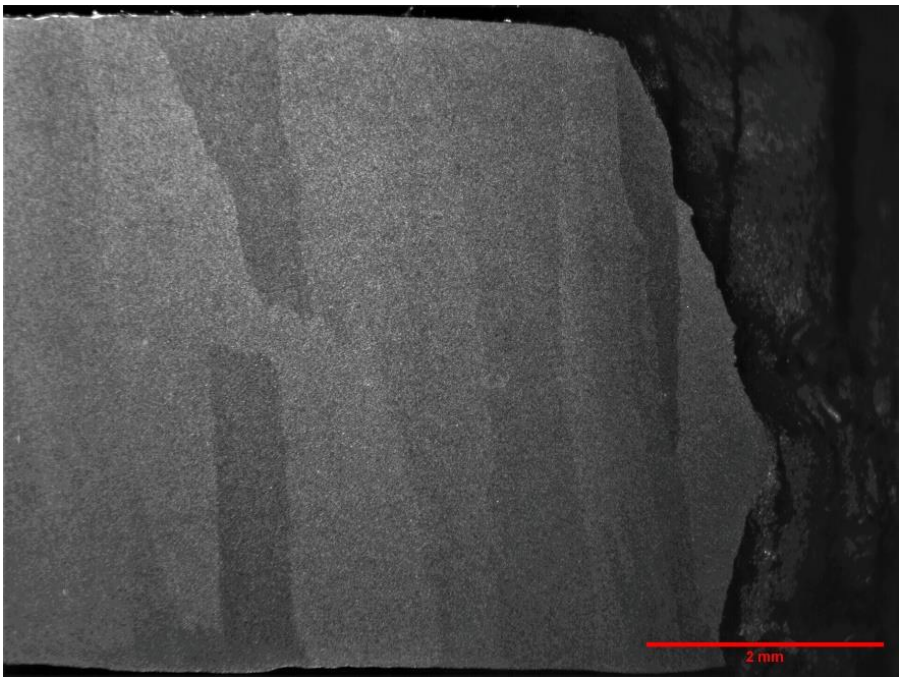

Figure 4.14 The Z 6061-T6 #9 sample after Keller's etch shows that after heat treatment the grains had grown in the direction of the layers.

4.2.5 AFSD X 6061-T6

The X direction samples also showed a change in fracture appearance after heat treatment. Upon visual examination of the fracture surface, the layer direction was apparent and pronounced. There were also cracks running parallel to one another across the fracture surface that were large enough to be seen visually. In addition to this, the topography of the fracture surface was more severe and difficult to image on the confocal microscope, Figure 4.15. In the SEM, the fracture surface appearance was like the Z fracture appearance. Figure 4.16 shows that near a secondary crack the surface near it had shallow microvoids that were smooth in appearance. At higher magnifications, the smooth surfaces have shallow microvoids as opposed to the deeper microvoids expected Figure 4.17. The metallography showed that upon etching, the grains were elongated and in the direction of the deposited layer. At one of the grains, we see that the material has fractured around a grain boundary, Figure 4.18.

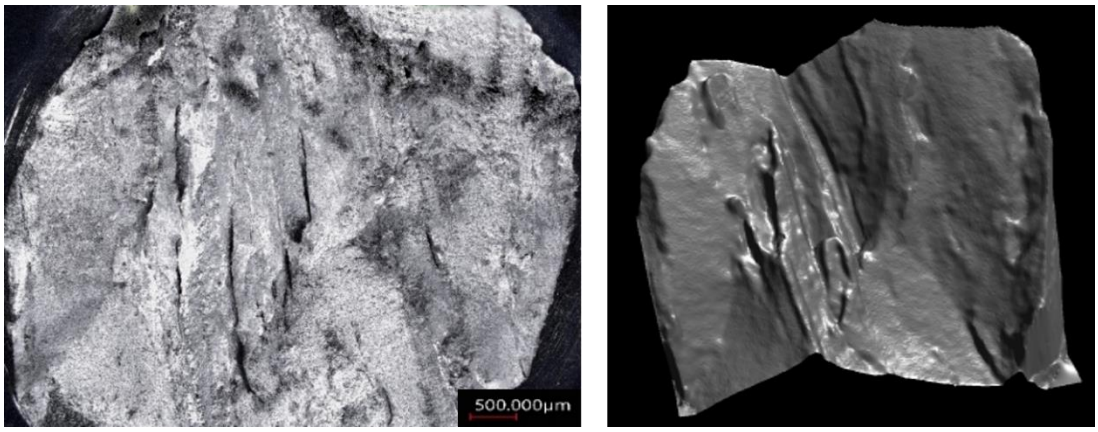

Figure 4.15 The figure shows that the dark lines are all parallel to etch other and run across the fracture surface.

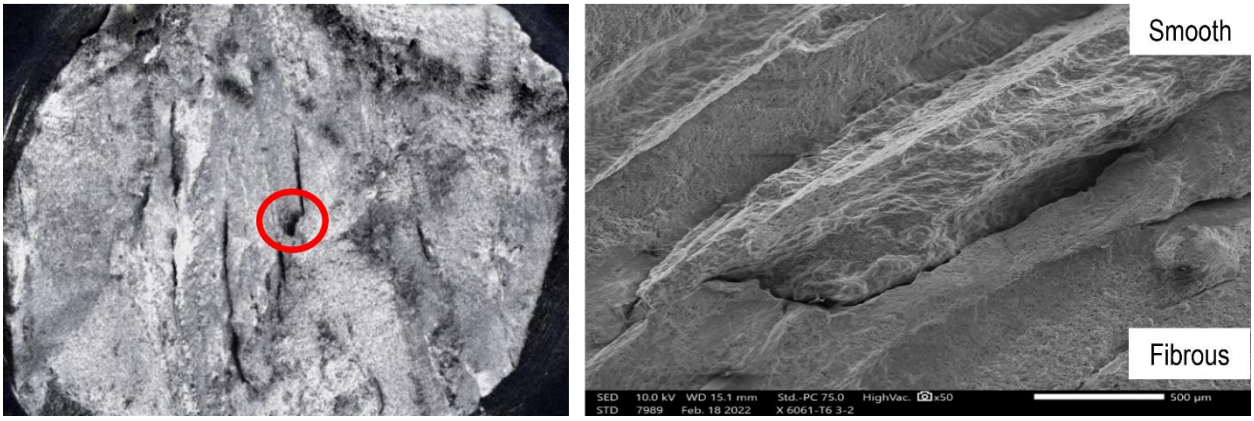

Figure 4.16 The appearance of the fracture surface changed from smooth to fibrous (right) near the secondary crack circled in red.

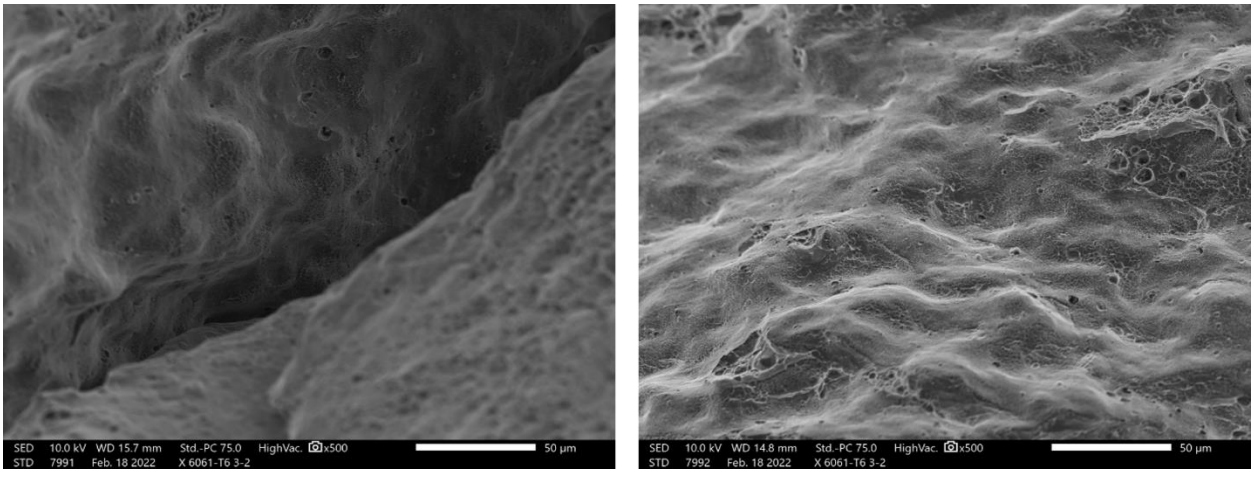

Figure 4.17 The cracks with a smooth appearance had shallow microvoids.

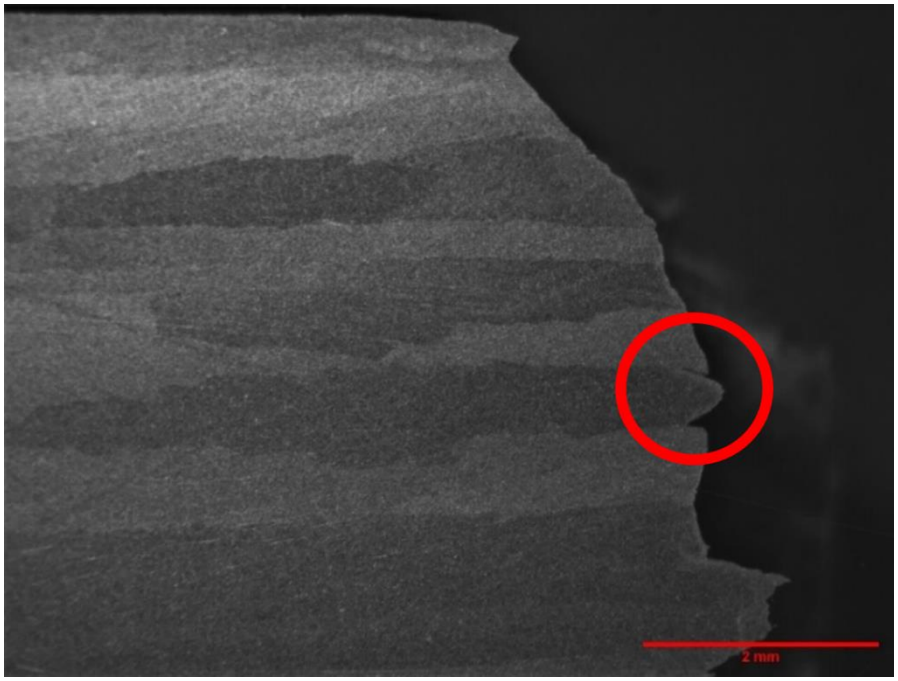

Figure 4.18 The grains grew after heat treatment in the direction of the layers and a crack initiated around a grain, circled in red.

4.2.6 Particle Analysis of 6061 As-Deposited and Heat Treated

There should be particles at the bottom of each microvoid. According to the chemistry of 6061 aluminum, it was expected to find Si and Mg rich particles on the fracture surface. EDS analysis of the wrought 6061-T6 fracture surface was used as a baseline to show that the particles were Mg and Si rich, Figure 4.19. These particles were expected in both the as-deposited condition and in the heat treated condition for the AFSD X and Z directions. Figure 4.20 shows the microvoids of the as-deposited material in the AFSD Z direction. The particles were Mg and Si rich with some Fe rich particles dispersed throughout.

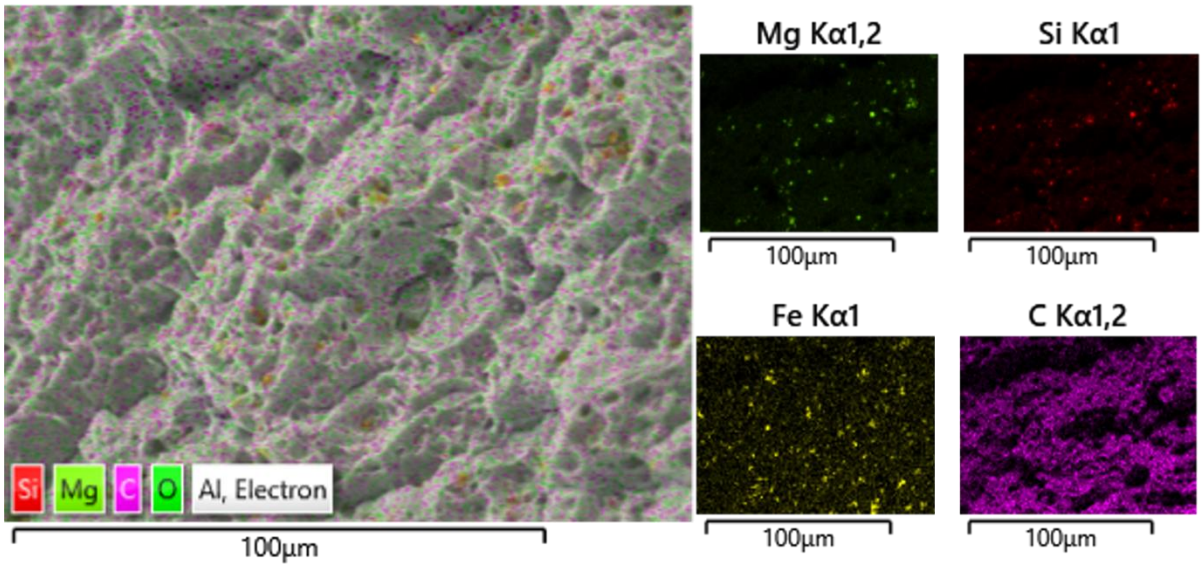

Figure 4.19 The heat treated fracture surface of wrought 6061-T6 #2 had Si and Mg rich particles in the bottom of the microvoids with Fe evenly dispersed.

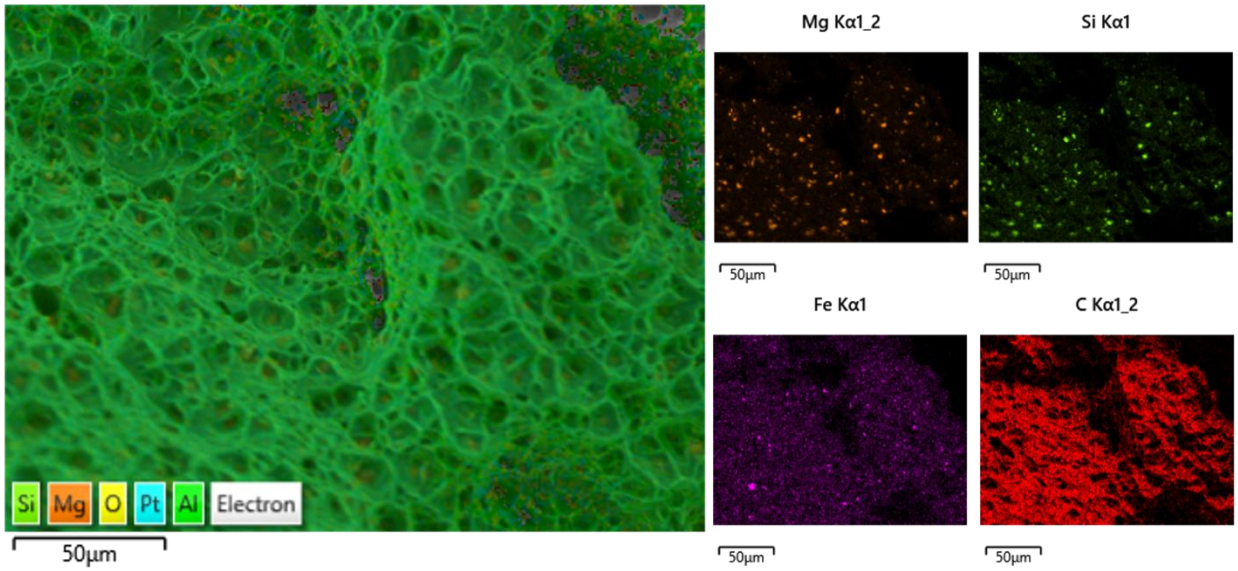

Figure 4.20 The as-deposited fracture surface had Si and Mg rich particles in the bottom of the microvoids sample AFSD Z 6061-AD #15.

After heat treatment as discussed in the previous sections, there were two distinct regions of the fracture surfaces in the AFSD Z direction samples; a ductile section with microvoids and a smooth section with shallow microvoids. EDS analysis on the ductile microvoids noted as the riser of the step on the fracture surface were analyzed, Figure 4.21. This showed the particles in

the voids were rich in Si and Mg with Fe rich particles evenly dispersed on the surface. The tread of the step on the fracture surface showed similar Si and Mg rich particles, Figure 4.22.

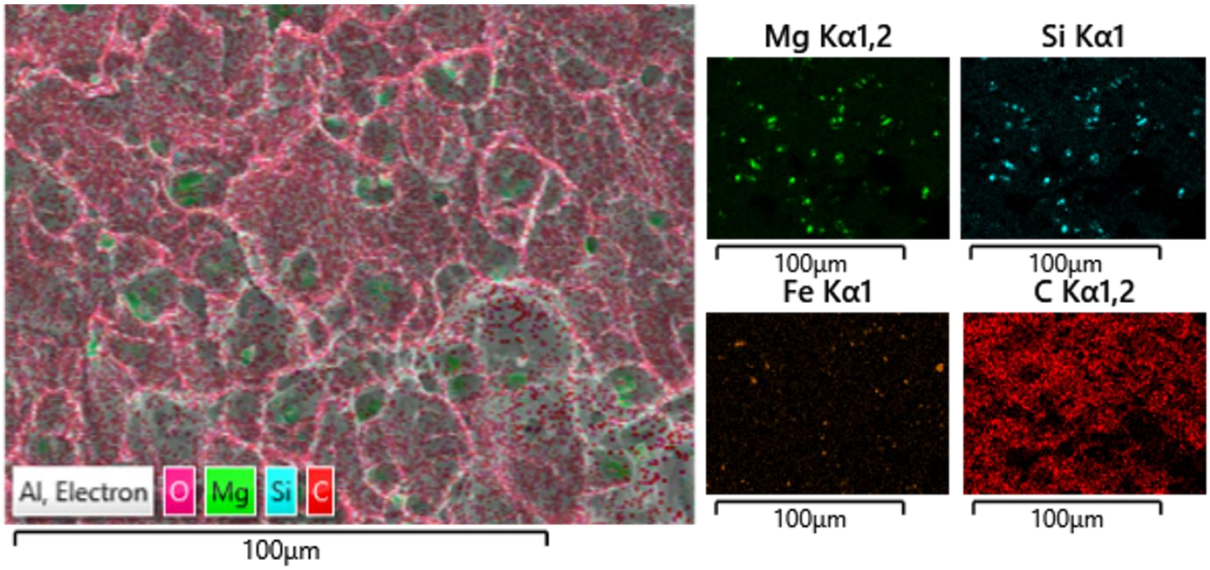

Figure 4.21 The heat treated fracture surface had Si and Mg rich particles in the bottom of the microvoids sample AFSD Z 6061-T6 #7.

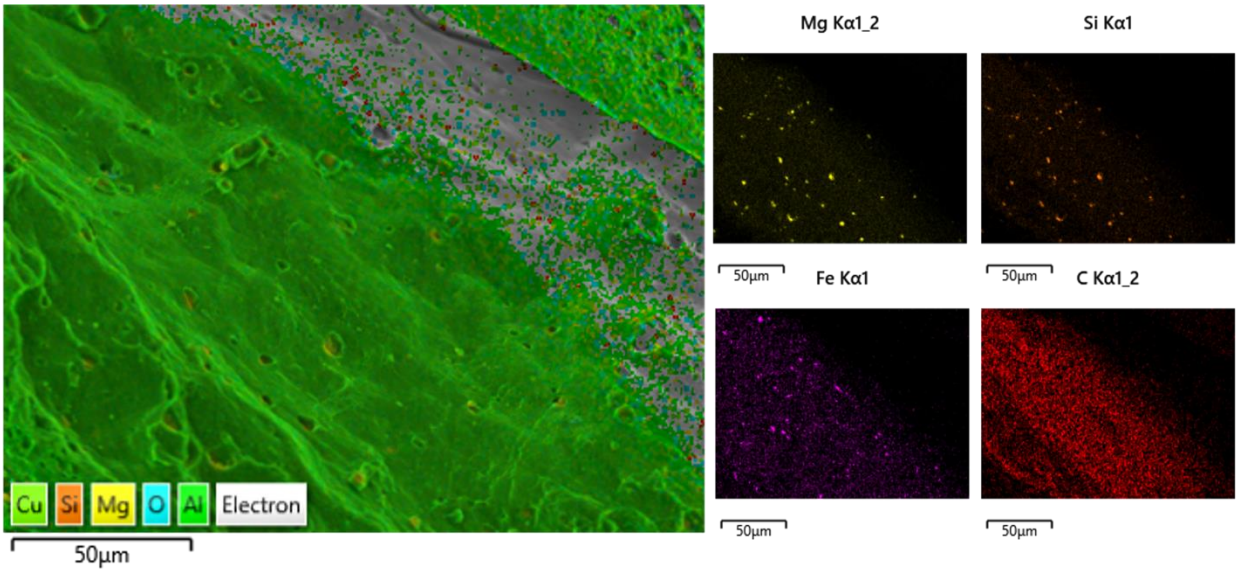

Figure 4.22 The heat treated fracture surface also had Si and Mg rich particles that were evenly dispersed on the smooth section of the fracture surface in sample AFSD Z 6061-T6 #7.

The fracture surface in the X direction after heat treatment also had two different appearances in the direction of the build layers. Figure 4.23 shows the microvoid section of the

sample that has Si and Mg rich particles. On the smoother shallow microvoid section, Figure 4.24, the particles were also rich in Si and Mg.

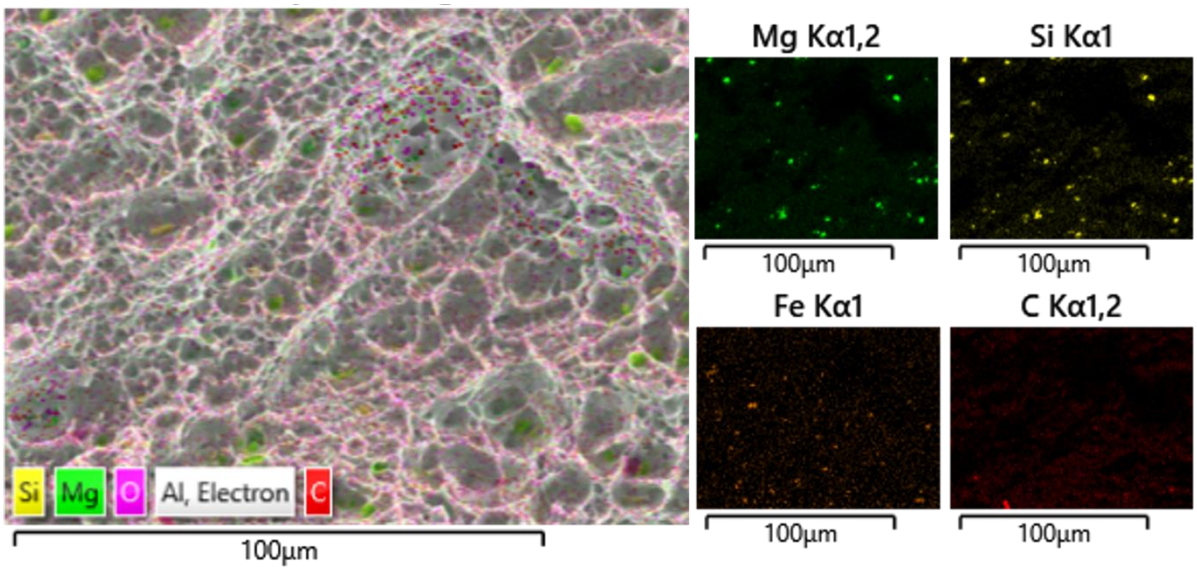

Figure 4.23 The heat treated fracture surface with microvoids had Si and Mg rich particles that were evenly dispersed on the facture surface in sample AFSD X 6061-T6 #1-2.

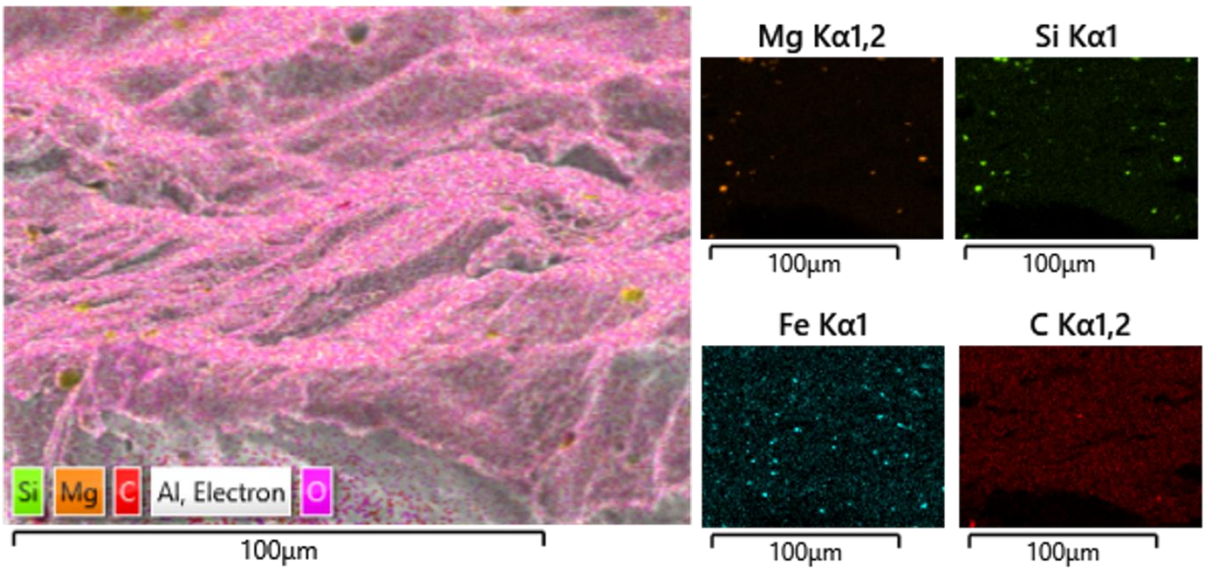

Figure 4.24 The heat treated fracture surface with the smooth and shallow microvoids had Si and Mg rich particles that were dispersed on the facture surface in sample AFSD X 6061-T6 #1-2.

4.3 6061 Outliers

4.3.1 AFSD Z 6061-AD #13

There were two outliers in the 6061 AFSD material, both from the Z direction samples. The first was sample Z 6061-AD #13. The yield strength of this material was within range of the other values, but it had a 15% lower ultimate strength than the average. The elongation both at and after fracture was over 70% lower than the average value for the as-deposited condition. The optical image of the fracture surface showed that the fracture did not have the expected cup and cone appearance. The fracture had a sheared section and then a twist in the center of the fracture. Figure 4.25 shows that the topography of the fracture surface was relatively flat with only the twist slightly raised. In an SEM, the surface appeared different at the sheared section and at the twist. In an SEM, the fracture appearance near the twist had microvoids, while the remaining section was smooth and granular in appearance, Figure 4.26. In the ductile region, Figure 4.27, the Mg and Si rich particles were found in the microvoids as expected. Figure 4.28 had the results from the EDS analysis from the section of the fracture surface that was smooth and granular in appearance. The results did not indicate any chemical contamination that caused the premature failure.

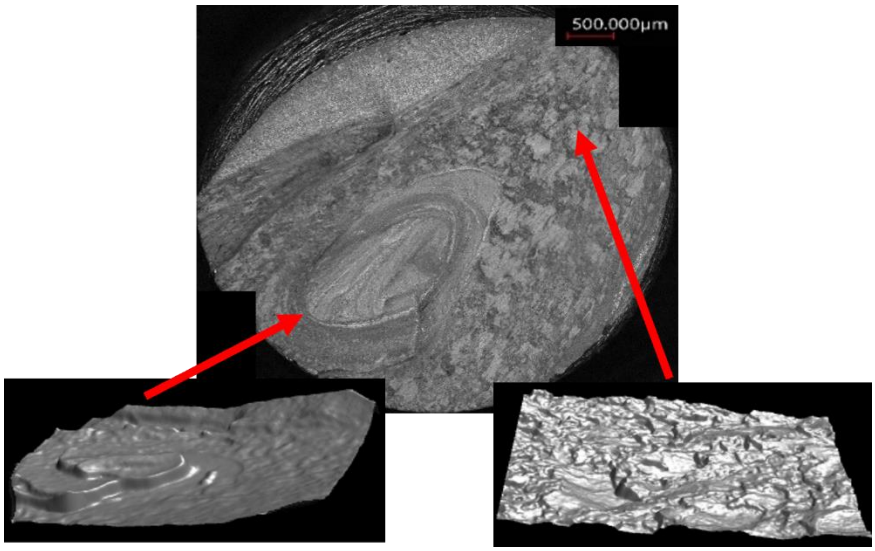

Figure 4.25 The fracture surface had two distinct zones the ductile ‘twist’ (left) and the granular appearance (right).

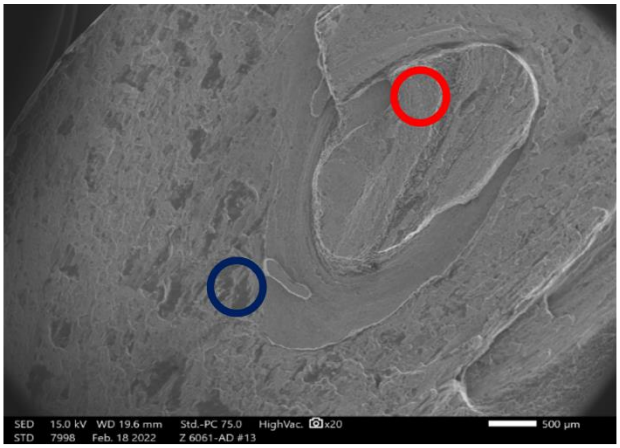

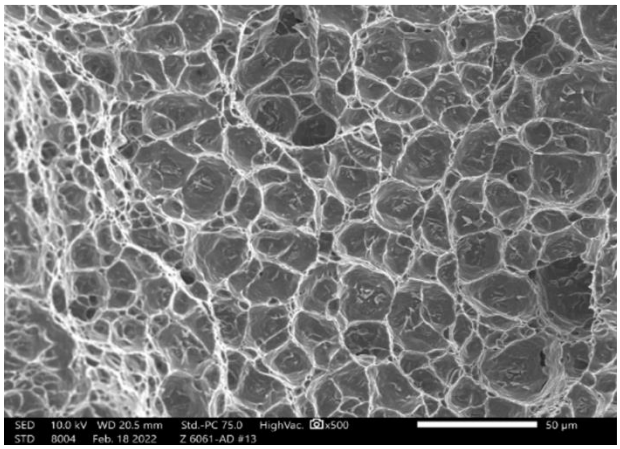

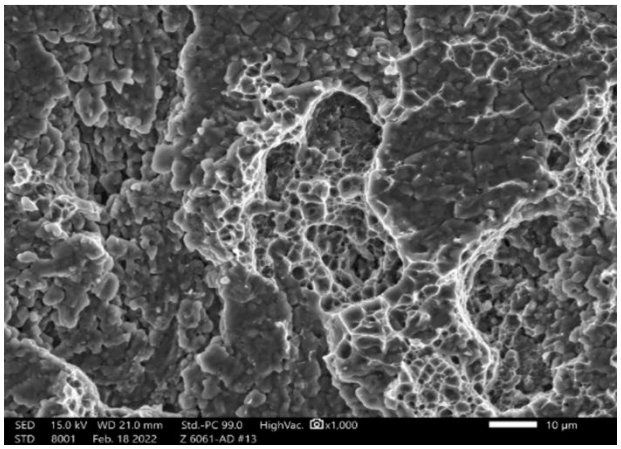

Figure 4.26 The fracture surface in the red circle was ductile in appearance (a) while the section in the blue circle was smooth in appearance (b).

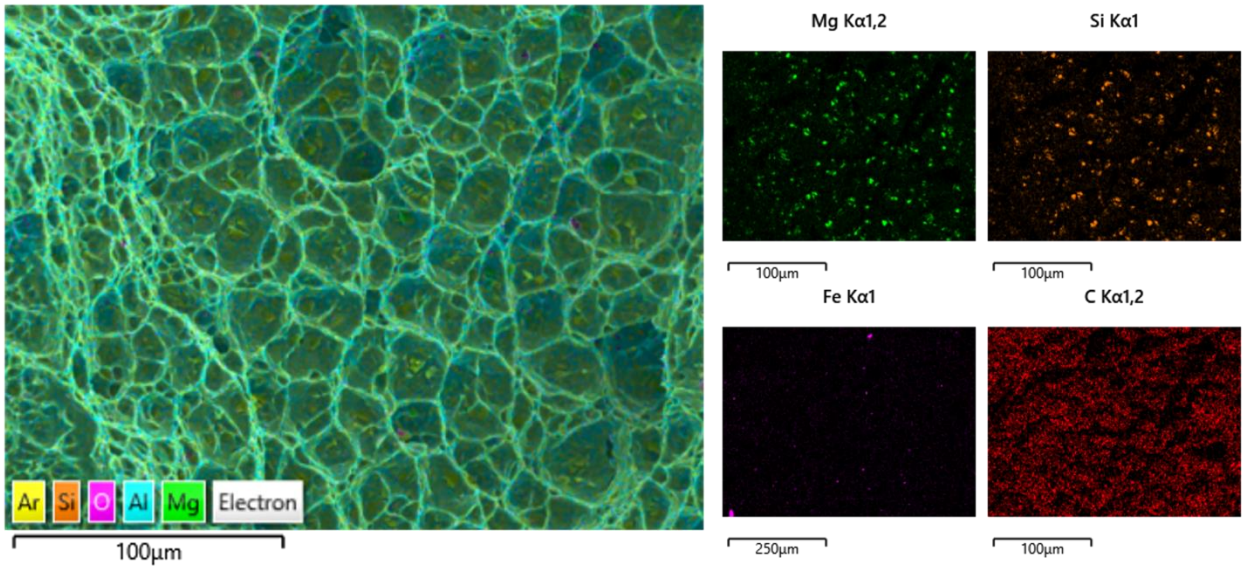

Figure 4.27 The EDS analysis of the ductile section of the 'twist' showed Mg and Si rich particles in the microvoids.

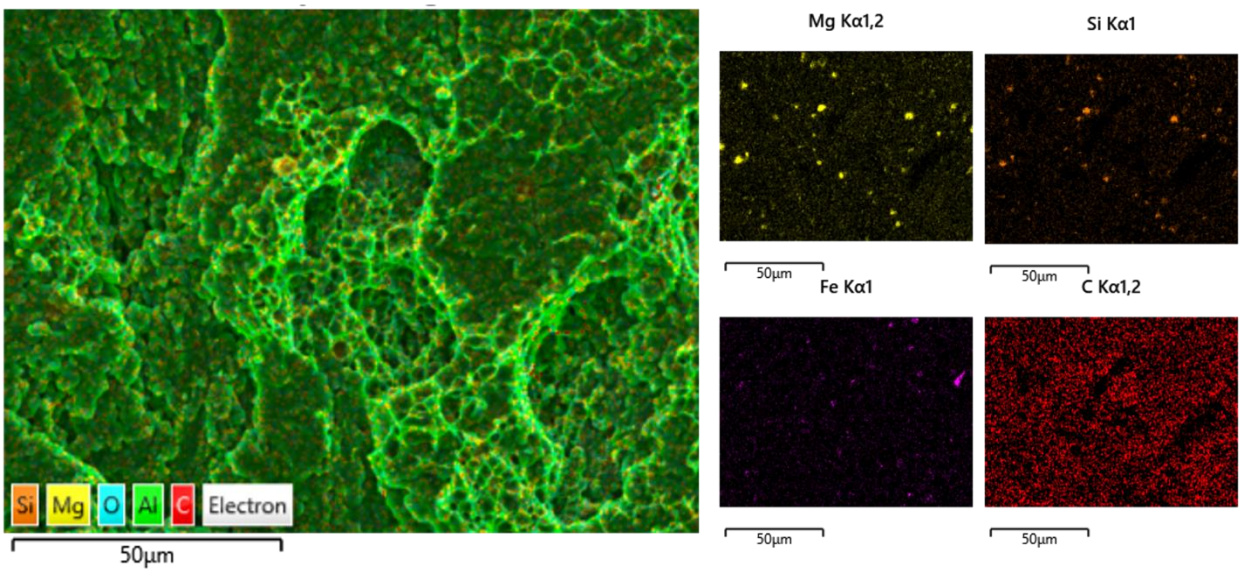

Figure 4.28 EDS analysis of the smooth and granular section showed Mg and Si rich particles that were not as evenly dispersed as the ductile 'twist' section.

4.3.2 AFSD Z 6061-T6 #5

The other outlier was also in the Z direction, but in the heat treated condition. The strength of this material was within the expected values when compared to the other samples, however, the elongation at and after fracture was much lower than average. The average value for elongation after fracture without the outlier included was 5% while the elongation of this material was only

1% elongation. The fracture surface of the samples in the Z direction had ledges or steps and this sample also has steps in them, but the topography was much flatter and there was a sharp corner on the fracture surface where the material had sheared off. Figure 4.29 shows the top view of the fracture surface and the sharp corner of the fracture surface where the material had sheared off.

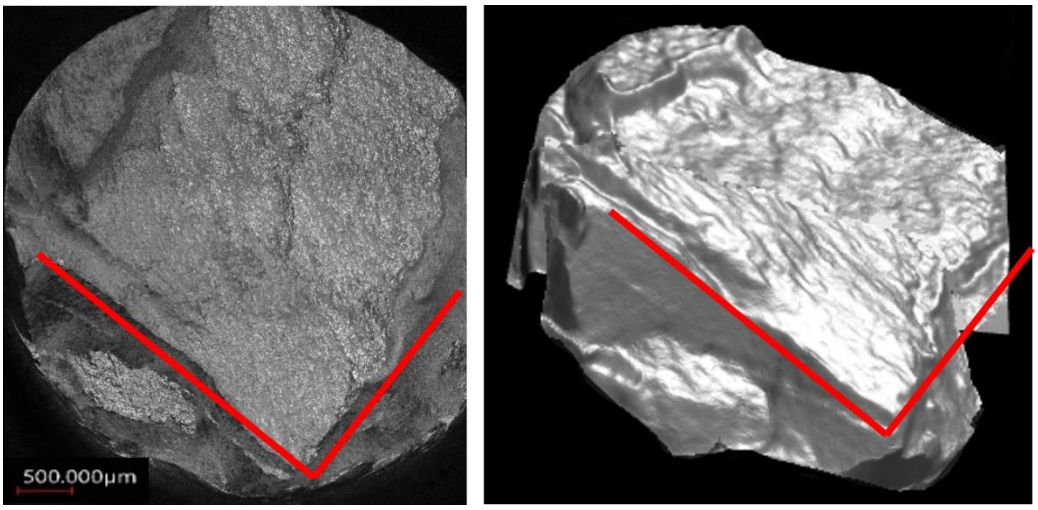

Figure 4.29 The fracture surface (left) and the topography (right) showed some ledges with a sharp corner outlined in red.

The SEM image in Figure 4.30, shows that on most of the fracture surface, the appearance was smooth with very shallow microvoids and only a few deep microvoids. EDS analysis, Figure 4.31, showed that in the few deeper microvoids the particles were Mg and Si rich. The etched fracture surface of the material, Figure 4.32, showed that there was no notable difference in the grain size from that of the 6061 materials in the heat treated condition.

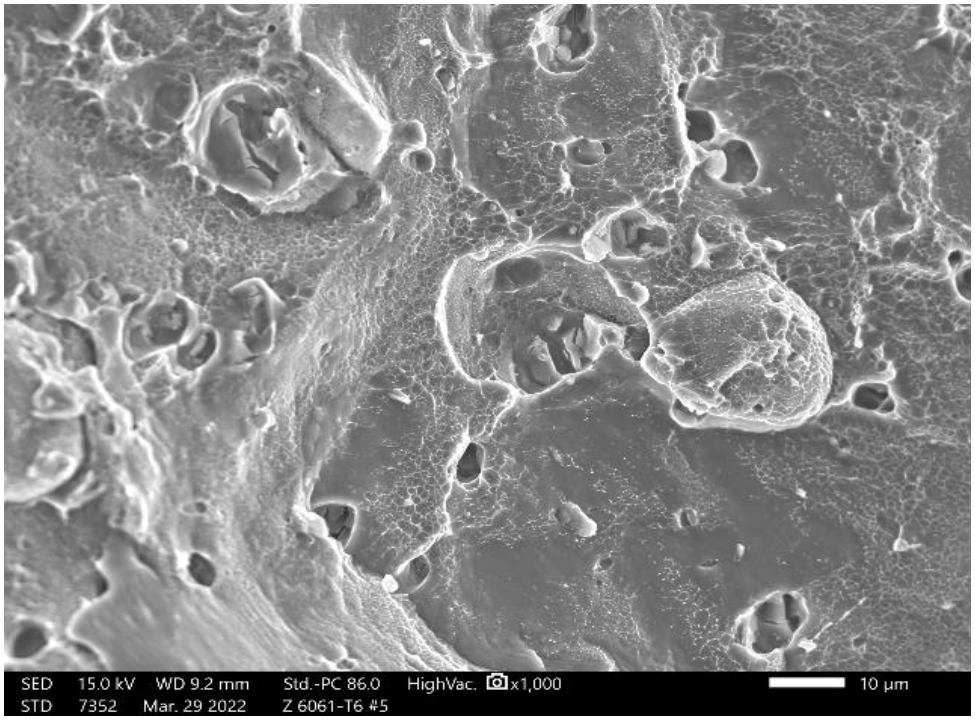

Figure 4.30 The fracture surface showed that most of the fracture surface was smooth in appearance with very shallow microvoids.

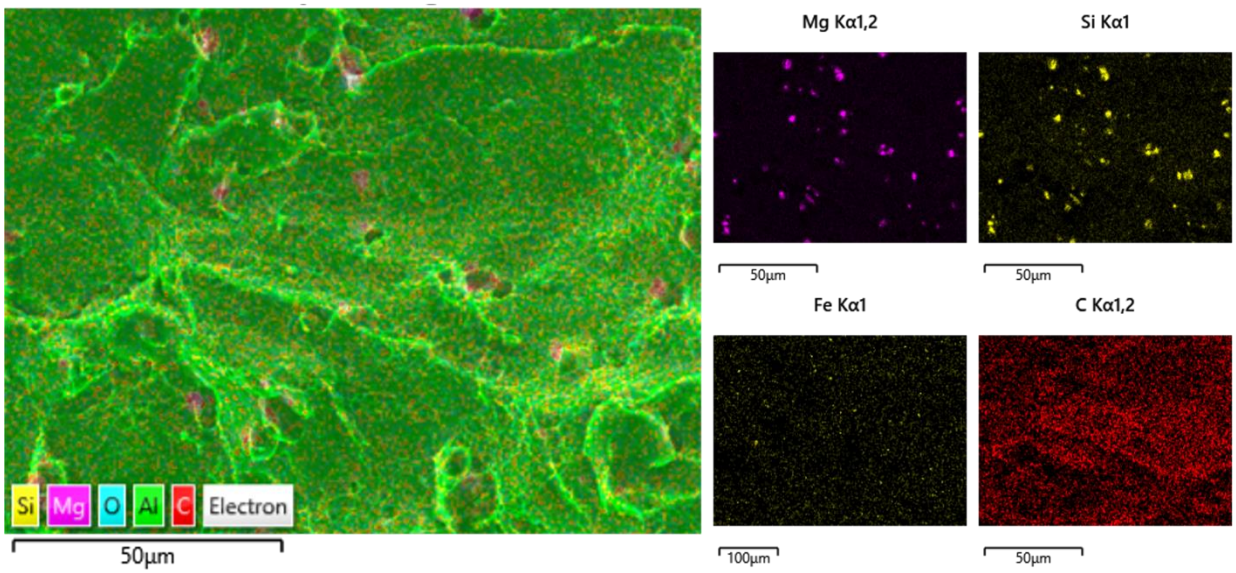

Figure 4.31 Although most microvoids were shallow, the particles in the deeper microvoids were Mg and Si rich.

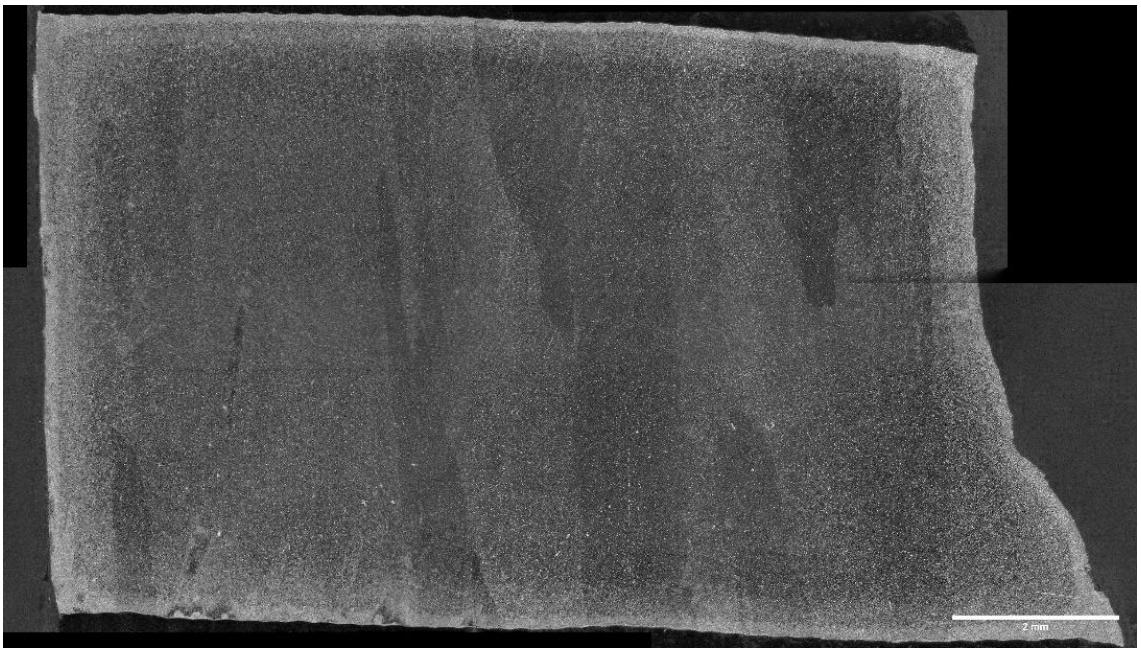

Figure 4.32 The grains grew after heat treatment in the direction of the layers with a crack initiating at a grain boundary.

Chapter 5 Results 7075

5.1 Mechanical 7075

For comparison, the literature values for annealed 7075 are listed in Table 5.1. Unlike 6061, 7075 standards do not list the T1 condition for any wrought or forged products [61], [62]. According to the standard unless noted the values listed are minimum values required to meet the standard. Table. 5.2 lists the average, maximum, and standard deviation of the mechanical properties and quality index values of the 7075 in the as-deposited and heat treated condition.

Table 5.1 Selected mechanical properties of 7075 aluminum [61], [62].

Sample Name	R_Y (MPa)	R_{UTS} (MPa)	El (%)
Wrought 7075-O Bar All [62]	165 (max)	276 (max)	10
Wrought 7075-T6 0.5" Bar [62]	496	558	7
Forged 7075-T6 up to 2" [61]			
Trans (Z)	421	503	4
Long (X)	434	510	9
AFSD Z 7075-AD	109 ± 5	225 ± 19	18 ± 6
AFSD Z 7075-T6	452 ± 184	518 ± 116	5 ± 3
AFSD Z 7075-T6 (outliers removed)	528 ± 4	573 ± 5	6 ± 2
Wrought 7075-T6	507 ± 6	566 ± 7	16 ± 1

Table 5.2 The Average mechanical properties and calculated quality index values for the 7075 AFSD and wrought material.

	AFSD Z 7075-AD	Wrought 7075-O	AFSD Z 7075-T6	Wrought 7075-T6
# Samples	9	2	7	7
E (GPa)				
max	72	68	69	69
mean	69 ± 3	66 ± 2	67 ± 1	67 ± 1
R_Y (MPa)				
max	116	158	532	513
mean	109 ± 5	156 ± 2	452 ± 184	507 ± 7
R_{UTS} (MPa)				
max	244	344	578	573
mean	225 ± 20	339 ± 6	518 ± 116	566 ± 7
A_{at} (%)				
max	26	16	7	10
mean	15 ± 7	15 ± 1	4 ± 3	9 ± 1
A_{after} (%)				
max	24	20	9	17
mean	18 ± 6	20 ± 0.2	5 ± 3	16 ± 1
W (MJ/m^3)				
max	1767	1424	450	518
mean	1156 ± 458	1365 ± 59	286 ± 127	472 ± 323
K_D				
max	2	2	2	2
mean	1.6 ± 0.3	1.9 ± 0.03	1.5 ± 0.6	1.9 ± 0.1
Q_O				
max	17781	14393	5024	5691
mean	11671 ± 4577	13808 ± 585	3307 ± 1425	5223 ± 229
Q_D				
max	35451	28468	9999	11377
mean	19855 ± 9839	26912 ± 1556	5730 ± 3017	9930 ± 686

5.1.1 As-Deposited

The general trend of the mechanical properties for the as-deposited condition was that the material was low strength and good ductility. The as-deposited material met the standard criteria for annealed aluminum as it did not exceed the maximum values for ultimate and yield strength.

The calculated quality index ranked the wrought material higher than the AFSD build. Because there was nothing to compare the directionality of the results, a t-test was used to compare the results to the wrought material. Table 5.3 lists the results of the comparison between the AFSD as-deposited material and the wrought 7075 material that was annealed. The t-test revealed that only the strength values were statistically significantly different.

Table 5.3 As-deposited AFSD material compared to wrought material in annealed condition.

R_Y (MPa) AFSD-Wrought			**R_{UTS} (MPa) AFSD-Wrought**		
	AFSD	*Wrought*		*AFSD*	*Wrought*
Mean	109	156	Mean	225	339
Variance	32	6	Variance	402	61
t-Stat	-18.3		t-Stat	-13.1	
P-value	5.2E-5		P-value	4.7E-05	
A_{at} (%) AFSD-Wrought			**A_{after} (%) AFSD-Wrought**		
	AFSD	*Wrought*		*AFSD*	*Wrought*
Mean	15	15	**Mean**	18	20
Variance	56	1	**Variance**	41	0
t-Stat	-0.1		**t-Stat**	-1.0	
P-value	0.85		**P-value**	0.35	

5.1.2 Heat Treated

After the T6 heat treatment, the AFSD material showed a significant increase in yield and ultimate strength with a predictable decrease in elongation. Both the wrought material and the AFSD material increased the yield and ultimate strengths in similar proportions. The AFSD material exceeded the minimum values required for strength and elongation for a forged material sampled in the transverse (Z) direction. Table 5.4 shows that, while the strength values were not statistically different, the elongation values both at and after fracture were different between the AFSD and wrought material. The standard deviation of the heat treated AFSD material was very

large due to several notable outliers. With these outliers removed, the strength and elongation values increased above that of the wrought material and had a lower standard deviation with less scatter in the data. Interestingly, with the removal of the outliers, the yield strength of the AFSD material was statistically greater than the wrought material. The same t-test used in Table 5.4 was repeated in Table 5.5 to show the change in the statistical difference with the outliers of the 7075 materials removed.

Table 5.4 T-test results for the AFSD and wrought material after heat treatment.

R_Y (MPa) AFSD-Wrought			**R_{UTS} (MPa) AFSD-Wrought**		
	AFSD	*Wrought*		*AFSD*	*Wrought*
Mean	452	507	**Mean**	518	566
Variance	39670	49	**Variance**	15686	59
t-Stat	-0.73		**t-Stat**	-1.01	
P-value	0.49		**P-value**	0.35	
A_{at} (%) AFSD-Wrought			**A_{after} (%) AFSD-Wrought**		
	AFSD	*Wrought*		*AFSD*	*Wrought*
Mean	4	9	**Mean**	6	16
Variance	9.8	0.6	**Variance**	10	2
t-Stat	-3.7		**t-Stat**	-7.6	
P-value	0.01		**P-value**	3.5E-5	

Table 5.5 T-test results for the AFSD and wrought material after heat treatment with the outliers removed.

R_Y (MPa) AFSD-Wrought			**R_{UTS} (MPa) AFSD-Wrought**		
	AFSD	*Wrought*		*AFSD*	*Wrought*
Mean	528	507	**Mean**	573	566
Variance	17	49	**Variance**	28	60
t-Stat	1		**t-Stat**	2	
P-value	2.9E-5		**P-value**	0.09	
A_{at} (%) AFSD-Wrought			**A_{after} (%) AFSD-Wrought**		
	AFSD	*Wrought*		*AFSD*	*Wrought*
Mean	6	9	**Mean**	7	16
Variance	3	1	**Variance**	1	2
t-Stat	-3.3		**t-Stat**	-11.2	
P-value	0.02		**P-value**	5.6E-7	

5.1.3 Elastic Modulus

The calculated % difference for elastic modulus compared to the ASTM standard for 7075 are listed in Table 5.6 [62]. Both the AFSD material and the wrought material had relatively small differences when compared to the literature value. A t-test was done to determine if there was a statistically significant difference in the elastic modulus between the AFSD and wrought material. Table 5.7 lists the mean, variance, t-stat, and p value results from the t-test run on the Young's modulus of the tested material. There was no statistically significant difference between the Young's moduli of the as-deposited and T6 AFSD material and the annealed and T6 wrought material.

Table 5.6 The difference between measured AFSD material compared to the literature value.

Sample Name	**E (GPa)**	**% Difference**
AFSD Z 7075-AD	68.6 $\pm$ 3.4	-2.1
AFSD Z 7075-T6	67.3 $\pm$ 1.2	-3.9
Wrought 7075-O	66.0 $\pm$ 2.4	-5.7
Wrought 7075-T6	67.4 $\pm$ 0.7	-3.5
ASTM 7075 [62]	70	

Table 5.7 The t-test results that compared the elastic modulus of the AFSD material to the wrought material before and after heat treatment.

E AFSD			**E Heat Treated**		
	AFSD	*Wrought*		*AFSD*	*Wrought*
Mean	69	67	Mean	68	67
Variance	12.8	1.6	Variance	7.9	1.9
t Stat	0.99		t Stat	0.92	
P(T<=t) two-tail	0.35		P(T<=t) two-tail	0.36	

5.2 Fractography 7075

5.2.1 Wrought 7075-T6

Compared to 6061 in the as-deposited and heat treated condition, 7075 was less ductile but had higher strength. For comparison to the AFSD material, the wrought 7075-T6 fracture surface was used as a baseline. Visually and with an optical microscope, it was expected to see necking or reduction of surface area and a fibrous fracture appearance with a shear lip around the outer rim of the fracture surface (typical cup/cone fracture) [57]. From the optical images of the wrought 7075-T6 fracture surface, a shear lip and spongy ductile core were observed, Figure 5.1.

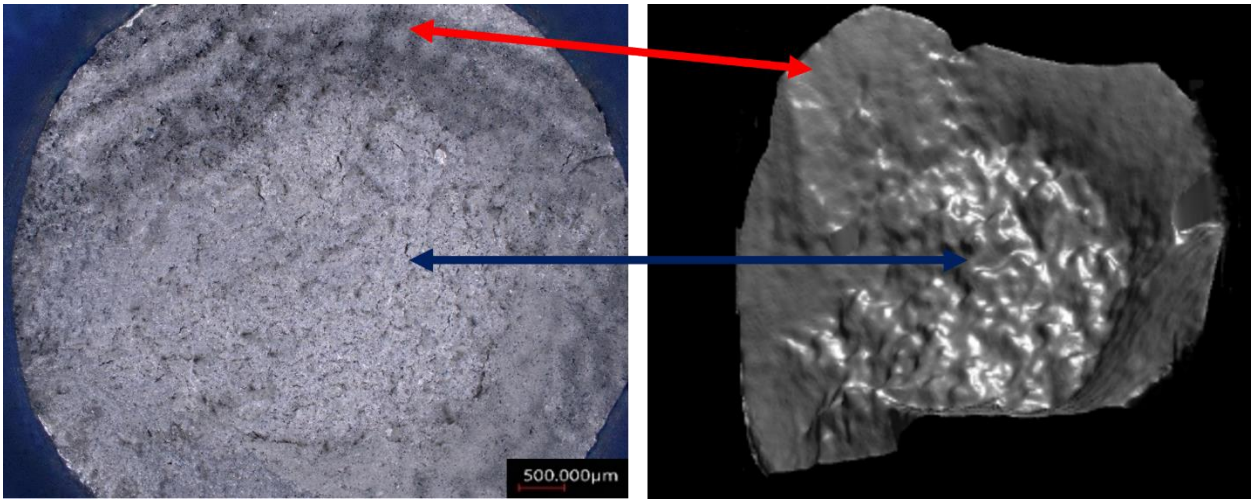

Figure 5.1 The optical image (left) at 5x magnification showed a dull fiberous appearance with the 3D rendering (right) showed the side profile of the shear lip (red arrow) and ductile fibrous center (blue), which indicated a ductile overlaod failure.

For a uniaxial tension test, the voids should appear round in shape at higher magnification. In the SEM, the wrought material showed microvoids or dimples with elongation in the direction of applied load, i.e., out of the page, Figure 5.2. Figure 5.2 was taken near the middle of the fracture surface to show the microvoids. Small secondary cracks in the fracture surface, as well as some quasi cleavage, was apparent. This was due to the tradeoff of between ductility and strength.

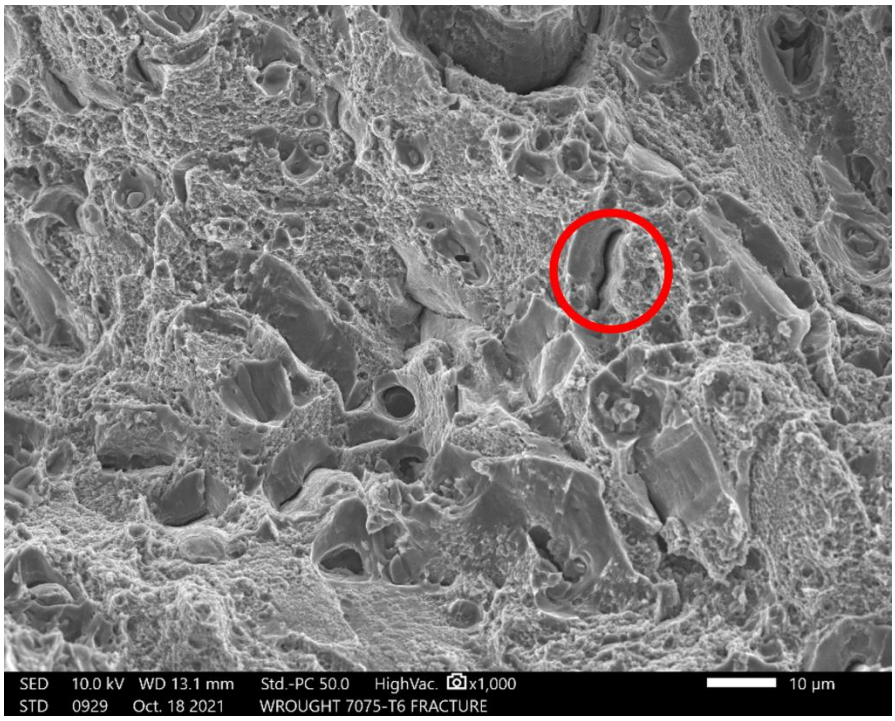

Figure 5.2 The center of the wrought 7075-T6 at 1000x showed microvoid coalsence indicative of ductile overload failure with a small secondary crack circled in red.

Finally, the metallographic analysis was expected to show that the grains in the wrought bar are oriented in the extrusion direction of the material. At the fracture surface it was expected to see random transgranular fracture [57]. Figure 5.3 shows that after polishing and etching of the cross-section that included the fracture surface, the samples showed grain flow that followed the direction of deformation.

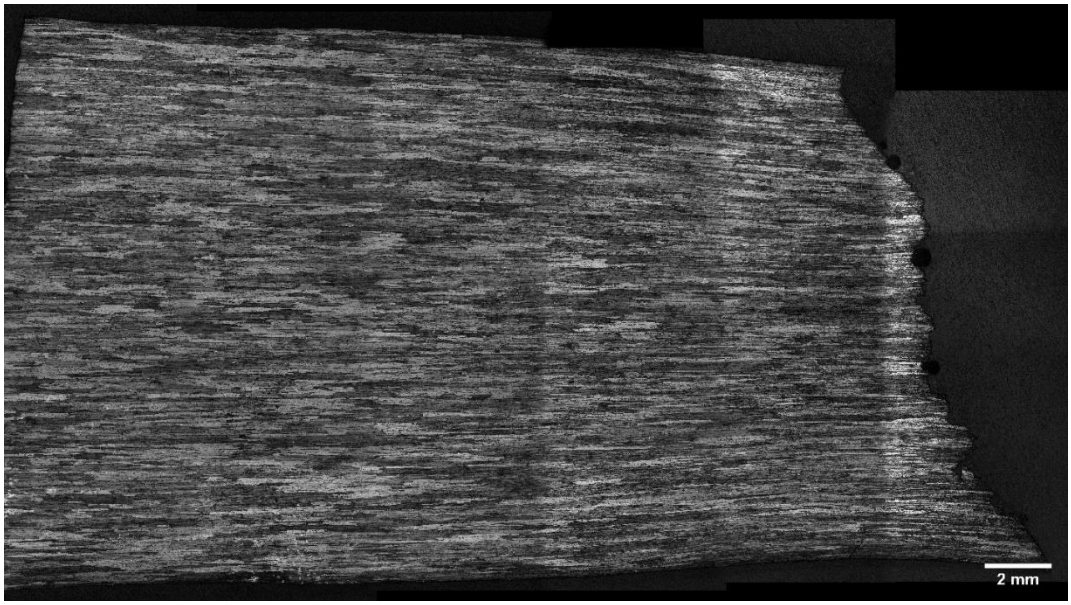

Figure 5.3 A cross section included the fracture surface of wrought 7075-T6 at 2.5X etched with Keller's showed that the grains were aligned in the extrusion direction.

5.2.2 AFSD Z 7075-AD

As mentioned in the tensile results section, the as-deposited material in both the Z orientation had low strength and good ductility. This condition was expected to exhibit indicators of ductile overload failure with a similar fracture surface as the 6061 as-deposited material. The fracture surface of the samples had a different fracture appearance compared to the 6061 samples. The fracture surface of the Z orientation samples often had an angle or spiked appearance instead of the traditional cup and cone seen in the AFSD 6061 as-deposited material. Figure 5.4 had an as-deposited fracture surface as a representative image. The overview image and the 3D rendering of the topography to the right of it show the angle of the fracture appearance. Despite this difference in appearance from the 6061 material, Figure 5.5, the fracture surface had microvoid coalescence throughout. In addition to these microvoids, as seen on the AFSD 6061-T6 samples the fracture surface had ledges on it. In the flat portion of the ledge, there were round microvoids while the sheared portion of the ledge that was perpendicular to the

flat portion had sheared microvoids. After etching with Weck's reagent, the grain structure was revealed to be very fine and did not show evidence of grain flow, Figure 5.6

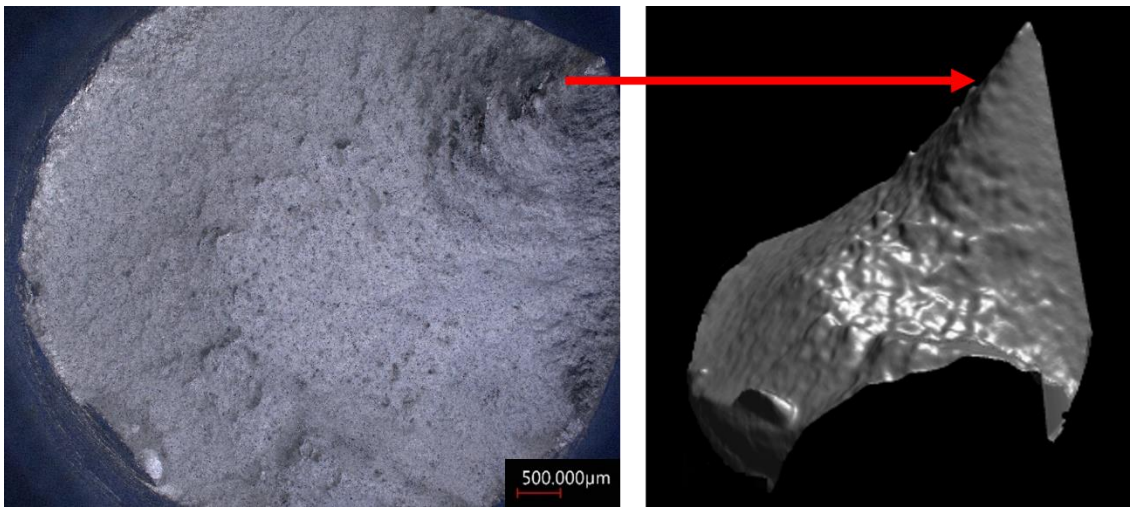

Figure 5.4 An overview image of Z 7075-AD #12 and the 3d rendering showing the spike of the topography.

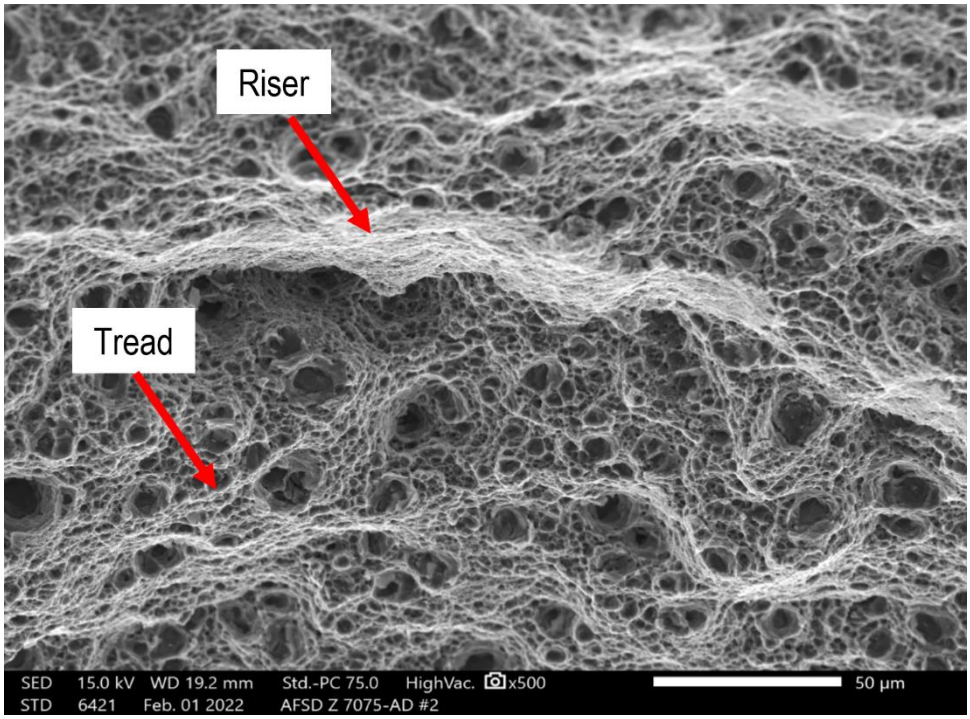

Figure 5.5 The fracture surface of the as-deposited 7075 material taken at 1000X, showing the flat tread and the sheared riser of the fracture surface.

Figure 5.6 The microstructure of the as-deposited AFSD Z 7075-AD #12 material etched with Weck's reagent showed a very fine-grained size at 150X.

5.2.3 AFSD Z 7075-T6

After heat treatment, the material was expected to show a reduction in ductility but the mechanism by which the material would fracture would still be ductile overload with, perhaps, quasi cleavage of the material [70]. However, the AFSD material in the Z direction samples had very little ductility when compared to the wrought material in section 5.2.1. Z direction material after heat treatment had a notable change in fracture appearance; the fracture surfaces were nearly completely flat. Figure 5.7 shows a fracture surface that was stitched together with ImageJ. From this, we can see a fracture surface with minimal reduction in cross-sectional area and a smooth appearance with a small shear lip around the sample. In the SEM, the fracture surface had a marked difference from the as-deposited material. Figure 5.8 shows that at high magnification, the fracture surface was smooth and granular, which is indicative of brittle failure. The grain size of the material increased in size after heat treatment, Figure 5.9 was etched with Weck's reagent revealed that the failure occurred along the grain boundaries.

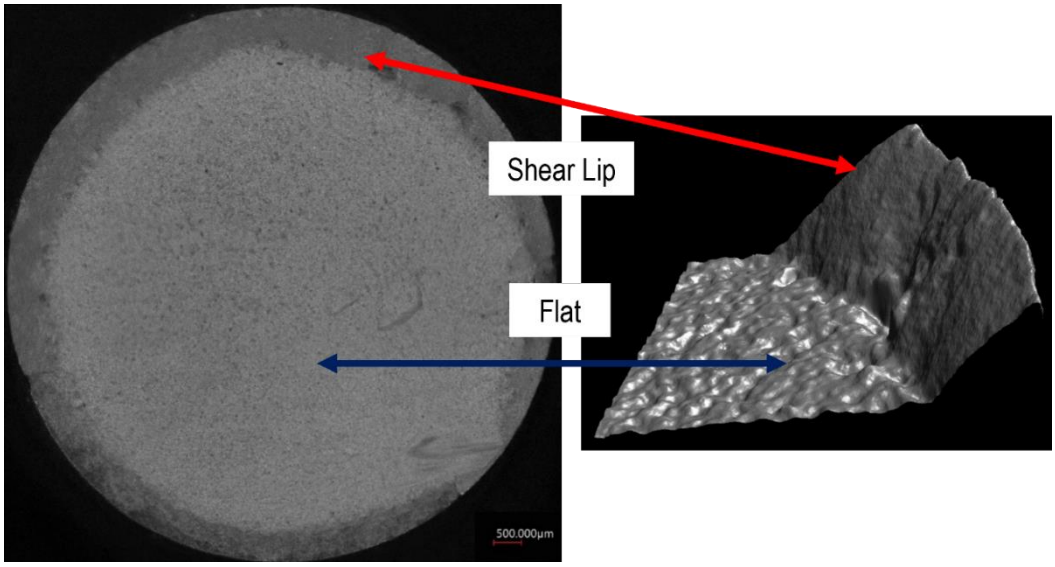

Figure 5.7 The overview image of Z 7075-T6 #4 was flat in appearance (left) with a shear lip all the way around the perimeter (right).

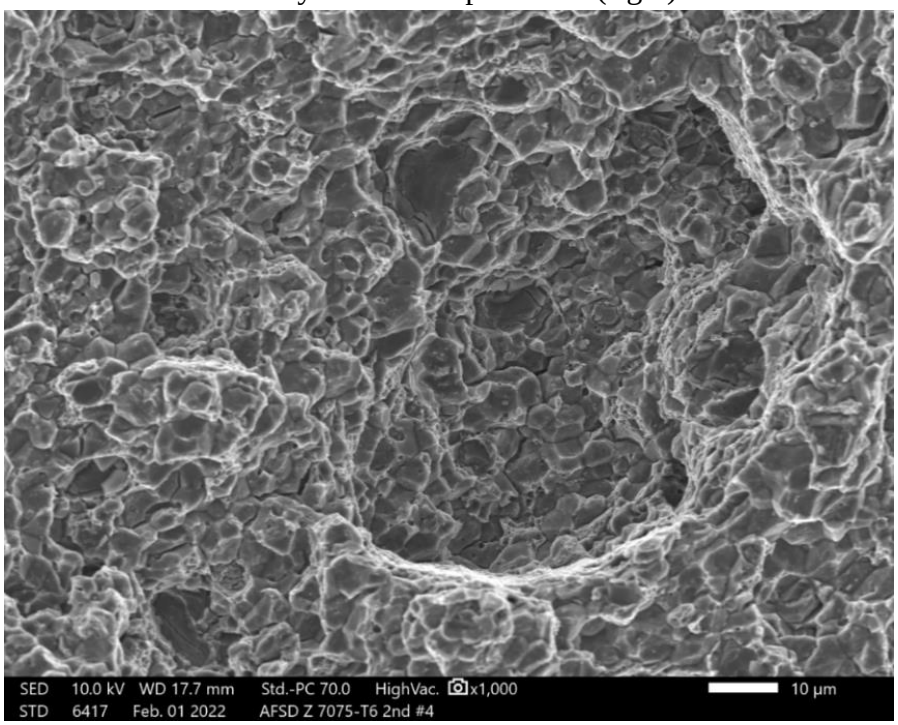

Figure 5.8 The fracture surface at 1000X was smooth and slightly faceted in appearance, which indicates brittle failure.

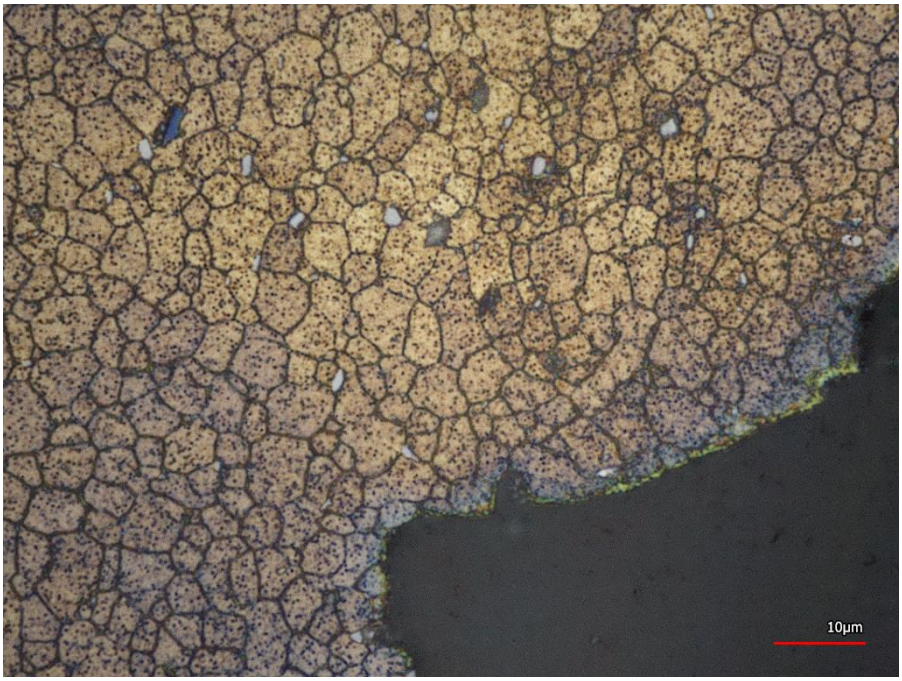

Figure 5.9 The microstructure of the heat treated sample of Z 7075-T6 #4 at 150X etched with Weck's revealed fracture occurring at the grain boundaries.

5.2.4 Particle Analysis of As-Deposited and Heat Treated Conditions

The expected precipitates on the fracture surface of the as-deposited and heat treated material should be like each other. The precipitates that form after heat treatment in 7075 were expected to be rich in Mg, Zn, and Cu. Where the fine coherent particles should be in the phase $Mg(Zn, Cu, Al)_2$. Figure 5.10 shows the baseline EDS analysis of the wrought 7075-T6 material which had Mg and Si rich particles with Mg, Zn, and Cu are evenly dispersed.

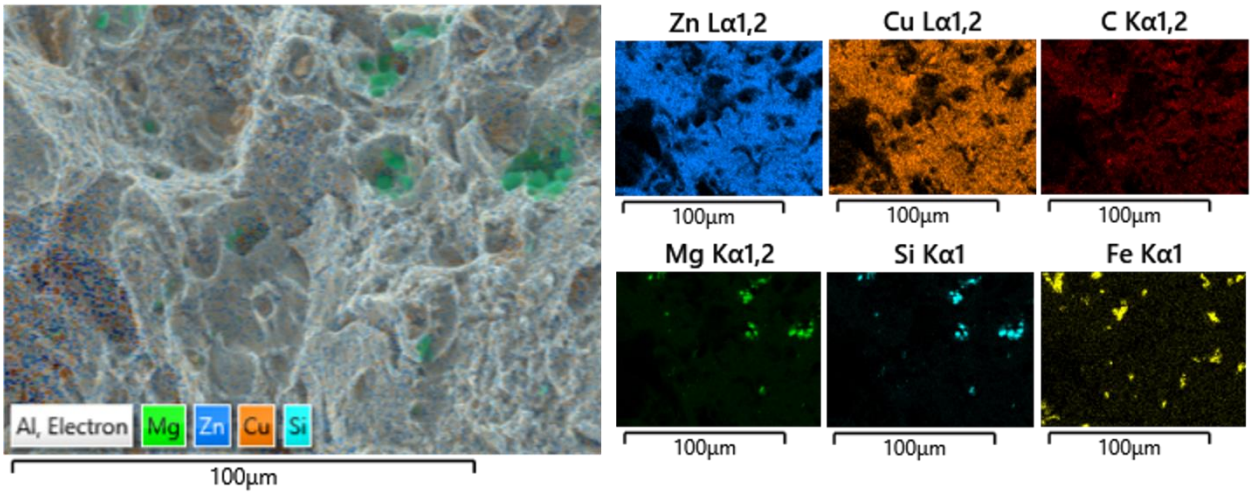

Figure 5.10 An EDS map showing of the wrought 7075-T6 sample #4 had particles that were rich in Mg and Si and there were smaller Mg, Zn, and Cu rich particles dispersed throughout the fracture surface.

In the as-deposited condition, an EDS map showed that the larger particles in the microvoids were Mg and Si rich while the smaller and more dispersed particles were Mg, Cu, and Zn rich, Figure 5.11. After heat treatment, the particles did not change in elemental analysis. Figure 5.12 shows that the larger particles were still Mg and Si rich. Smaller particles were still Mg, Cu, and Zn rich and were still evenly dispersed in the matrix.

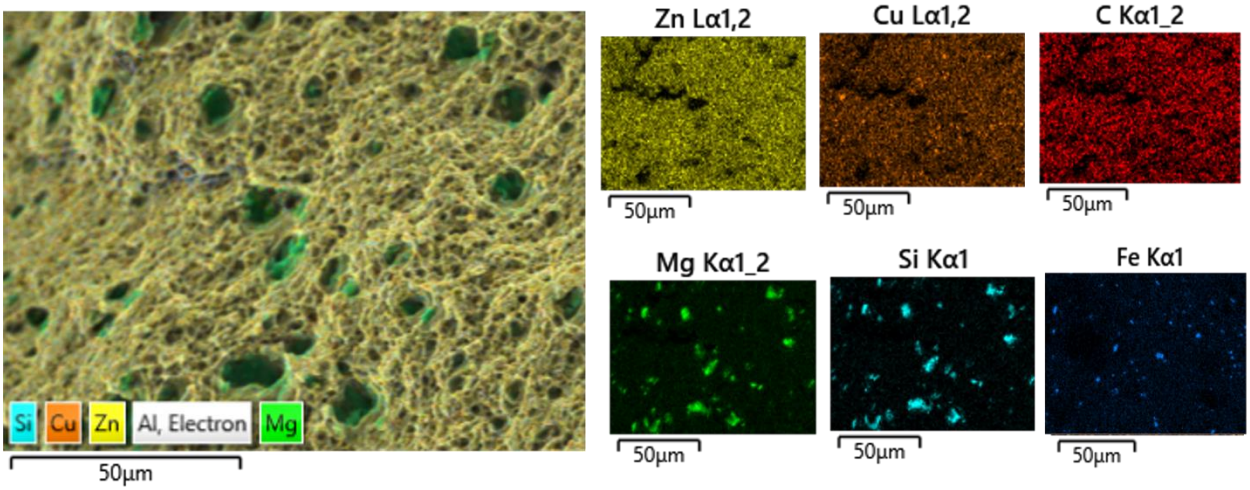

Figure 5.11 An EDS map showing that the particles were rich in Mg and Si and there were smaller Mg, Zn, and Cu rich particles were dispersed throughout the fracture surface of sample AFSD Z 7075-AD #9.

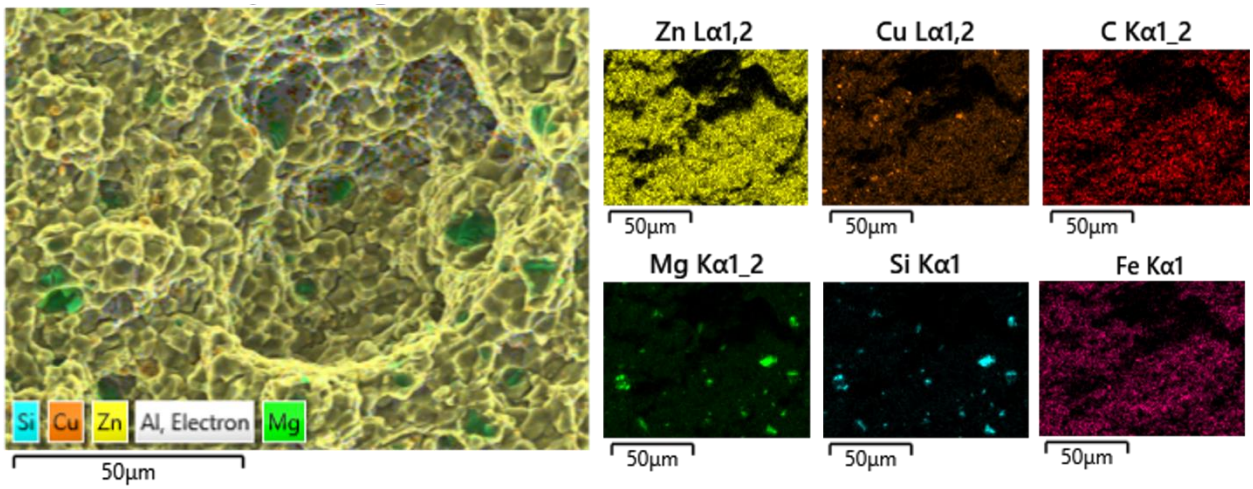

Figure 5.12 An EDS map of the heat treated material showing Mg and Si rich large particles with smaller Mg, Zn, and Cu rich particles dispersed throughout the fracture surface in sample AFSD Z 7075-T6 #4.

5.3 Outliers of 7075

While all the fracture surfaces in the Z direction after heat treatment had a significant loss of ductility, three notable outliers were identified in the tensile data in both the as-deposited and heat treated condition. What is most important to note is that these samples were sectioned next to one another on the same build; 13, 14, and 15 were located on the second build in the same 1.5" section.

5.3.1 AFSD Z 7075-AD #13

In the as-deposited condition, the 7075 material was expected to have an elongation at fracture of 18%, but sample #13 failed at 5% elongation. The material did reach the correct yield strength but did not meet the expected ultimate strength due to the low ductility. The optical image of the fracture surface stitched together with ImageJ, Figure 5.13, showed the flat appearance of the fracture surface without the expected necking of the cross-sectional area associated with ductility. The fracture surface overview showed dark lines that point towards one point on the edge which was expected to be the initiation site for the fracture. In the SEM, the location marked in red in Figures 5.13 and 5.14 were dark in color. Higher magnification showed

that the fracture surface had a smooth appearance with some sections appearing darker in color. An EDS analysis revealed that the dark areas in the SEM image of Figure 5.14b were carbon rich, Figure 5.15. The measured carbon amounts were close to 50wt%. Unfortunately, EDS does not accurately measure the amount of carbon on the fracture surface due to carbon's low atomic number. Since graphite lubricant is used carbon was a potential contaminate. The etched microstructure showed fine grained microstructure, Figure 5.16

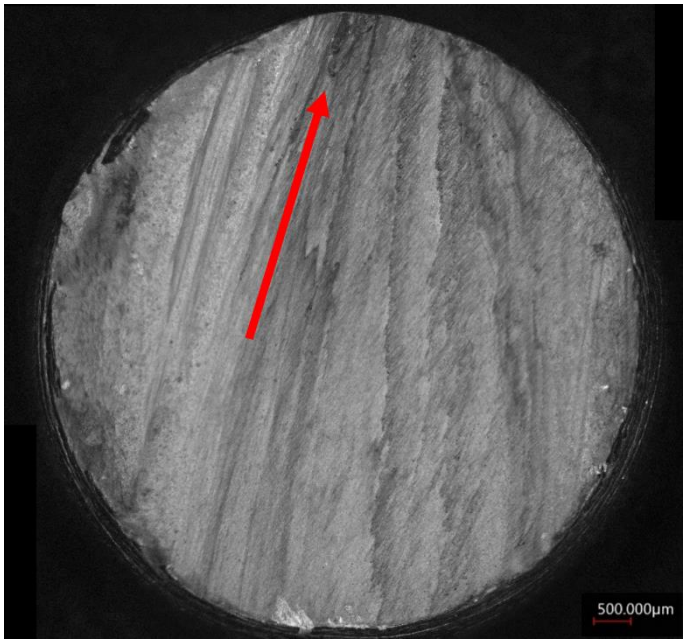

Figure 5.13 The fracture surface was flat with dark lines running across the surface that pointed towards the outer edge (red arrow).

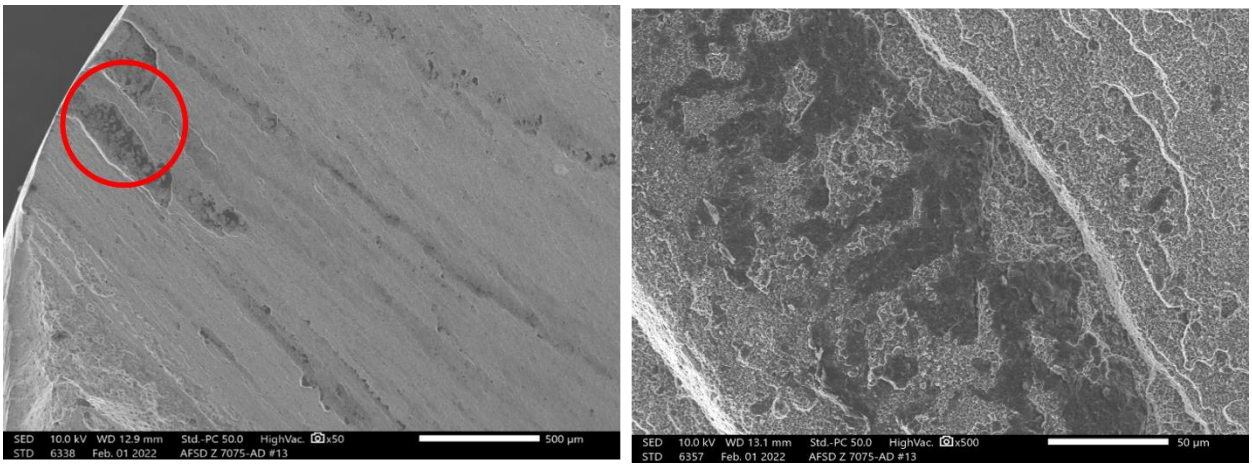

Figure 5.14 Sem image of the fracture surface at the fracture initiation site (a) 50X and its appearance at higher magnifications (b) 500x.

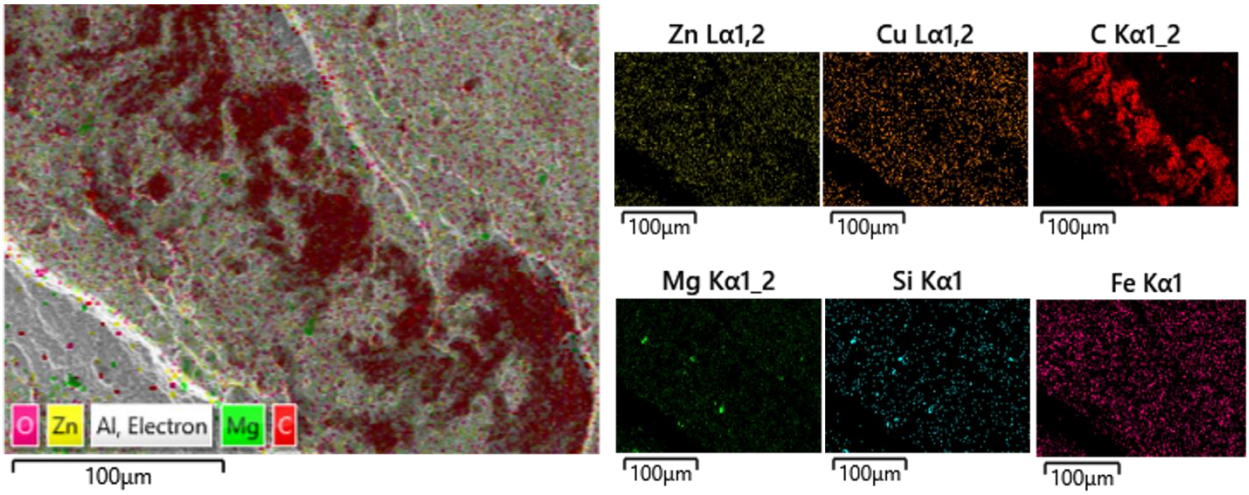

Figure 5.15 An EDS map showing a carbon rich area along with the expected Mg, Si, Zn and Cu elements.

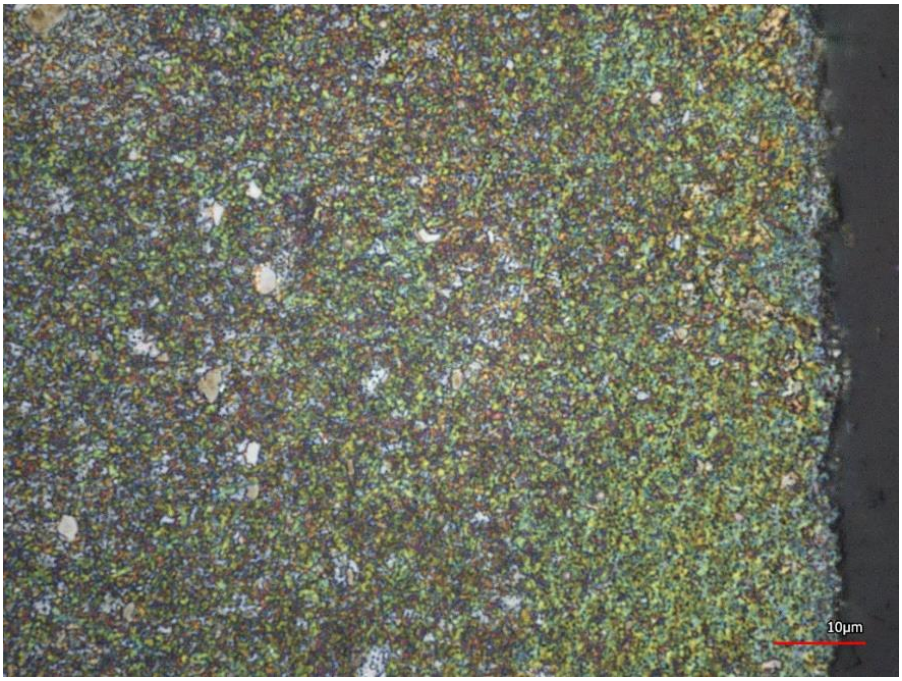

Figure 5.16 The cross section of the fracture surface at 150x with a Keller's etch revealed a fine grain structure.

5.3.2 AFSD Z 7075-T6 #14

This loss of ductility occurred again in the heat treated sample that was next to the #13 sample. Sample #14 had 0% elongation after fracture when the expected elongation after fracture should be closer to 7%. This sample also had no yield point and only reached less than half of the expected ultimate strength. The fracture surface, Figure 5.17, had two different zones as opposed to the other 'normal' flat fracture typical of the AFSD 7075 heat treated material. The initiation zone had a 'wavy' appearance before it reached the fast final fracture. Next to the overview image of the fracture surface, the 3D rendering of the fracture surface showed that while visually it appears there are 'waves' on the fracture surface these waves did not have any topographical difference that was severe enough to be detected with the optical profilometer.

Figure 5.17 An overview of the fracture surface (left) and the 3d rendering of the red circled ‘waved’ section (right).

In the SEM, this darker ‘wave’ was still visible, however, at higher magnification, the appearance of the fracture surface was the same as seen in the other heat treated samples. Figure 5.18 shows a section near a wave imaged at higher magnification showed a similar appearance to the heat treated AFSD 7075 material that was granular in appearance. EDS analysis did not detect carbon in high amounts, Figure 5.19. The etched fracture surface, Figure 5.20, had a similar appearance to the other etched samples of similar heat treatment.

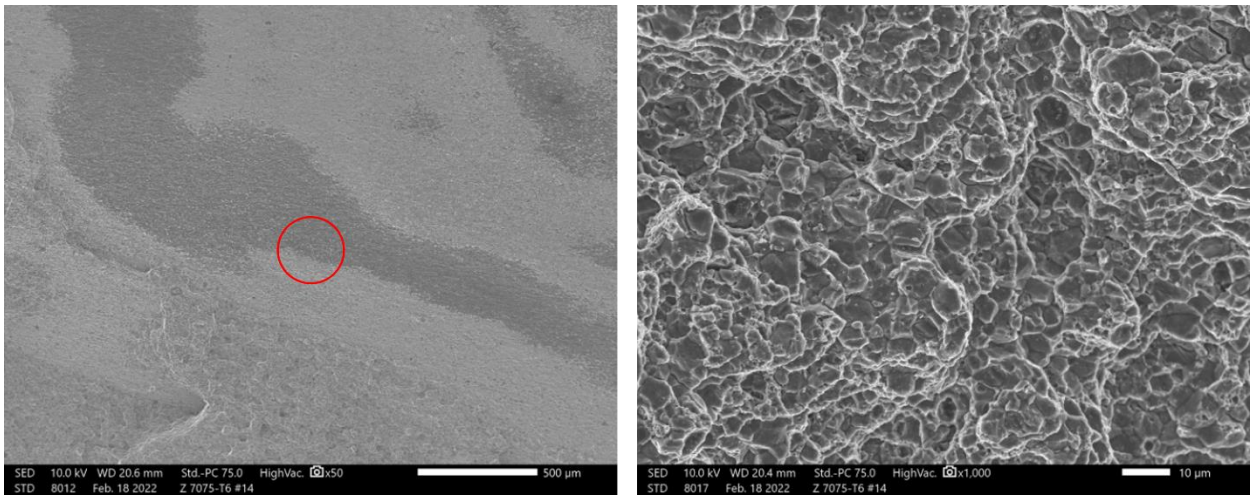

Figure 5.18 The fracture surface at 50X (left) and the fracture surface at higher magnification showing a smooth appearance 1000x (right).

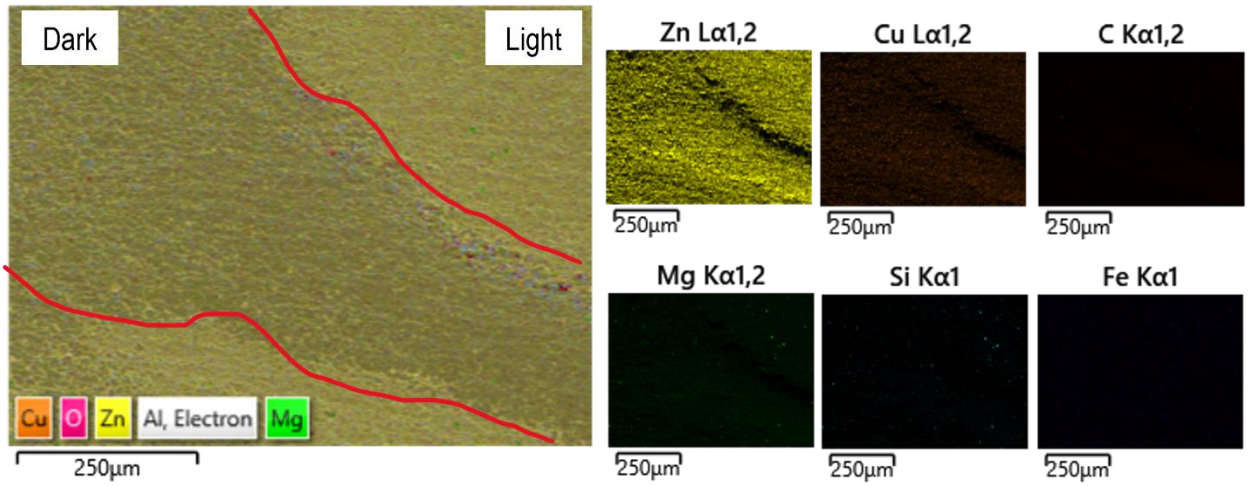

Figure 5.19 EDS map of the dark section of the wave outlined in red did not show a difference in chemistry or carbon in high amounts.

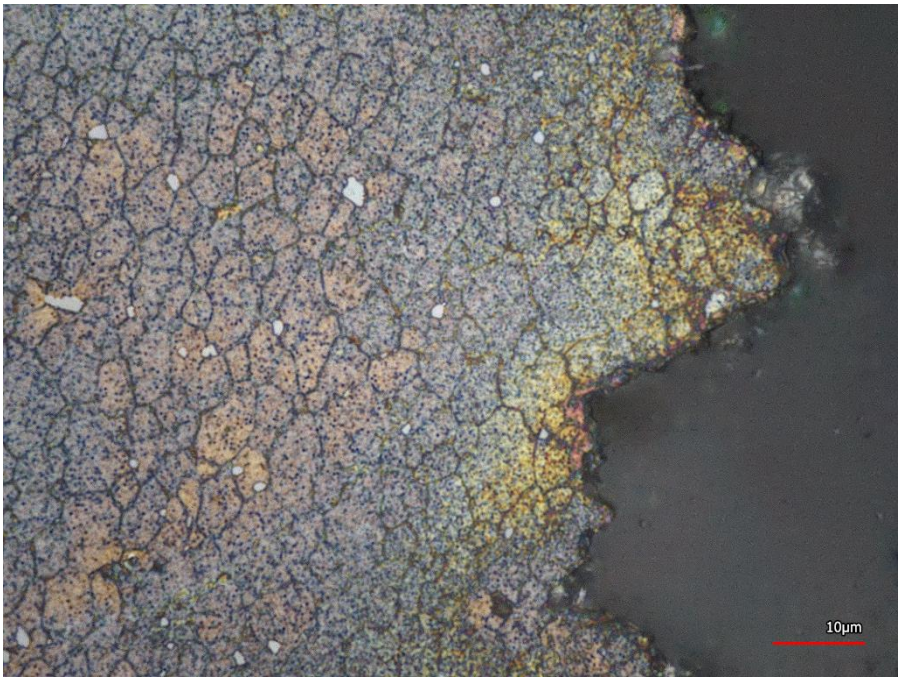

Figure 5.20 Sample AFSD Z 7075-T6 #14 near the fracture surface etched with Weck's and at 150X showed failure occurs at the grain boundaries.

5.3.3 AFSD Z 7075-T6 #15

The fracture surface of this sample also had a low elongation after fracture (3%) and the yield and ultimate strength values were low. An overview of the fracture surface, Figure 5.21, had a dark smudge at the top, which was probably the initiation site for the fracture. The initiation site was smoother in appearance and started on the outside edge of the fracture surface, Figure 5.22. The fracture was brittle across the remainder of the fracture surface. At higher magnification, the fracture surface appeared smooth and granular. EDS analysis did not show carbon in any high amounts; however, the fracture surface did have a similar dark appearance optical as the previous outliers, Figure 5.23. Figure 5.24 shows that the etched fracture surface of this material had failure that initiated along the grain boundaries.

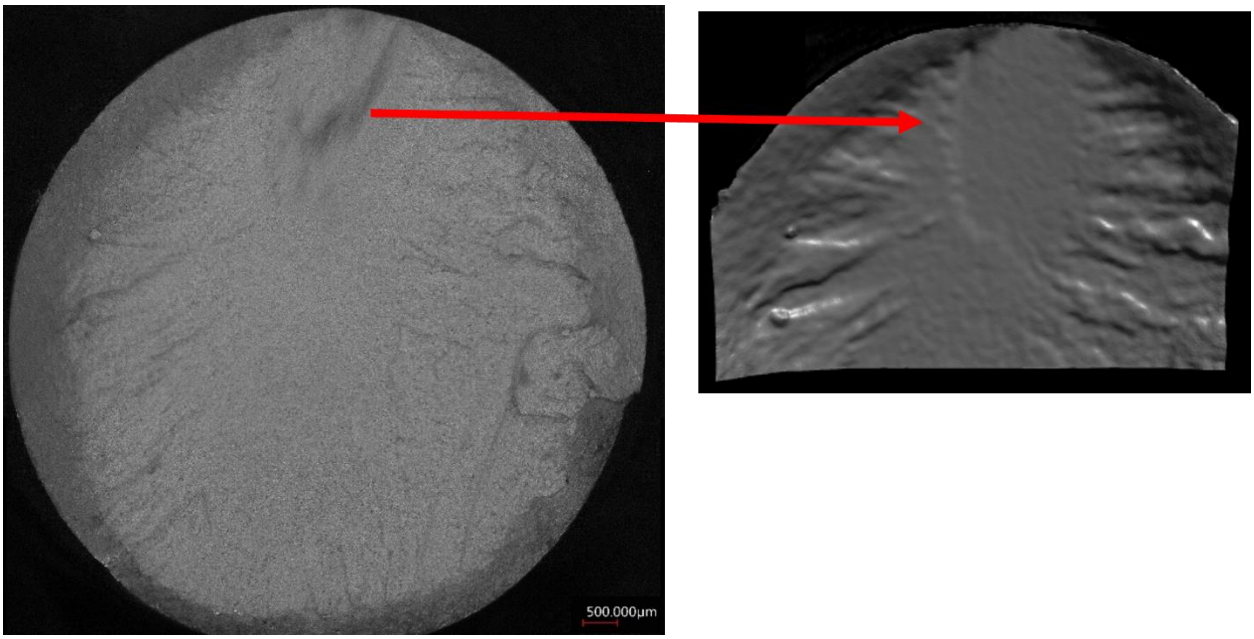

Figure 5.21 The fracture surface of the AFSD Z 6061-T6 #15 material and the topographical 3D rendering of the initiation site.

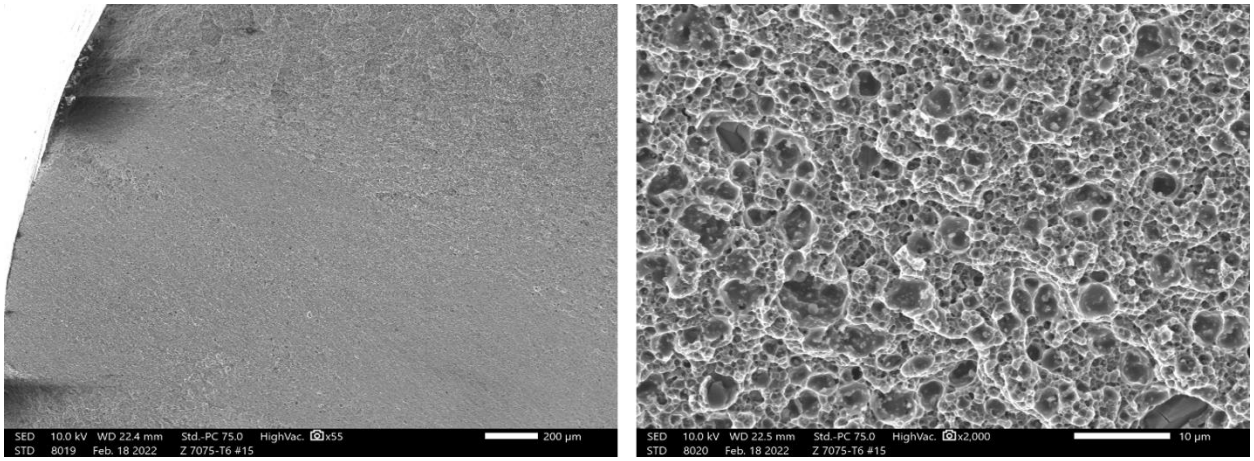

Figure 5.22 The initiation of the fracture was smooth in appearance (top) 55x and at higher magnification is appears to have a smooth granular appearance (below) 2000X.

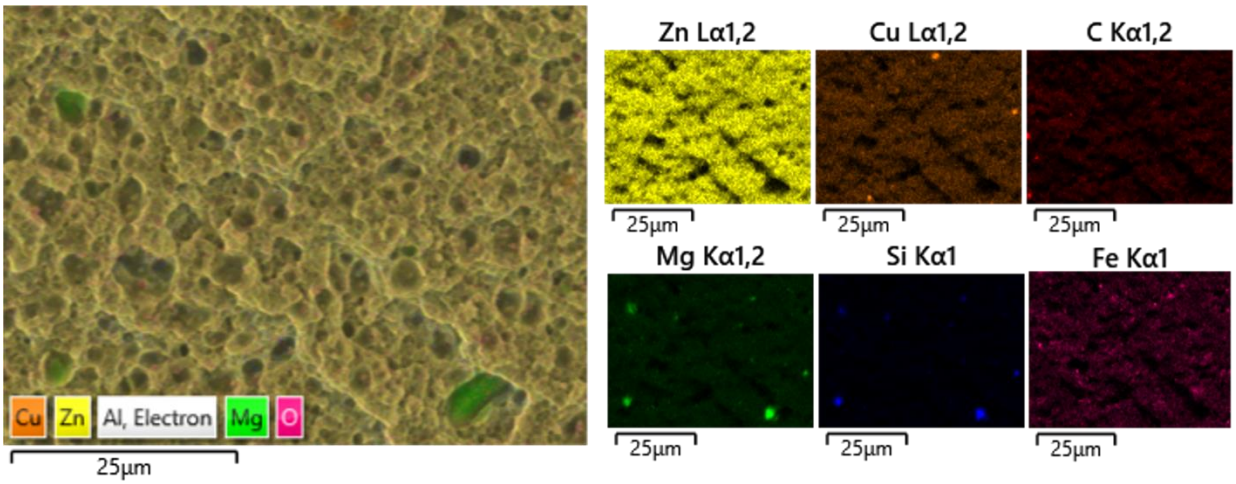

Figure 5.23 The EDS map showed expected elements with very little carbon or oxygen.

Figure 5.24 The cross section of the fracture surface at 150x after etching with Weck's reagent revealed that fracture was along the grain boundaries.

5.4 Raman Spectroscopy

It was suspected that carbon contamination was the cause of the poor ductility in the tensile specimens and that excess carbon was the cause of the outlier failures in samples 13, 14, and 15. Polished 7075 samples were analyzed for the presence of carbon using EDS, but it was difficult to determine if the amount of carbon was significant or what phase the carbon was in. Raman spectroscopy was used to determine the phase and presence of carbon in polished but

unetched samples. Two samples were investigated, a heat treated 7075 material (sample #4) that had good ductility (7%) and one of the outlier samples (#14) that had a catastrophic failure with no yield strength and 0% elongation. Figures 5.25 and 5.26 show the unetched images of samples #4 and #14. What is important to notice is that in sample #4, while there appears to be little carbon at low magnification, at higher magnification there was carbon throughout the microstructure. When compared to the outlier sample #14, there was a greater presence of carbon. Figure 5.26 showed that the carbon was in bands that were approximately 4 mm apart. Raman spectroscopy was completed on numerous particles in this sample. The Raman shift for the graphite lubricant spray and the particles in samples #4 and #14 is shown in Figure 5.27. The graphite spray is representative of disordered graphite before and after the heat treatment [67], [71]. The Raman shift for the particles in the microstructure indicated amorphous carbon [71].

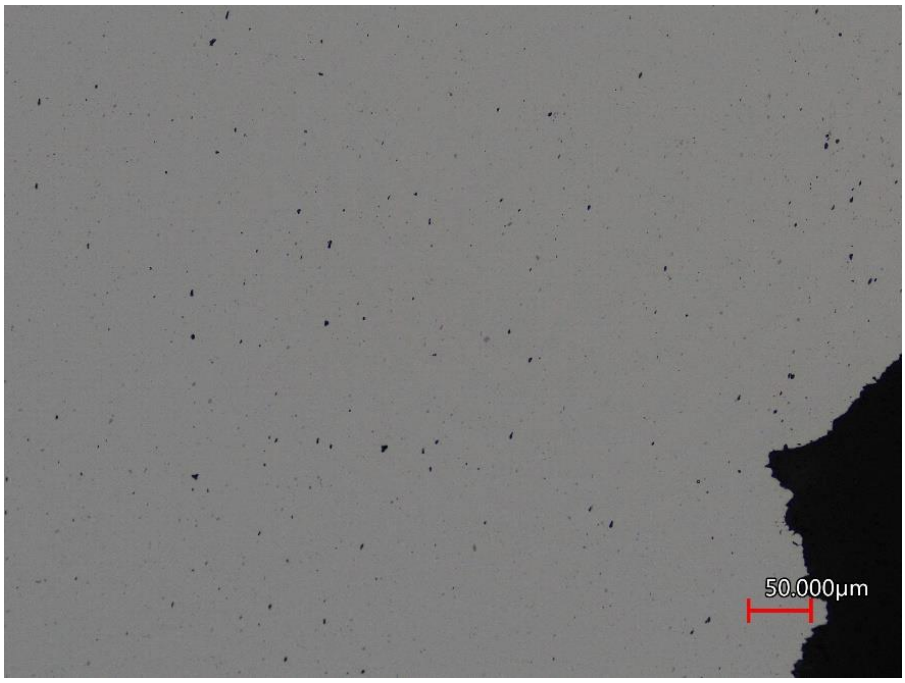

Figure 5.25 The unetched AFSD Z 7075-T6 #4 did not have noticeable banding of carbon particles at 20X.

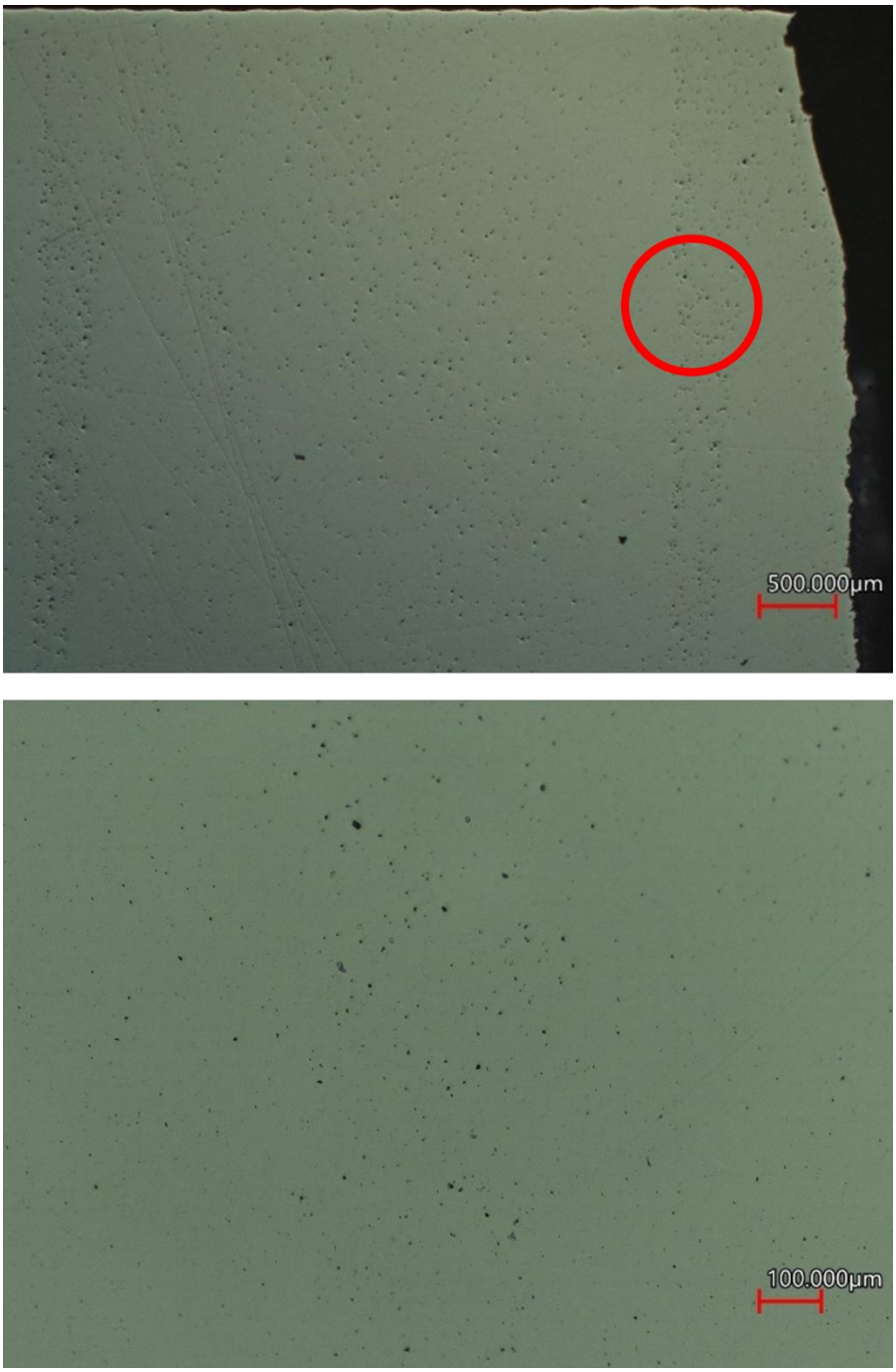

Figure 5.26 The outlier sample had lines where carbon was deposited in the microstructure of the unetched samples #14 at 2.5X (above) and 10X (below).

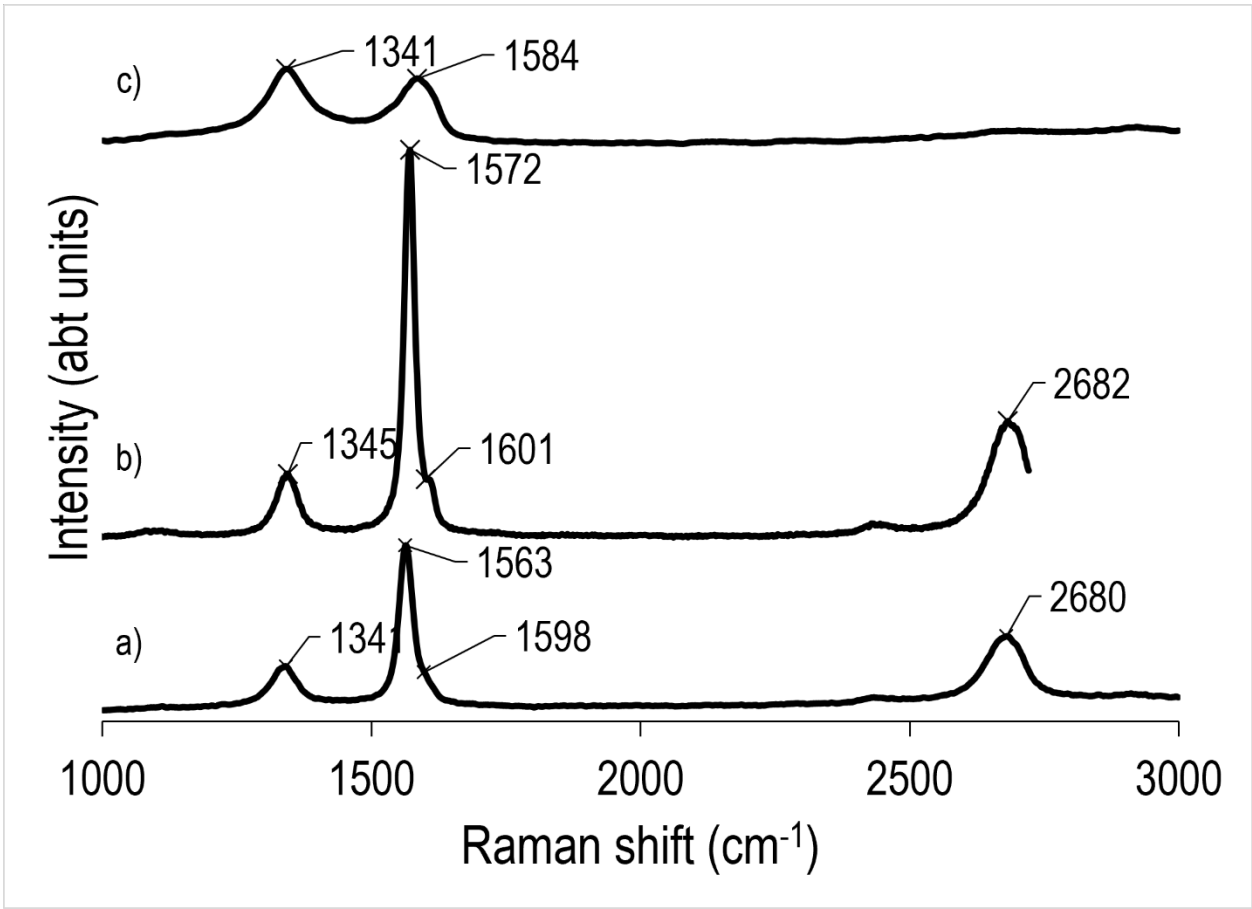

Figure 5.27 The Raman shift for the graphite spray as sprayed (a) after heat treatment (b), and the dark particles suspected to be carbon (c) in the unetched microstructures.

Chapter 6 Discussion

6.1 Mechanical Properties

As stated previously, the as-deposited condition for the AFSD material was low strength with high ductility. The feedstock material in both the 6061 and 7075 AFSD builds were in the fully hardened condition, but during AFSD the strengthening precipitates were expected to go back into the solution. Figure 6.1 shows a graph of the solubility of various elements and precipitates as a function of the hot working temperature [32]. On this graph, the temperatures of the AFSD deposits are noted by red lines. Under the assumption that the deposits are kept at or near the working temperatures for most of the build time, it would be expected that the material in the as-deposited state would be soft and ductile due to the dissolution of the strengthening precipitates and alloying elements.

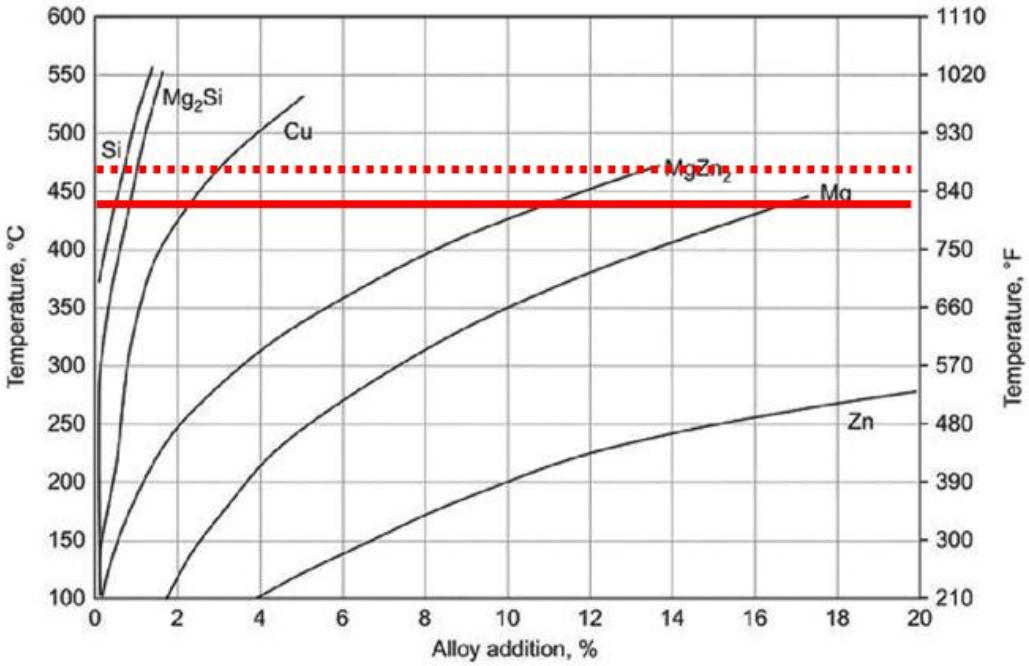

Figure 6.1 The dotted line is located at the working temperature for 6061 and the solid line was the the working temperature for 7075 [55].

The EDS analysis of the particles observed on the fracture surfaces showed that most of the particles still present in the microstructure of both 7075 and 6061 in the as-deposited

condition were those that were rich in Mg and Si. At the working temperature of the 6061 materials, most of the Si and Mg should dissolve back into the matrix. With the 7075 materials, the Mg, Zn, and Cu additions are expected to be almost completely dissolved in the matrix. Coarse particles such as the Mg_2Si may still be present, and this was confirmed with the EDS analysis of the fracture surfaces.

The effects of the cold working are expected to be negligible as the heat treatment for 6061 and 7075 is the main strengthening contributor. The heat treatment of the 6061 showed that, statistically, only the elongation varies with the Z and X directions. When designing with the AFSD process in mind, it is therefore important to include the fact that the directionality of the strength is negligible, but the elongation is dependent on build orientation.

The mechanical behavior of the 7075 is predominantly controlled by the effects of the graphite lubricant used. Although it reaches strengths required for both the wrought and forged products its elongation is severely affected. This is most likely since the carbonaceous material is spread throughout the layer and at the layer interfaces during deposition. It is expected that the reduction or elimination of the graphite lubricant would greatly increase the peak strength without such a detrimental effect on the elongation.

6.2 Fracture Mechanisms

In hot worked or forged material, failure or fracture is often initiated at defects, such as an intermetallic phase (IMP) or along microstructural discontinuities such as high grain flow sections. Both the 6061 and 7075 material had microstructural discontinuities caused by the AFSD process where the interfaces between the layers caused more recrystallization. In addition,

the use of graphite lubricant or the formation of oxides can cause inclusions in the material that act as stress risers.

6.2.1 6061

In the 6061 materials, the fracture mode was dominated by the failure at microstructural discontinuities. This was evident in the topographical appearance of the fracture surfaces. In the as-deposited condition, this topography was not as evident since the failure was due to ductile overload. However, after heat treatment, this behavior was very apparent due to the growth of the grains in the build direction. After heat treatment, the AFSD Z direction microstructure had grain coarsening where the average width of the grains was 0.89 mm while on the fracture surface the riser height was 0.86 mm. This notes that while the failure is most likely occurring at the grain boundaries. Because the grains grow and elongate in the direction of the layers, the AFSD Z direction samples failed like a layered composite where the layers delaminated at the interfaces in a smooth appearance while the layer interiors were ductile. Figure 6.2 showed a simplified proposed mechanism of failure of the Z direction samples. Although this failure mode is fairly consistent, failure can occasionally occur rapidly at a grain boundary and cause lower ductility in the case of sample AFSD Z 6061-AD #5.

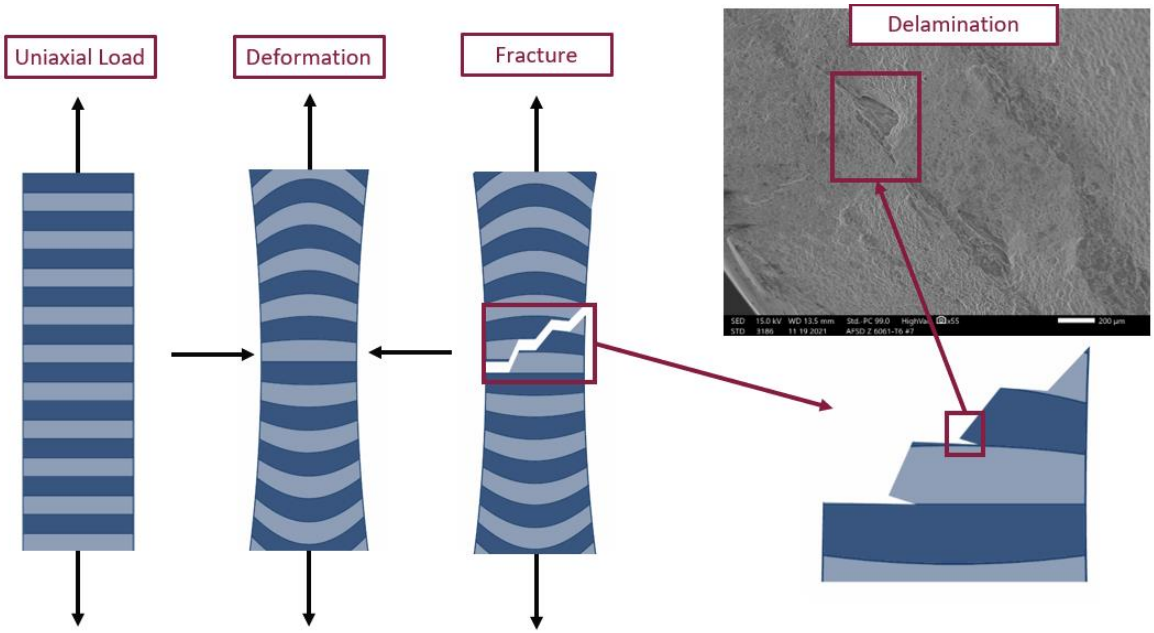

Figure 6.2 The proposed mechanism of failure shows that at the fracture surface it has a stepped appearance due to the delamination of the layers.

In the X direction AFSD samples, failure is like a composite where the grain boundary interfaces are points of weakness in the sample. After heat treatment, the interfaces are less ductile than the layer interiors. The secondary cracks seen in the facture surface, most notably in the heat treated X direction, are thought to occur due to residual stress in the sample caused by elastic spring back. The proposed method for this is that the reduction of the surface area during necking generates compressive stresses in the direction perpendicular to the tensile load. Once the specimen breaks the sudden release of the applied load the compressive stresses are released, and the layers are pulled apart. Figure 6.3 shows a diagram of the proposed method by which the failure occurred. This is less severe but still apparent in the as-deposited material as the fracture surface inside the secondary cracks are dimpled with microvoids in the direction perpendicular to the applied load. If these secondary cracks formed from something like fiber pullout the microvoids would be sheared in the direction of the applied load.

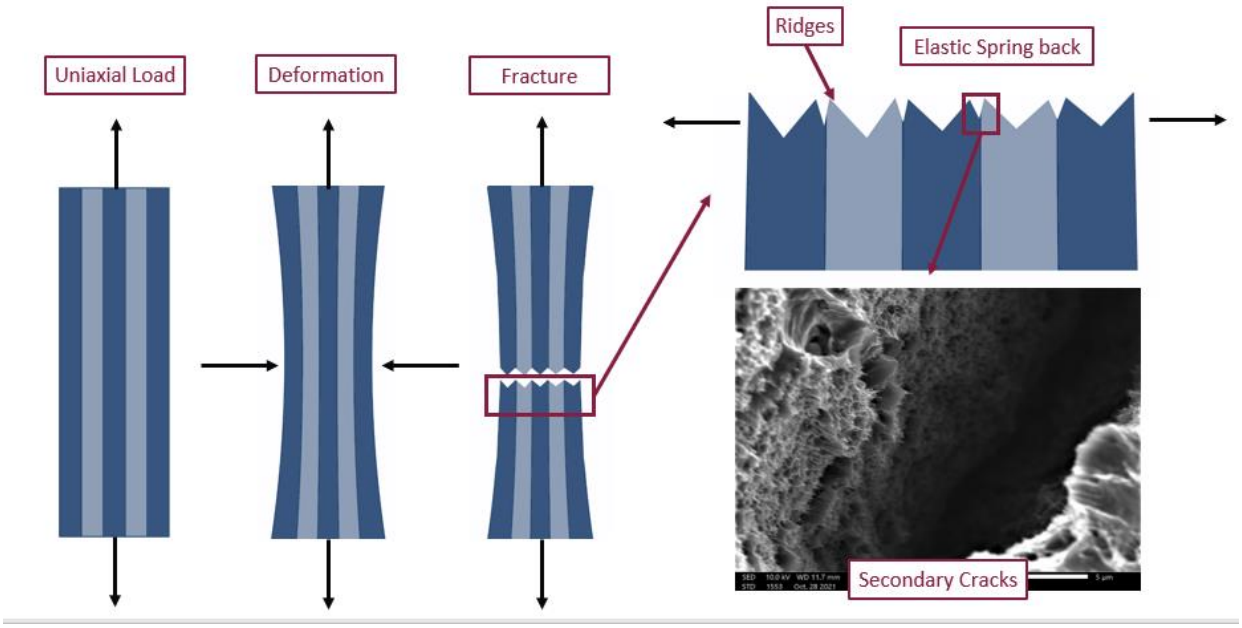

Figure 6.3 The proposed mechanism of failure shows that at the fracture surface elastic spring bake causes the secondary cracks in the fracture surface.

6.2.2 7075

In the 7075 builds, the failure mode was dominated by the presence of intermetallic phases which have been identified as carbon that is most likely from the graphite lubricant spray used during production. Mapping of these particles showed that, in the as-deposited condition, the particles were round in appearance at the interfaces and more densely populated. After heat treatment, the graphite did not go into solution in the aluminum. Thus, failure initiated at the layer interfaces and acted as a composite with high strength but limited ductility. The use of graphite lubricant will cause issues with quality control since excess carbon on the feedstock material may cause premature failure, as in the case of samples #13, 14, and 15 which were in a 1.5" section at the beginning of the build wall. These failures point to the fact that even if the AFSD process successfully mixes into the matrix IMPs there are discontinuities between the layers and the layer interfaces that may cause unpredictable mechanical properties and premature failure.

6.3 Heat Treatment and Grain Growth

The 6061 materials underwent grain coarsening during heat treatment. Figures 6.4 and 6.5 show the progression of the grain size in the 6061 AFSD in the X and Z direction material after annealing and after the T6 heat treatment (anneal, solution, quench, age) for both the X and Z directions. In the 7075 materials, the grain size was fine but did not coarsen much after the heat treatment when compared to the 6061 material, Figure 6.6. Both 6061 and 7075 have alloy additions of Cr, Zr, and Mn which stabilize the sub-grain structure and prevent recrystallization [55]. The 7075 materials had much more Zr which accounts for the limited grain coarsening compared to the 6061 AFSD material. Overall, the 7075 had more alloying elements than 6061 that can serve as dispersoids that can pin the grain boundaries and prevent recrystallization [55].

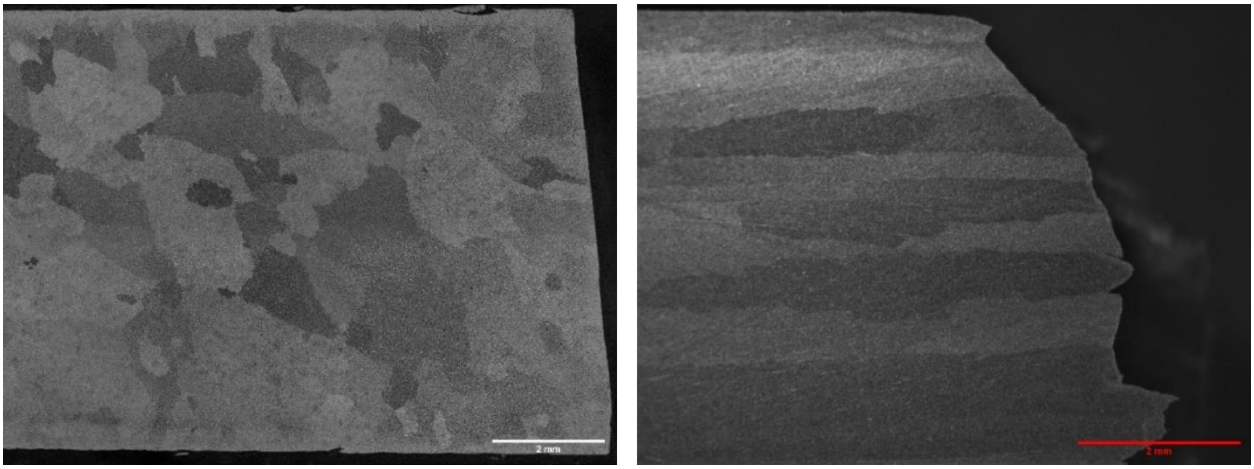

Figure 6.4 AFSD X (left) #2-1 annealed, (right) #2-2 fully heat treated showing the change in grain size.

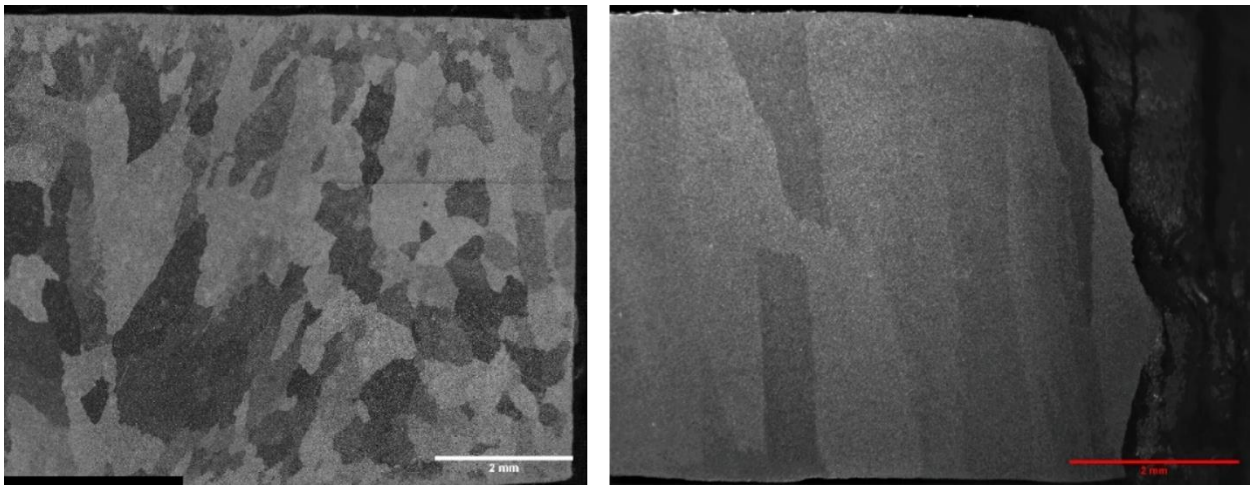

Figure 6.5 AFSD Z 6061 (left) #11 annealed (right) #9 fully heat treated at 2.5X showing the change in grain size.

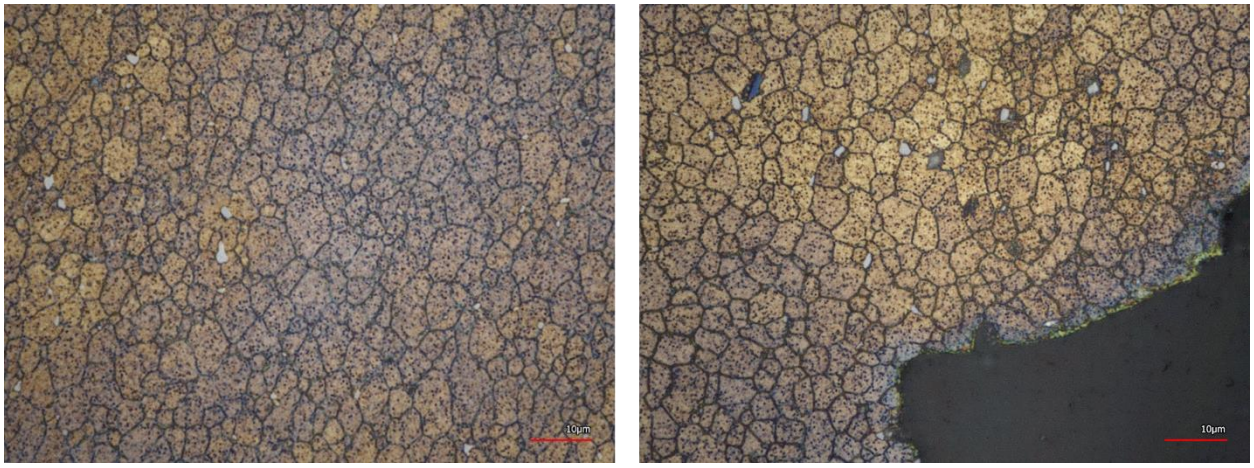

Figure 6.6 AFSD Z 7075-AD #12 (left) after annealing and AFSD Z 7075-T6 #14 fully heat treated (right) etched with Weck's reagent imaged at 150X showing the change in grain size.

Chapter 7 Conclusions

7.1 Overall Conclusions

- A post processing heat treatment of the AFSD material was required to achieve industry standard mechanical properties.
- After heat treatment, both the 6061 and 7075 material experienced grain coarsening.
- Eliminate the use of graphite lubricant when printing 7075 as entrapped graphite impurities can cause poor ductility and increased variability in mechanical properties.

7.2 6061

- Mechanical Properties
    - As-deposited material was soft and ductile, due to the dissolution of precipitate particles during AFSD processing.
    - AFSD 6061 required a heat treatment to meet the minimum strength requirements for a forging.
    - After heat treatment, both build directions increased in strength with no statistically significant difference in values.
    - Z direction samples did not meet minimums for elongation and had notable outliers in the results.
    - The quality index ranked X direction higher in both the as-deposited and heat treated conditions due to the higher elongation and higher strain energy density and lower variability in the measurements.
- Fractography
    - Layer direction affected failure mode and fracture surface appearance.
    - A potential source of the secondary cracks and delamination in the X and Z build directions in the heat treated conditions are potentially oxide films.
    - Particles in both the heat treated and non-heat treated conditions show Mg and Si rich particles as expected.
- Microstructure
    - As-deposited material showed a fine grain size with flow lines in the direction of the build layers.
    - After heat treatment, both the X and Z directions exhibited grain growth in the direction of the layers.

- Outliers
    - Outliers were investigated and determined to either exclude or include these values in the quality index calculations.
    - AFSD Z 6061-AD #13 potentially failed due to contamination during the process which can be reasonably mitigated with quality control measures and was thus excluded from average values.
    - AFSD Z 6061-T6 #5 was not excluded from the averages as it represented a potential for random failures associated with this process such as oxide formation or poor interfacial bonding.

7.3 7075

- Mechanical Properties
    - AFSD 7075 required a heat treatment to meet the minimum strength requirements for a forging.
    - The average ultimate tensile strength was higher than the literature but had higher variability.
    - The quality index was like that of the annealed wrought material in the as-deposited condition but was lower than the wrought 7075 material after heat treatment.
    - With outliers removed, mechanical strength averages were better than wrought material.
- Fractography
    - As-deposited material had similar steps as seen in the 6061 Z direction fractures.
    - Graphite affected the fracture behavior of the heat treated AFSD 7075 material.
    - In the heat treated condition, the fracture appearance was granular and smooth which indicates a brittle like fracture.
    - EDS analysis showed Mg, Cu, and Zn uniformly distributed with coarse Mg and Si rich particles most likely Mg_2Si.
- Metallography
    - Raman analysis of the unetched samples of AFSD 7075 material showed particles that were carbon rich.

    - The as-deposited AFSD material had a fine grained microstructure with grain coarsening after heat treatment.
    - Analysis of the fracture surface cross-section showed the fracture occurred along the grain boundaries in the heat treated condition.
- Outliers
    - Three outliers were identified near one another and showed evidence of excess graphite lubricant that caused the premature failure.

7.4 Future Work

Items not covered by this work but would greatly increase the understanding of the AFSD process for large-scale additive manufacturing are;

- Measuring the residual stresses produced in the as-deposited material.
- Determining the fatigue properties of the AFSD material as a function of the layers.
    - In terms of 6061, the elongation values and thus the strain energy density were statistically different. This affects the fracture toughness which is linked to fatigue performance.
    - In terms of 7075, the presence of graphite lubricant in the microstructure can act as a premade crack that will negatively affect the fatigue properties.
- Investigating the mechanical properties at the interface between two parallel overlapping deposits.
- Using transmission electron microscopy to characterize the precipitates in the as-deposited, annealed, and heat treated conditions.

Bibliography

[1] R. Stewart, Ed., "The Army and the New Look," in *American Military History: The United States Army in a Global Era, 1917-2008*, vol. 2, Washington, D.C.: Center of Military History United States Army, 209AD, pp. 573–590.

[2] W. Nuckols and R. Cameron, "Don't Harness an Ox to a Racehorse: Get the M113 Out of the Armored Brigade Combat Team ... Now, Please!," *Armor*, no. January-March, pp. 56–64, 2016.

[3] B. Cheeseman and M. Lynch, "U.S. ARMY RESEARCH, DEVELOPMENT AND ENGINEERING COMMAND," p. 17.

[4] "Alcoa's one-piece forged aluminum hull doubles blast protection for combat vehicles - ASM International." https://www.asminternational.org/search/-/journal_content/56/10180/22440462/NEWS (accessed Mar. 31, 2022).

[5] M. Anderson, "Smoothing the Path to Large-scale Additive Manufacturing," *Automotive Design & Production*, vol. 131, no. 8, pp. 20–22, Aug. 2019.

[6] E. R. Denlinger and P. Michaleris, "Mitigation of distortion in large additive manufacturing parts," *Proc. Inst. Mech. Eng. Part B J. Eng. Manuf.*, vol. 231, no. 6, pp. 983–993, May 2017, doi: 10.1177/0954405415578580.

[7] M. Borish, B. Post, A. Roschli, P. Chesser, L. Love, and K. Gual, "Defect Identification and Mitigation Via Visual Inspection in Large-Scale Additive Manufacturing - Materials Science & Engineering Collection - ProQuest," *J. Meterials*, vol. 71, no. 3, pp. 893–899, 2018.

[8] J. Ding *et al.*, "Thermo-mechanical analysis of Wire and Arc Additive Layer Manufacturing process on large multi-layer parts," *Comput. Mater. Sci.*, p. S092702561100365X, Jul. 2011, doi: 10.1016/j.commatsci.2011.06.023.

[9] D. Espalin, "High Feed Rate Wire Heating and Embedding for Large Area Additive Manufacturing of Parts Containing Embedded Electronic Functionality," Ph.D., The University of Texas at El Paso, United States -- Texas, 2017. Accessed: Oct. 31, 2020. [Online]. Available: http://search.proquest.com/materialscienceengineering/docview/2058066193/abstract/E825EF0A1CBE4207PQ/13

[10] P. 25 O. 2019 | 15:00 GMT, "The World's Largest 3D Metal Printer Is Churning Out Rockets - IEEE Spectrum," *IEEE Spectrum: Technology, Engineering, and Science News*. https://spectrum.ieee.org/aerospace/space-flight/the-worlds-largest-3d-metal-printer-is-churning-out-rockets (accessed Nov. 01, 2020).

[11] "Giant Satellite Fuel Tank Sets New Record for 3-D Printed Space Parts," *Media - Lockheed Martin*. https://news.lockheedmartin.com/2018-07-11-Giant-Satellite-Fuel-Tank-Sets-New-Record-for-3-D-Printed-Space-Parts (accessed Oct. 31, 2020).

[12] "Big Metal Additive," *Big Metal Additive*. https://bigmetaladditive.com/ (accessed Apr. 15, 2022).

[13] G. Lim, K. Lau, W. S. Cheng, Z. Chiang, M. Krishnan, and D. Ardi, "Residual Stresses in Ti-6 Al-4 V Parts Manufactured by Direct Metal Laser Sintering and Electron Beam Melting," 2017. https://www.semanticscholar.org/paper/Residual-Stresses-in-Ti-6-Al-4-V-Parts-Manufactured-Lim-Lau/47c3d15ae21b239a7cc976f918aa174e80a32318 (accessed Mar. 23, 2022).

[14] M. Köhler, S. Fiebig, J. Hensel, and K. Dilger, “Wire and Arc Additive Manufacturing of Aluminum Components,” *Metals*, vol. 9, no. 5, Art. no. 5, May 2019, doi: 10.3390/met9050608.
[15] I. Gibson, D. Rosen, and B. Stucker, “Post-processing,” in *Additive Manufacturing Technologies: 3D Printing, Rapid Prototyping, and Direct Digital Manufacturing*, I. Gibson, D. Rosen, and B. Stucker, Eds. New York, NY: Springer, 2015, pp. 329–350. doi: 10.1007/978-1-4939-2113-3_14.
[16] “Sciaky’s EBAM Process Achieves Qualification through Lockheed Martin Testing,” *Via Satellite*, Jul. 20, 2018. https://www.satellitetoday.com/uncategorized/2018/07/20/sciakys-ebam-process-achieves-qualification-through-lockheed-martin-testing/ (accessed Dec. 13, 2020).
[17] R. J. Williams, C. M. Davies, and P. A. Hooper, “A pragmatic part scale model for residual stress and distortion prediction in powder bed fusion,” *Addit. Manuf.*, vol. 22, pp. 416–425, Aug. 2018, doi: 10.1016/j.addma.2018.05.038.
[18] R. Griffiths, D. Petersen, D. Garcia, and H. Yu, “Additive Friction Stir-Enabled Solid-State Additive Manufacturing for the Repair of 7075 Aluminum Alloy,” *Appl. Sci.*, vol. 9, p. 3486, Aug. 2019, doi: 10.3390/app9173486.
[19] H. Z. Yu and R. S. Mishra, “Additive friction stir deposition: a deformation processing route to metal additive manufacturing,” *Mater. Res. Lett.*, vol. 9, no. 2, pp. 71–83, Feb. 2021, doi: 10.1080/21663831.2020.1847211.
[20] H. Z. Yu *et al.*, “Non-beam-based metal additive manufacturing enabled by additive friction stir deposition,” *Scr. Mater.*, vol. 153, pp. 122–130, Aug. 2018, doi: 10.1016/j.scriptamat.2018.03.025.
[21] A. Mukhopadhyay and P. Saha, “Mechanical Characterization of Aluminium Alloy 6061 Powder Deposit Made by Friction Stir Based Additive Manufacturing,” *Key Eng. Mater.*, vol. 846, pp. 110–116, Jun. 2020, doi: http://dx.doi.org/10.4028/www.scientific.net/KEM.846.110.
[22] R. J. Griffiths *et al.*, “A Perspective on Solid-State Additive Manufacturing of Aluminum Matrix Composites Using MELD,” *J. Mater. Eng. Perform.*, vol. 28, no. 2, pp. 648–656, Feb. 2019, doi: 10.1007/s11665-018-3649-3.
[23] “SAE Government Technologies Establishes Advanced Manufacturing Commercialization Center™ in Southeast Michigan.” http://www.sae.org/site/news/press-room/2022/04/sae-government-technologies-establishes-advanced-manufacturing-commercialization-center%E2%84%A2-in-southeast-michigan (accessed Jun. 08, 2022).
[24] “MELD Selected for World’s Largest Metal Printer – MELD Manufacturing.” https://meldmanufacturing.com/meld-selected-for-worlds-largest-metal-printer/ (accessed Jun. 08, 2022).
[25] “GVSC awards contract to build largest metal 3D printer ever,” *DVIDS*. https://www.dvidshub.net/news/397953/gvsc-awards-contract-build-largest-metal-3d-printer-ever (accessed Jun. 08, 2022).
[26] D. Garcia *et al.*, “In situ investigation into temperature evolution and heat generation during additive friction stir deposition: A comparative study of Cu and Al-Mg-Si,” *Addit. Manuf.*, vol. 34, p. 101386, Aug. 2020, doi: 10.1016/j.addma.2020.101386.
[27] F. Al-Badour, I. H. Zainelabdeen, R. K. Suleiman, and A. Adesina, “Crack Repair Using Hybrid Additive Manufacturing and Friction Stir Processing,” presented at the ASME 2019 Pressure Vessels & Piping Conference, Nov. 2019. doi: 10.1115/PVP2019-93688.

[28] M. E. J. Perry, R. J. Griffiths, D. Garcia, J. M. Sietins, Y. Zhu, and H. Z. Yu, "Morphological and microstructural investigation of the non-planar interface formed in solid-state metal additive manufacturing by additive friction stir deposition," *Addit. Manuf.*, vol. 35, p. 101293, Oct. 2020, doi: 10.1016/j.addma.2020.101293.
[29] O. G. Rivera *et al.*, "Influence of texture and grain refinement on the mechanical behavior of AA2219 fabricated by high shear solid state material deposition," *Mater. Sci. Eng. A*, vol. 724, pp. 547–558, May 2018, doi: 10.1016/j.msea.2018.03.088.
[30] B. J. Phillips *et al.*, "Microstructure-deformation relationship of additive friction stir-deposition Al–Mg–Si," *Materialia*, vol. 7, p. 100387, Sep. 2019, doi: 10.1016/j.mtla.2019.100387.
[31] D. Z. Avery *et al.*, "Influence of Grain Refinement and Microstructure on Fatigue Behavior for Solid-State Additively Manufactured Al-Zn-Mg-Cu Alloy," *Metall. Mater. Trans. A*, vol. 51, no. 6, pp. 2778–2795, Jun. 2020, doi: 10.1007/s11661-020-05746-9.
[32] H. J. McQueen, S. Spigarelli, M. E. Kassner, and E. Evangelista, *Hot Deformation and Processing of Aluminum Alloys*, 0 ed. CRC Press, 2016. doi: 10.1201/b11227.
[33] J. B. Jordon *et al.*, "Direct recycling of machine chips through a novel solid-state additive manufacturing process," *Mater. Des.*, vol. 193, p. 108850, Aug. 2020, doi: 10.1016/j.matdes.2020.108850.
[34] D. Z. Avery *et al.*, "Evaluation of Microstructure and Mechanical Properties of Al-Zn-Mg-Cu Alloy Repaired via Additive Friction Stir-Deposition," *J. Eng. Mater. Technol.*, pp. 1–35, Oct. 2021, doi: 10.1115/1.4052816.
[35] B. J. Phillips, C. J. Williamson, R. P. Kinser, J. B. Jordon, K. J. Doherty, and P. G. Allison, "Microstructural and Mechanical Characterization of Additive Friction Stir-Deposition of Aluminum Alloy 5083 Effect of Lubrication on Material Anisotropy," *Materials*, vol. 14, no. 21, p. 6732, Nov. 2021, doi: 10.3390/ma14216732.
[36] M. Y. Rekha, D. Avery, P. G. Allison, J. B. Jordon, and L. Brewer, "Nanostructure Evolution in AA7075 Alloy Produced by Solid State Additive Manufacturing – Additive Friction Stir - Deposition," *Microsc. Microanal.*, vol. 27, no. S1, pp. 3118–3119, Aug. 2021, doi: 10.1017/S1431927621010783.
[37] H. G. Yang, "Numerical Simulation of the Temperature and Stress State on the Additive Friction Stir with the Smoothed Particle Hydrodynamics Method," *Strength Mater.*, vol. 52, no. 1, pp. 24–31, Jan. 2020, doi: 10.1007/s11223-020-00146-1.
[38] L. P. Martin, A. Luccitti, and M. Walluk, "Repair of aluminum 6061 plate by additive friction stir deposition," *Int. J. Adv. Manuf. Technol.*, Sep. 2021, doi: 10.1007/s00170-021-07953-z.
[39] P. Asiatico, "THE APPLICABILITY OF ADDITIVE FRICTION STIR DEPOSITION FOR BRIDGE REPAIR," Virginia Polytechnic Institute and State University, Blackbsurg, VA, 2021.
[40] B. J. Phillips *et al.*, "Effect of parallel deposition path and interface material flow on resulting microstructure and tensile behavior of Al-Mg-Si alloy fabricated by additive friction stir deposition," *J. Mater. Process. Technol.*, vol. 295, p. 117169, Sep. 2021, doi: 10.1016/j.jmatprotec.2021.117169.
[41] B. A. Rutherford *et al.*, "Effect of Thermomechanical Processing on Fatigue Behavior in Solid-State Additive Manufacturing of Al-Mg-Si Alloy," *Metals*, vol. 10, no. 7, p. 947, Jul. 2020, doi: 10.3390/met10070947.

[42] S. C. Beck *et al.*, “The effect of solutionizing and artificial aging on the microstructure and mechanical properties in solid-state additive manufacturing of precipitation hardened Al–Mg–Si alloy,” *Mater. Sci. Eng. A*, vol. 819, p. 141351, Jul. 2021, doi: 10.1016/j.msea.2021.141351.
[43] J. K. Yoder, R. J. Griffiths, and H. Z. Yu, “Deformation-based additive manufacturing of 7075 aluminum with wrought-like mechanical properties,” *Mater. Des.*, vol. 198, p. 109288, Jan. 2021, doi: 10.1016/j.matdes.2020.109288.
[44] A. Kolhatkar, V. Karthik, G. M. S. K. Chaitanya, A. Kumar, and D. Ramchandran, “Development and Validation of a Miniature Tensile Specimen for Determination of Mechanical Properties,” *J. Test. Eval.*, vol. 47, no. 5, p. 20180294, Sep. 2019, doi: 10.1520/JTE20180294.
[45] J. Kazakeviciute, J. P. Rouse, D. Focatiis, and C. Hyde, “Small specimen techniques for estimation of tensile, fatigue, fracture and crack propagation material model parameters,” *J. Strain Anal. Eng. Des.*, vol. 57, no. 4, pp. 227–254, May 2022, doi: 10.1177/03093247211025208.
[46] K. Kumar *et al.*, “Use of Miniature Tensile Specimen for Measurement of Mechanical Properties,” *Procedia Eng.*, vol. 86, pp. 899–909, Jan. 2014, doi: 10.1016/j.proeng.2014.11.112.
[47] C.-G. Kuo, C.-Y. Hsu, J.-H. Chen, and P.-W. Lee, “Discharge current effect on machining characteristics and mechanical properties of aluminum alloy 6061 workpiece produced by electric discharging machining process,” *Adv. Mech. Eng.*, vol. 9, no. 11, p. 1687814017730756, Nov. 2017, doi: 10.1177/1687814017730756.
[48] S. R. Arunachalam, S. E. Galyon Dorman, R. T. Buckley, N. A. Conrad, and S. A. Fawaz, “Effect of electrical discharge machining on corrosion and corrosion fatigue behavior of aluminum alloys,” *Int. J. Fatigue*, vol. 111, pp. 44–53, Jun. 2018, doi: 10.1016/j.ijfatigue.2018.02.005.
[49] D. Madyira, “Effect of Wire EDM on Microstructure and Fracture Toughness of 7075-T6511 Aluminum Alloy,” Jul. 2015.
[50] B07 Committee, “Test Methods for Tension Testing Wrought and Cast Aluminum- and Magnesium-Alloy Products,” ASTM International. doi: 10.1520/B0557-15.
[51] “Grain Flow in Forgings - The Basics.” https://www.forgemag.com/articles/84265-grain-flow-in-forgings---the-basics (accessed Apr. 15, 2022).
[52] T. A. Dux, “Forging of Aluminum Alloys,” in *Aluminum Science and Technology*, K. Anderson, J. Weritz, and J. G. Kaufman, Eds. ASM International, 2018, pp. 315–335. doi: 10.31399/asm.hb.v02a.a0006493.
[53] “Forging Design Involving Parting Line and Grain Flow,” Jan. 2005, doi: 10.31399/asm.hb.v14a.a0004037.
[54] G. E. Totten, Ed., “Heat Treatment Practices of Age-Hardenable Aluminum Alloys,” in *Heat Treating of Nonferrous Alloys*, ASM International, 2016, pp. 245–273. doi: 10.31399/asm.hb.v04e.a0006288.
[55] D. S. MacKenzie, “Metallurgy of Heat Treatable Aluminum Alloys,” in *Aluminum Science and Technology*, K. Anderson, J. Weritz, and J. G. Kaufman, Eds. ASM International, 2018, pp. 411–437. doi: 10.31399/asm.hb.v02a.a0006509.
[56] L. Wang, X. Yang, J. D. Robson, R. E. Sanders, and Q. Liu, “Microstructural Evolution of Cold-Rolled AA7075 Sheet during Solution Treatment,” *Materials*, vol. 13, no. 12, p. 2734, Jun. 2020, doi: 10.3390/ma13122734.

[57] V. Kerlins, “Modes of Fracture,” Jan. 1987, doi: 10.31399/asm.hb.v12.a0001831.
[58] T. A. Dux, “Forging of Aluminum Alloys,” Nov. 2018, doi: 10.31399/asm.hb.v02a.a0006493.
[59] “Heat Treatment Practices of Age-Hardenable Aluminum Alloys,” Jun. 2016, doi: 10.31399/asm.hb.v04e.a0006288.
[60] B07 Committee, “Specification for Aluminum and Aluminum-Alloy Sheet and Plate,” ASTM International. doi: 10.1520/B0209_B0209M-21A.
[61] B07 Committee, “Specification for Aluminum and Aluminum-Alloy Die Forgings, Hand Forgings, and Rolled Ring Forgings,” ASTM International. doi: 10.1520/B0247-20.
[62] B07 Committee, “Specification for Aluminum and Aluminum-Alloy Extruded Bars, Rods, Wire, Profiles, and Tubes,” ASTM International. doi: 10.1520/B0221-21.
[63] S. Pantelakis and N. Alexopoulos, “Assessment of the ability of conventional and advanced wrought aluminum alloys for mechanical performance in light-weight applications,” *Mater. Des. - MATER Des.*, vol. 29, pp. 80–91, Dec. 2008, doi: 10.1016/j.matdes.2006.12.004.
[64] N. D. Alexopoulos and S. G. Pantelakis, “A New Quality Index for Characterizing Aluminum Cast Alloys with Regard to Aircraft Structure Design Requirements,” *Metall. Mater. Trans. Phys. Metall. Mater. Sci. A*, vol. 35A, no. 1, pp. 301–308, Jan. 2004.
[65] S. Preibisch, S. Saalfeld, and P. Tomancak, “Globally optimal stitching of tiled 3D microscopic image acquisitions,” *Bioinformatics*, vol. 25, no. 11, pp. 1463–1465, Jun. 2009, doi: 10.1093/bioinformatics/btp184.
[66] M. Warmuzek, “Metallographic Techniques for Aluminum and Its Alloys,” Dec. 2004, doi: 10.31399/asm.hb.v09.a0003769.
[67] S. Reich and C. Thomsen, “Raman Spectroscopy of Graphite,” *Philos. Trans. Math. Phys. Eng. Sci.*, vol. 362, no. 1824, pp. 2271–2288, 2004.
[68] C. Hirlimann, M. Jouanne, and C. Forrières, “Raman spectroscopy of graphite in cast iron,” *J. Raman Spectrosc.*, vol. 23, no. 5, pp. 315–317, 1992, doi: 10.1002/jrs.1250230512.
[69] “Standard Specification for Aluminum and Aluminum-Alloy Sheet and Plate.” https://www.astm.org/b0209_b0209m-21a.html (accessed Mar. 16, 2022).
[70] “Wrought Aluminum Alloys: Atlas of Fractographs,” Jan. 1987, doi: 10.31399/asm.hb.v12.a0000621.
[71] O. Beyssac and M. Lazzeri, “Application of Raman spectroscopy to the study of graphitic carbons in the Earth Sciences,” in *Raman spectroscopy applied to Earth sciences and cultural heritage*, G. Ferraris, J. Dubessy, M.-C. Caumon, and F. Rull, Eds. European Mineralogical Union, 2012, pp. 415–454. doi: 10.1180/EMU-notes.12.12.
[72] N. Zhu *et al.*, “The Effect of Anodization on the Mechanical Properties of AA6061 Produced by Additive Friction Stir-Deposition,” *Metals*, vol. 11, no. 11, p. 1773, Nov. 2021, doi: 10.3390/met11111773.

Appendix A

Table A.1 Published literature values of AFSD 6061 material.

	Yield (R_Y) (MPa)	UTS (R_{UTS})(MPa)	El. at fracture (A_{at}) (%)
Beck S. [42][1,2]	Ω = 300 rpm, V = 127 mm/min		
X 6061-AD	114 ± 2	**185 ± 22**	37 ± 11
X 6061-Sol.	147 ± 9	**292 ± 19**	33 ± 6
X 6061-T6	320 ± 2	**371 ± 7**	31 ± 3
Wrought 6061-T651	296 ± 2	**351 ± 2**	31 ± 2
Rutherford B. [41], [72][2]	Ω = 300 rpm, V = 127 mm/min		
X 6061-AD	61 ± 6.4	**137 ± 14.8**	68 ± 4
Z 6061-AD	64 ± 2.7	**130 ± 3.5**	60 ± 6
Wrought 6061-T651	296 ± 1.8	**316 ± 2.2**	34
6061-O	40 ± 0.2	**118 ± 2.4**	-
Phillips et al. [35][2,3]	Graphite lubriacant used Ω = 300 rpm V = 127 mm/min		
Y 6061-AD (Parallel passes)	~ 60	**~ 160**	~ 60
Mukhopadhyay and Saha [21][4]	Powder feedstock, Ω = 1700 rpm, V = 22 mm/min		
X 6061-AD	133	102	-
Y 6061-AD	133	108	-
Wells[5,6]	Temperature controlled, V = 101.6 mm/min		
X 6061-AD	66 ± 4.8	**147 ± 1.1**	22 ± 5.6
Z 6061-AD	61 ± 1.9	**123 ± 8.7**	11 ± 4.0
Z 6061-AD (outlier removed)	61 ± 2.2	**128 ± 0.5**	13 ± 0.8
X 6061-T6	288 ± 15.3	**323 ± 14.8**	8 ± 3.1
Z 6061-T6	313 ± 4.5	**337 ± 8.4**	2 ± 1.0
Wrought 6061-T6	411 ± 4.9	**431 ± 7.9**	7 ± 0.8

[1] Heat treatment: ASTM B918-B98120-M (Sol at 565 ºC 50 min, quenched, and aged at 177 ºC for 8hrs)
[2] Tensile testing: No standard listed, 5 mm extensometer, displacement-controlled test
[3] Values were determined from figure images in paper and claims that UTS was 20 MPa higher than Rutherfords single pass values [41]
[4] Tensile testing: No standard listed, no extensometer used, specimen used in Kumar et al.[46]
[5] Heat treatment: ASM Handbook (Annealed at 413 ºC for 3 hrs., Solutionized at 527 ºC for 1 hr., Quenched, Aged at 178 ºC for 8 hrs.) [52], [54]
[6] Tensile testing: ASTM B557-15, standard subsized round bar proportional to standard [50]

Table A.2 Published literature values of AFSD 6061 material.

	Yield (R_Y) (MPa)	UTS (R_{UTS})(MPa)	El. at fracture (A_{at}) (%)
Avery et al. [31][1,2]	Ω = 225 rpm, V = 50.8 mm/min		
Z 7075-AD	140	**295**	16
Z 7075 Naturally aged	150	**317**	15
7075-T651 feedstock	525	**583**	19
Yoder J.K. et al. [43][3,4]	Ω = 250 rpm, V = 76.2 mm/min, graphite lubricant		
X Direction 7075-T6	477	**541**	8.2
Feedstock Wrought 7075-T6	503	**575**	10.5
Wells[5,6]	Temp. Controlled, V = 101.6 mm/min, graphite lubricant		
Z 7075-AD	109 ± 5.3	**225 ± 18.9**	15 ± 7
Z 7075-AD (outlier removed)	109 ± 5.6	**231 ± 11.2**	16 ± 5.9
Z 7075-T6	452 ± 184.4	**518 ± 116**	4 ± 2.9
Z 7075-T6 (outliers removed)	528 ± 3.7	**573 ± 4.8**	6 ± 1.7
Wrought 7075-T6	507 ± 6.5	**566 ± 7.1**	9 ± 0.7

[1]Heat treatment: naturally aged for 850 hrs.
[2]Tensile testing: E606/E606M-12 modified specimen with 5 mm gauge extensometer.
[3] Heat treatment: Solutionized at 470 ºC for 2 hours, Quenched, Aged at 120 ºC for 20 hours
[4] Tensile: No standards listed gauge section of 25 x 6 x 2 mm, extension rate of 0.2 mm/min
[5] Heat treatment: ASM Handbook (Annealed at 413 ºC for 3 hrs., Solutionized at 527 ºC for 1 hr., Quenched, Aged at 178 ºC for 8 hrs.) [52], [54]
[6] Tensile testing: ASTM B557-15, standard subsized round bar proportional to standard [50]

Appendix B

Table B.1 AFSD X 6061-AD Tensile Results.

	AFSD X 6061-AD					
Sample #	1-1	2-1	3-1	4-1	4-2	5-1
E (GPa)	68	62	61	69	65	66
Yield (MPa)	62	63	62	62	71	74
UTS (Mpa)	146	147	147	146	149	148
El (at) (%)	19	19	18	19	20	34
El (after) (%)	38	36	33	38	33	34

Table B.2 AFSD Z 6061-AD Tensile Results.

	AFSD Z 6061-AD			
Sample #	11	12	**13**	15
E (GPa)	58	53	**50**	49
Yield (MPa)	64	59	**60**	60
UTS (Mpa)	129	128	**108**	128
El (at) (%)	14	12	**4**	13
El (after) (%)	25	33	**8**	32

Table B.3 AFSD X 6061-T6 Tensile Results.

	AFSD X 6061-T6		
Sample #	1-2	2-2	3-2
E (GPa)	71	70	61
Yield (MPa)	274	310	282
UTS (Mpa)	305	341	324
El (at) (%)	8	5	12
El (after) (%)	14	11	14

Table B.4 AFSD Z 6061-T6 Tensile Results.

	AFSD Z 6061-T6									
Sample #	1	2	3	4	**5**	6	7	8	9	10
E (GPa)	72	70	70	68	**68**	68	69	69	72	68
Yield (MPa)	321	316	313	309	**312**	310	307	312	315	320
UTS (Mpa)	350	333	331	339	**323**	336	328	338	342	350
El (at) (%)	4	2	1	3	**1**	2	2	3	3	4
El (after) (%)	3	4	3	3	**1**	4	5	11	8	8

Table B.5 Wrought 6061-T6 Results.

	Wrought 6061-T6							
Sample #	1	2	3	4[1]	5[1]	6	7	8
E (GPa)	70	71	70	62	68	73	70	72
Yield (MPa)	416	412	408	375	335	417	410	403
UTS (Mpa)	441	433	429	398	356	438	431	416
El (at) (%)	7	7	7	7	10	8	6	5
El (after) (%)	16	18	17	18	18	13	13	15

[1]Samples slipped in grip and failed prematurely, excluded from the average.

Table B.6 Wrought 6061-O Results.

	Wrought 6061-0	
Sample #	1	2
E (GPa)	70	70
Yield (MPa)	106	106
UTS (Mpa)	144	180
El (at) (%)	12	16
El (after) (%)	18	18

Table B.7 AFSD Z 7075-AD Tensile Results.

	AFSD Z 7075-AD								
Sample #	1	2	6	9	10	12	**13**	16	17
E (GPa)	71	68	65	70	61	68	**71**	71	72
Yield (MPa)	112	110	111	108	96	108	**106**	116	115
UTS (Mpa)	229	237	231	229	205	230	**181**	242	244
El (at) (%)	8	15	14	20	24	11	**2**	11	26
El (after) (%)	10	23	22	15	20	22	**5**	18	24

Table B.8 AFSD Z 7075-T6 Tensile Results.

	AFSD Z 7075-T6						
Sample #	3	4	5	8	11	**14**	**15**
E (GPa)	69	68	66	66	66	**68**	**68**
Yield (MPa)	531	529	532	521	527	**0**	**521**
UTS (Mpa)	575	569	566	576	578	**237**	**524**
El (at) (%)	7	6	3	7	6	**0**	**0**
El (after) (%)	9	7	6	6	8	**0**	**3**

Table B.9 Wrought 7075-T6 Tensile Results.

	Wrought 7075-T6						
Sample #	1	2	3	4	5	6	7
E (GPa)	69	67	67	67	67	68	68
Yield (MPa)	512	513	511	510	501	494	506
UTS (Mpa)	571	573	569	572	560	552	564
El (at) (%)	9	9	8	10	9	8	8
El (after) (%)	17	16	17	13	14	15	16

Table B.10 Wrought 7075-O Tensile Results.

	Wrought 7075-0	
Sample #	1	2
E (GPa)	68	64
Yield (MPa)	158	155
UTS (Mpa)	344	333
El (at) (%)	14	16
El (after) (%)	20	20

Table B.11 General steps used to polish the as-deposited and heat treated material.

Type Abrasive/Size	Load - lbs.	Base Speed	Relative Rotation	Time
320 Grit, water cooled	5	250	contra	until plane
600 Grit, water cooled	5	250	contra	2 min
800 Grit, water cooled	5	250	contra	2 min
1000 Grit, water cooled	5	250	contra	2 min
1200 Grit, water cooled	5	250	contra	2 min
9 um diamond suspension	5	150	contra	5 min
3 um diamond suspension	5	150	contra	4 min
1 um diamond suspension	5	150	contra	2 min
0.05 um Colloidal Silica	By hand	100	contra	1 min

Table B.12 The etchant name and chemical composition used for the 6061 and 7075 etching of the AFSD material.

Etchant Name	Chemical Composition	Method
Keller's	20(50) mL distilled H_2O 20(25) mL HNO_3, (70%) 20(15) mL HCl, (38%) 5(10) mL HF, 40%	Immersion for 1-2 min or until color changes, rinse in distilled water
Weck's	5 g NH_4HF_2, 100 mL H_2O	Swab for 10-30 seconds, rinse in distilled water